Analysis of Strain Effects on Schottky-Barrier Single- and Double-Walled Carbon Nanotube Transistors

A thesis submitted for the partial fulfillment of the requirement of the degree of

Master of Science in Electrical and Electronic Engineering

by

Md. Abdul Wahab

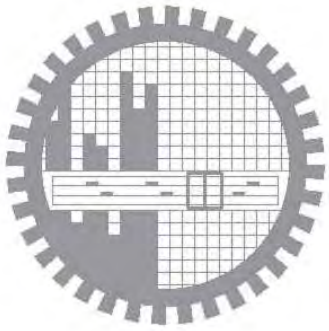

DEPARTMENT OF ELECTRICAL AND ELECTRONIC ENGINEERING
BANGLADESH UNIVERSITY OF ENGINEERING AND TECHNOLOGY
2010

The thesis titled " **Analysis of Strain Effects on Schottky-Barrier Single- and Double-Walled Carbon Nanotube Transistors**" Submitted by Md. Abdul Wahab, Roll No.: 100706225P, Session: October 2007 has been accepted as satisfactory in partial fulfillment of the requirement for the degree of MASTER OF SCIENCE IN ELECTRICAL AND ELECTRONIC ENGINEERING on April 27, 2010.

BOARD OF EXAMINERS

1. _____

Dr. Quazi Deen Mohd Khosru — **Chairman**
Professor — (Supervisor)
Department of Electrical and Electronic Engineering
Bangladesh University of Engineering and Technology
Dhaka-1000, Bangladesh.

2. _____

Dr. Aminul Hoque — **Member**
Professor and Head — (Ex-officio)
Department of Electrical and Electronic Engineering
Bangladesh University of Engineering and Technology
Dhaka-1000, Bangladesh.

3. _____

Dr. Md. Shafiqul Islam — **Member**
Professor
Department of Electrical and Electronic Engineering
Bangladesh University of Engineering and Technology
Dhaka-1000, Bangladesh.

4. _____

Dr. Anisul Haque — **Member**
Professor and Chairperson — (External)
Department of Electrical and Electronic Engineering
East West University
Dhaka-1212, Bangladesh.

Declaration

I hereby declare that this thesis or any part of it has not been submitted elsewhere for the award of any degree or diploma.

Md. Abdul Wahab

Dedication

To My Mother: Mrs. Sufia Begum

Contents

List of Figures

List of Tables

Acknowledgement

I would like to express my heartiest gratitude and profound respect to my supervisor Dr. Quazi Deen Mohd Khosru, Professor, Department of Electrical and Electronic Engineering, Bangladesh University of Engineering and Technology, Dhaka, for his continuous support, invaluable advice, and critical and constructive evaluations.

I am grateful to Dr. Aminul Hoque, Professor and Head, Department of Electrical and Electronic Engineering, Bangladesh University of Engineering and Technology, Dhaka, for providing all the necessary helps and his valuable time in this thesis.

I want to say 'thank you' to all others for helping me directly or indirectly to accomplish this work.

Abstract

A full band quantum mechanical simulation model using p_z orbital of carbon atom is developed to study the transport physics of uniaxial and torsional strained double-walled (DW) carbon nanotube (CNT) field-effect transistors (FETs) and to analyze their performance. The characteristics and performance of our proposed DW CNTFET are compared with existing SW CNTFET. It is shown that both the uniaxial and torsional strain can change the band gap of DW CNT and this band gap is the minimum of the two band gaps of the tubes from which DW CNT is constituted. The strain has large impact on the I-V characteristics of both SW and DW CNT devices. Tensile and torsional strains improve greatly the off-state current and on/off current ratio of both devices. Compressive strain improves on-state current, but this improvement is comparatively small. The effect of strain on off-state current, on-state current and on/off current ratio is higher in SW CNTFET. The inverse subthreshold slope of DW CNTFET is better than SW CNTFET. But the variation of inverse subthreshold slope with strain is smaller in DW CNTFET. The effect of strain on C-V characteristics is observed. Unlike SW CNTFET the on-state transconductance of DW CNTFET increases with tensile and torsional strains and decreases with compressive strain. The on-state cut-off frequency of DW CNTFET also shows opposite behavior to SW CNTFET with strain following on-state transconductance. Intrinsic switching delay improves greatly with compressive strain only for both devices. Again the SW CNTFET exhibits better change with strain than DW CNTFET. Concrete Physical description is provided to explain all above changes with strain. To complete the whole analysis of DW CNTFET the dimensions of the device are varied and their effects on the performance are observed.

Chapter 1

Introduction

Advent of nanotechnology will scale the size of the conventional MOS device to its physical limit within next decade [1, 2]. Then the conventional silicon technology will confront tough challenges to sustain the scaling trend and some challenges are already menacing. Unconventional device geometry and different channel materials are being actively pursued in recent years with a view to keep device performance in line with the ever accelerating progress of semiconductor technology. Carbon nanotube (CNT) is one of the front line candidates for a possible replacement [3–8]. Each layer of graphite is known as graphene. Carbon nanotubes are formed by rolling-up the graphene sheets. Carbon nanotubes can be single-walled (SW), double-walled (DW), or multi-walled (MW) depending on the number of graphene sheets rolled-up to form the tubes. Carbon nanotubes have very high electron mobility [9]. Both electronic and mechanical properties of carbon nanotubes are remarkable. An overview of experimental and numerical study of carbon nanotubes and corresponding devices up to present time is discussed in the following sections.

1.1 Literature Review

Carbon nanotube was first discovered by Japanese electron microscopist Sumio Iijima in 1991 [10]. Since then a significant progress has been achieved to learn the characteristics of carbon nanotubes and to examine their application in future nanoelectronics. First transistor using CNTs appears in 1998 [11, 12]. Since then the development of CNTs as a field effect transistors (FETs) has been rapid. The potential performance advantages of CNTFETs over conventional silicon MOSFETs have been established up to the scaling limit [13]. Schottky-barrier CNTFETs have been heavily studied. It has been found that carbon nanotube Schottky-barrier transistors exhibit scaling that is qualitatively different than conventional Si metal-oxide-semiconductor field effect transistors (MOSFETs) [14]. To suppress the OFF current the drain voltage must be scaled appropriately [15]. Contact geometry of carbon nanotube FETs plays an important role to charge transfer from the contact electrode to the one dimensional (1D) CNT channel [16]. Thinner electrodes for contacts dramatically improve device performance by modifying the electric field at the contact [17]. Asymmetry between the source and drain dielectrics can reduce the OFF current [18,19]. The metal-CNT work function difference has been modified by adsorbates and chemical means [20–23]. A zero-Schottky-barrier metal-CNT contact for the valence band or p-channel CNTFET has been demonstrated experimentally

using different metals, such as palladium (Pd) and rhodium (Rh) [24,25]. Recently, zero-Schottky-barrier ballistic n-type CNTFET has been realized using scandium (Sc) [26]. Potassium doping has been demonstrated to give n-type channels [21]. Also a lot of researches have been accomplished on ambipolar behavior [20] and the frequency response of CNTFETs [27–29].

Strain engineering has been extensively investigated for boosting the performance of nanoscale silicon MOSFETs through application of stress in the channel region [30, 31]. Strain improves the transconductance of PMOSFET by 7 % by improving electron and hole mobilities. Strain improves the drive current of CMOS devices by 20 %. Here, heavy mechanical stress is produced by addition of SiN to the channel. Strain also plays an important role in the electrical properties of carbon nanotubes [32–41] and has been a subject of strong research interest. Mechanical [42, 43] properties of carbon nanotubes are remarkable. It can withstand very large mechanical strains [42] and have extremely high Young's modulus [43]. Depending on its radius and chirality, it shows metallic or semiconducting behavior [35]. Maiti *et al.* [41] have shown that strain can change the conductance of a zigzag nanotube by several orders of magnitude through theoretical analysis. The pioneer experiment by Tombler *et al.* [44] has demonstrated that high strain ($\sim$3%) can change the conductance of a metallic single wall nanotube by two orders of magnitude by applying strain to a suspended nanotube using atomic force microscope (AFM) tip. Strain can open up a band gap in metallic CNTs and can modify the band gap of semiconducting CNTs [45]. Small band gap semiconducting or quasi-metallic nanotubes exhibit the largest changes in resistance and piezo-resistive gauge factors, and they can be used as nanoscale pressure sensors [46]. While the study of strain effects on electronic and mechanical properties of CNTs shows significant progress, strain engineering in CNT based devices is still in early stage. Single walled carbon nanotube devices have been fabricated on elastomeric polydimethylsiloxane (PDMS) substrates [47]. In those devices, strain has been applied to modulate their electronic properties. The conductance of a suspended multi-walled CNT has been measured by applying strain using AFM tip [48]. The strain effects on the performance of ballistic Schottky-barrier single-walled carbon nanotube field effect transistors (SB-CNTFETs) have been theoretically studied [49]. In this paper it is shown that strain significantly improves off-state current, on/off current ratio and switching speed. Strain also improves the drive current. DW tubes possess clear advantages over SW CNTs for various specific applications such as superior mechanical properties and structural and thermal stability [50]. SW CNTs are structurally stable up to 1200 ^{o}C whereas DW CNTs 2000 ^{o}C [50]. Carbon nanotubes always contain structural defects eg. pentagons, pentagon-heptagon pairs, vacancies, interstitials, metallic impurities etc. These defects diminish considerably the mechanical strength of nanotubes and affect their electronic transport. Structural defects and metal particles present within DW CNTs can be efficiently removed without altering the structure and diameters of the tubes by heat treatment or annealing which is not possible in SW CNTs for lower stable temperature limit. Therefore, DW CNTs could replace SW CNTs in numerous technological applications, and could be used in the fabrication of nanoelectronic devices. DW CNT exhibits superior mechanical properties over SW CNTs [51]. Double-walled carbon nanotubes also have attracted considerable attention since their intrinsic coaxial structure gives rise to intriguing electronic and optical properties [51].

Research on DW CNTFETs is still in early stage [52–56]. However, few measurements on electrical transport in DW CNTFETs have been carried out so far [57]. DW CNTFET experimentally exhibits better inverse subthreshold slope than SW CNTFET [52]. For a DW CNT with metallic inner tube and semiconducting outer tube, Wang *et al.* [54, 56] have found that free charges in the inner tube screen the outer tube's potential from the gate effect. This screening is directly related to the charge transfer from outer tube to inner tube or inter tube interaction and degrades the device performance [54]. Electronic transport properties of Cs-encapsulated DW CNTs synthesized via the plasma irradiation method have been studied [55]. The Cs-encapsulated DW CNTs exhibit high performance n-channel FETs in contrast to ambipolar behavior of pristine DW CNTs. The future of DW CNTFET is bright, the DW CNTs exhibit superior mechanical properties over SW CNTs, and strain greatly improves the performance of SW CNTFET. That is why we have been motivated to analyze the performance of DW CNTFET with strain.

1.2 Objective of the Work

In this work, we pay more emphasis on the performance analysis of ballistic Schottky-barrier DW CNTFETs with strain through quantum mechanical simulation. Since theoretical work on Schottky-barrier SW CNTFETs with strain has already been performed, we pay less emphasis on it. To extend our work we have made performance analysis of the same device by varying different physical parameters of it. The simulation model uses a self-consistent solution between electrostatics and charge density. For electrostatics of the coaxial geometry, we solve two dimensional Poisson's equation in cylindrical coordinates. For charge density, we solve the p_z orbital basis Schrodinger's equation using recursive Green's function algorithm [58]. The DW nanotube is generated from two semiconducting, (10, 0) and (19, 0), zigzag nanotubes with wall separation of 0.34 nm [59–61], and the SW nanotube is the (19, 0) zigzag tube. The experimental study by Wang *et al.* [54] shows that the M-S and M-M structures, out of the possible four distinct shell (outer)-shell (inner) combinations, i.e., metallic (M)-semiconducting (S), M-M, S-M, and S-S, are basically metallic CNTFETs, and they lose their functionality as a FET due to the lack of defined on- and off-states. The inner M and outer S structure shows hole conduction in negative gate bias at low temperature, however, the device can not be turned off. At room temperature, this structure, S-M, has almost no variation of drain current with the gate bias. Therefore, S-S is the only possible structure that can be used to build electronic logic devices, and we use this structure in our study. We make the SW nanotube to have the same diameter as the DW nanotube because in that case both of them would have almost same band gap, and their performance comparison would be meaningful.

1.3 Thesis Layout

This thesis consists of seven chapters. Chapter one gives an introduction followed by literature review, objective of the work.

Fundamental matters of carbon nanotube are studied in chapter two.

Chapter three deals with the self-consistent model between Poisson's solver and

Schrodinger's solver. We develop numerical Poisson's solver using finite difference method. To develop schrodinger's solver we have two alternative methods: Green's function algorithm and recursive Green's function algorithm. But we use the second one for our research.

The conductivity of both strained single-walled and double-walled carbon nanotubes are measured through numerical simulation in chapter four.

A comparison of performance through quantum mechanical simulation between the single-walled CNTFETs and the double-walled CNTFETs with strain is presented in chapter five.

The performance of CNTFETs is analyzed with varying different physical lengths in chapter six in unstrained case.

Conclusive remarks and discussions are presented in chapter seven. A recommendation for future study is also suggested here.

Chapter 2

Study of Carbon Nanotube

Each layer of graphite is known as graphene. Carbon nanotubes are formed by rolling-up the graphene sheets. Carbon nanotube can be single-walled, double-walled, or multi-walled depending on the number of graphene sheets rolled-up coaxially. Although in experiment the carbon nanotubes are built up automatically through chemical vapor deposition, for simulation purposes we should have clear idea about graphene to develop the numerical model of carbon nanotube. In this section, the electronic structures and properties of carbon nanotubes as well as graphene sheets are discussed.

2.1 Two Dimensional Graphene

A graphene sheet is a single layer of three dimensional graphite. The bonding mechanism in a graphene is similar to that of graphite. The atomic number of carbon is 6, and the atom electronic structure is $1s^2 2s^2 2p^2$ in atomic physics notation. When carbon atoms combine to form graphite, sp^2 hybridization occurs. In this process one s-orbital and two p-orbitals (p_x and p_y) combine to form three hybrid sp^2-orbitals at 120^o to each other within a plane. This in-plane bond is referred to as a σ-bond. This is a strong covalent bond that binds the atoms in the plane, and results in the high stiffness and high strength of a graphene. The remaining p-orbital (p_z) is perpendicular to the plane of σ-bonds. It contributes mainly to the interlayer interaction and is-called the π-bond. This π-bond is much weaker than a σ-bond. Figure 2.1 shows the graphene lattice with lattice vectors, $\overrightarrow{a}_1$ and $\overrightarrow{a}_2$, where,

$$\overrightarrow{a}_1 = (2, 0)\frac{a}{2}, \overrightarrow{a}_2 = (1, -\sqrt{3})\frac{a}{2}. \tag{2.1}$$

Here the lattice constant $a = |\overrightarrow{a}_1| = |\overrightarrow{a}_2| = \sqrt{3}a_{CC} = 2.49\mathring{A}$. The carbon-carbon bond distance a_{CC} for graphene is 1.44 $\mathring{A}$. In tight binding model, only the nearest-neighbor interactions are non-zero. Each atom in the basis has three nearest-neighbor as shown in Fig. 2.1. Here the bond vectors are

$$\begin{aligned} \overrightarrow{r}_1 &= (\sqrt{3}, -1)a_{CC}/2 \\ \overrightarrow{r}_2 &= (2, 0)a_{CC}/2 \\ \overrightarrow{r}_3 &= (-\sqrt{3}, -1)a_{CC}/2 \end{aligned} \tag{2.2}$$

Using the lattice vectors and bond vectors, and adding them appropriately we

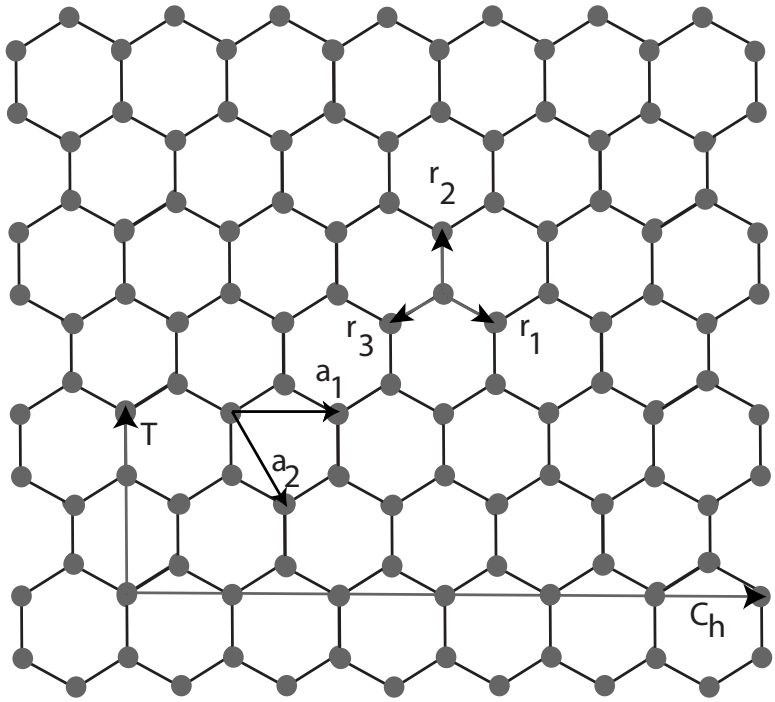

Figure 2.1: A 2D graphene sheet with lattice vectors and bond vectors.

easily determine the different lattice position of the graphene to form the numerical model.

2.2 Graphene to Carbon Nanotube

A single-walled CNT is made from a 2D graphene by rolling it up into a cylindrical shape. Electrons in a CNT are confined in the radial and circumferential directions due to layer thickness and periodicity, respectively. So the structure becomes one-dimensional (1D) with axial symmetry. CNTs can be single-walled, doubled-walled, or multi-walled. However, first we discuss about single-walled CNT, then double-walled CNT. The structure of single-walled nanotube is distinguished by two vectors, chiral vector $\overrightarrow{C}_h$ and translational vector $\overrightarrow{T}$. The chiral vector is expressed by the real space unit vectors $\overrightarrow{a}_1$ and $\overrightarrow{a}_2$ of the graphene sheet

$$\overrightarrow{C}_h = n\overrightarrow{a}_1 + m\overrightarrow{a}_2 \tag{2.3}$$

and the nanotube is specified as (n,m), where, n and m are integers. A zigzag nanotube corresponds to the case of m = 0, an armchair nanotube corresponds to the case of n = m, and all other (n,m) nanotubes are chiral nanotubes. In terms of n and m, the magnitude of the chiral vector is

$$C_h = a\sqrt{n^2 + m^2 + nm}. \tag{2.4}$$

The chiral vector is the circumference of the nanotube. The translational vector is defined as the unit vector parallel to the nanotube axis and perpendicular to the chiral vector in the graphene lattice as shown in Figure 2.1. In terms of the honey comb lattice vectors, the translational vector is

$$\overrightarrow{T} = t_1\overrightarrow{a}_1 + t_2\overrightarrow{a}_2, \tag{2.5}$$

where,

$$t_1 = \frac{2m+n}{d_R}, t_2 = \frac{2n+m}{d_R}. \tag{2.6}$$

Here d_R is the greatest common divisor of $(2m+n)$ and $(2n+m)$. The unit vectors of the nanotube are the chiral vector and the translational vector, and the unit cell is the rolled-up form of the rectangle generated by these two vectors.

Alike graphene we can develop the simulation model of the single-walled carbon nanotube structure by taking the help of the lattice vectors and the bond vectors. The procedure for counting the atomic position should be:

Calculate the atomic position of all the first layer atoms consecutively. Repeat this procedures for consecutive layers until all layers completed.

Now we develop the simulation model of double-walled carbon nanotube structure in strainless case. The procedure for counting the atomic position should be:

Calculate the atomic position of all the first layer atoms consecutively of the outer tube as we did for single-walled carbon nanotube by taking the help of lattice vectors and bond vectors of the outer tube.

Now switch to the first layer of the inner tube. Calculate the atomic position of all the first layer atoms consecutively of the inner tube with the help of lattice vectors and bond vectors of the inner tube.

Now switch back to the outer tube and calculate the atomic position of the second layer of this tube. Then do the same task for the second layer of the inner tube.

Now move to the next layers consecutively and repeat the previous procedures.

Within layer, with uniaxial strain applied, the axial, r_{it}, and the circumferential, r_{ic}, components of a carbon-carbon bond are modified by the following equation [35]

$$\begin{aligned} r_{it} &= (1+\epsilon_t) r_{i0t}, \\ r_{ic} &= (1+\epsilon_c) r_{i0c}. \end{aligned} \tag{2.7}$$

Here, ϵ_t is the transverse strain and ϵ_c is the circumferential strain [62], and r_{i0t} and r_{i0c} are the axial and the circumferential components, respectively, of the unstrained carbon-carbon bond. Here, ϵ_t and ϵ_c are related via Poisson's ratio [49]

$$\begin{aligned} \nu &= -\frac{\triangle r/r}{\triangle l/l} \\ &= -\frac{\epsilon_c}{\epsilon_t}, \end{aligned} \tag{2.8}$$

where, r and $\triangle r$ are original radius and its change, l and $\triangle l$ are the original length and its change of the strained CNT, and $i = 1$, 2 and 3 for three bond vectors of graphene layer (Figure 2.1). Poisson's ratio is considered here for the realistic calculation of strain and its value of 0.2 is used in our simulation [39, 49]. For torsional strain, the circumferential component of the carbon-carbon bond modifies as

$$r_{ic} = r_{i0c} + \tan(\theta) r_{i0t}, \tag{2.9}$$

where, θ is the shear strain [35].

Before application of strain the bonding vectors between nearest neighbor atoms $\overrightarrow{r}_{10}$, $\overrightarrow{r}_{20}$, and $\overrightarrow{r}_{30}$ were [35]

$$\overrightarrow{r}_{10} = \frac{a^2}{2}\frac{n+m}{c_h}\widehat{c} - \frac{a^2}{2\sqrt{3}}\frac{n-m}{c_h}\widehat{t}, \tag{2.10}$$

$$\overrightarrow{r}_{20} = -\frac{a^2}{2}\frac{m}{c_h}\widehat{c} + \frac{a^2}{2\sqrt{3}}\frac{2n+m}{c_h}\widehat{t}, \tag{2.11}$$

$$\overrightarrow{r}_{30} = -\frac{a^2}{2}\frac{n}{c_h}\widehat{c} - \frac{a^2}{2\sqrt{3}}\frac{n+2m}{c_h}\widehat{t}. \tag{2.12}$$

After incorporating uniaxial as well as torsional strain by Eqs. 2.7 and 2.9, the modified bonding vectors become [35]

$$\begin{aligned}\overrightarrow{r}_1 &= \left[(1+\epsilon_c)\frac{a^2}{2}\frac{n+m}{c_h} - \tan(\gamma)\frac{a^2}{2\sqrt{3}}\frac{n-m}{c_h}\right]\widehat{c} \\ &\quad - \left[(1+\epsilon_t)\frac{a^2}{2\sqrt{3}}\frac{n-m}{c_h}\right]\widehat{t},\end{aligned} \tag{2.13}$$

$$\begin{aligned}\overrightarrow{r}_2 &= -\left[(1+\epsilon_c)\frac{a^2}{2}\frac{m}{c_h} - \tan(\gamma)\frac{a^2}{2\sqrt{3}}\frac{2n+m}{c_h}\right]\widehat{c} \\ &\quad + \left[(1+\epsilon_t)\frac{a^2}{2\sqrt{3}}\frac{2n+m}{c_h}\right]\widehat{t},\end{aligned} \tag{2.14}$$

$$\begin{aligned}\overrightarrow{r}_3 &= -\left[(1+\epsilon_c)\frac{a^2}{2}\frac{n}{c_h} + \tan(\gamma)\frac{a^2}{2\sqrt{3}}\frac{n+2m}{c_h}\right]\widehat{c} \\ &\quad - \left[(1+\epsilon_t)\frac{a^2}{2\sqrt{3}}\frac{n+2m}{c_h}\right]\widehat{t}.\end{aligned} \tag{2.15}$$

To develop the simulation model of both single-walled and double-walled carbon nanotube structures with strain we take the help of modified bond vectors due to strain and follow the previous procedures.

There are three possible combination to incorporate strain in double-walled carbon nanotube: strain only in outer tube, strain only in inner tube and strain in both tubes. To apply strain in outer tube only and leave the inner tube unstrained, we use modified bond vectors for outer tube and bond vectors for inner tube to develop the simulation model of the double-walled carbon nanotube structure and we follow the same procedure of developing the structure as we did in strainless case. To incorporate strain in both tubes we use modified bond vectors for both tubes and for inner tube only we use modified bond vectors for inner tube.

Chapter 3

Simulation Model of the Device

The simulation model uses a self-consistent solution between electrostatics and charge density.

3.1 Poisson's Solver

The cross section of the cylindrical device that we study is shown in Figure 3.1. This device structure was reported in literatures [63–66]. The carbon nanotube (either SW or DW) is used as channel materials. The length of the tube is the summation of gate length(L_g), source underlap (L_{uS}) and drain underlap (L_{uD}). The gate oxide is SiO_2 of dielectric constant 3.9 with thickness t_{ox} [67]. The same oxide is used as extended dielectric material with thickness of t_{ox-ex}. Source and drain metal extensions L_{ex} are included to take care of fringing electric fields [63–66]. The gate metal has the same work function as the CNT has. The work function of the CNT is 4.5 eV [68]. The source and drain metal Fermi levels align with the conduction band of the CNT.

For the coaxially gated CNTFET, Figure 3.1, we obtain electrostatic potential by solving Poisson's equation [63]

$$\nabla.(\epsilon \nabla V) = -\rho. \tag{3.1}$$

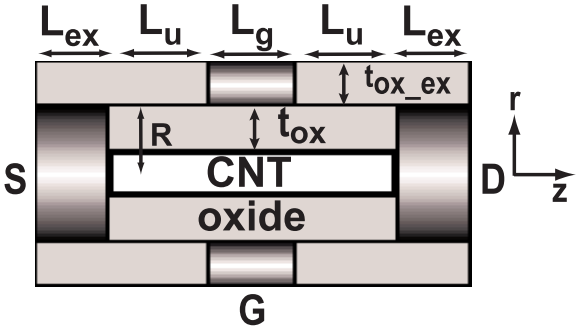

Figure 3.1: The cross-sectional view of the coaxial gate device with carbon nanotube as channel. The coordinates and different dimensions are also shown.

Here, ρ is charge density and $\epsilon = \epsilon_0 \epsilon_r$ with ϵ_r being the relative permitivity and ϵ_0 the free space permitivity. Poisson's equation, Eq. (3.1), in cylindrical coordinates

(r, ϕ, z) with the assumption that V is independent of ϕ for the coaxial device is

$$\frac{\partial^2 V}{\partial r^2} + \left[\frac{1}{r} + \frac{1}{\epsilon}\frac{\partial \epsilon}{\partial r}\right]\frac{\partial V}{\partial r} + \left[\frac{1}{\epsilon}\frac{\partial \epsilon}{\partial z}\right]\frac{\partial V}{\partial z} + \frac{\partial^2 V}{\partial z^2} = \frac{-\rho}{\epsilon}. \tag{3.2}$$

The Poisson's equation, Eq. (3.2), is discretized using finite difference and it becomes

$$a(i)V(i-1,j)+b(i)V(i,j)+c(i)V(i+1,j)+d(i)V(i,j-1)+e(i)V(i,j+1) = -\frac{\rho(i,j)}{\epsilon(i,j)}, \tag{3.3}$$

where,

$$\begin{aligned} a(i) &= \frac{2}{[z(i+1)-z(i-1)][z(i)-z(i-1)]} \\ &\quad -\frac{\epsilon(i+1,j)-\epsilon(i-1,j)}{\epsilon(i,j)[z(i+1)-z(i-1)]^2}, \end{aligned} \tag{3.4}$$

$$\begin{aligned} b(i) &= \frac{-2}{[z(i+1)-z(i-1)][z(i+1)-z(i)]} \\ &\quad +\frac{-2}{[z(i+1)-z(i-1)][z(i)-z(i-1)]} \\ &\quad +\frac{-2}{[r(j+1)-r(j-1)][r(j+1)-r(j)]} \\ &\quad +\frac{-2}{[r(j+1)-r(j-1)][r(j)-r(j-1)]}, \end{aligned} \tag{3.5}$$

$$\begin{aligned} c(i) &= \frac{2}{[z(i+1)-z(i-1)][z(i+1)-z(i)]} \\ &\quad +\frac{\epsilon(i+1,j)-\epsilon(i-1,j)}{\epsilon(i,j)[z(i+1)-z(i-1)]^2}, \end{aligned} \tag{3.6}$$

$$\begin{aligned} d(i) &= \frac{2}{[r(j+1)-r(j-1)][r(j)-r(j-1)]} \\ &\quad -\left[\frac{1}{r(j)}+\frac{\epsilon(i,j+1)-\epsilon(i,j-1)}{\epsilon(i,j)[r(j+1)-r(j-1)]}\right] \\ &\quad \left\{\frac{1}{r(j+1)-r(j-1)}\right\}, \end{aligned} \tag{3.7}$$

$$\begin{aligned} e(i) &= \frac{2}{[r(j+1)-r(j-1)][r(j+1)-r(j)]} \\ &\quad -\left[\frac{1}{r(j)}+\frac{\epsilon(i,j+1)-\epsilon(i,j-1)}{\epsilon(i,j)[r(j+1)-r(j-1)]}\right] \\ &\quad \left\{\frac{1}{r(j+1)-r(j-1)}\right\}. \end{aligned} \tag{3.8}$$

At $r = 0$ i.e. $j = 1$, $\lim_{r\to 0} \frac{1}{r}\frac{\partial V}{\partial r} = \frac{\partial^2 V}{\partial r^2}$. So, the Poisson's equation, Eq. (3.2), becomes

$$2\frac{\partial^2 V}{\partial r^2} + \left[\frac{1}{\epsilon}\frac{\partial \epsilon}{\partial z}\right]\frac{\partial V}{\partial z} + \frac{\partial^2 V}{\partial z^2} = \frac{-\rho}{\epsilon}. \tag{3.9}$$

Here, we assume that there is no variation of dielectric constant along axial direction at $r = 0$. Again we discretize this using finite difference as Eq. (3.3) where,

$$\begin{aligned} a(i) &= \frac{2}{[z(i+1) - z(i-1)][z(i) - z(i-1)]} \\ &\quad - \frac{\epsilon(i+1, j) - \epsilon(i-1, j)}{\epsilon(i, j)[z(i+1) - z(i-1)]^2}, \end{aligned} \tag{3.10}$$

$$b(i) = \frac{-4}{(\Delta r)^2} + \frac{-2}{[z(i+1) - z(i)][z(i) - z(i-1)]}, \tag{3.11}$$

$$\begin{aligned} c(i) &= \frac{2}{[z(i+1) - z(i-1)][z(i+1) - z(i)]} \\ &\quad + \frac{\epsilon(i+1, j) - \epsilon(i-1, j)}{\epsilon(i, j)[z(i+1) - z(i-1)]^2}. \end{aligned} \tag{3.12}$$

Here, due to symmetry $V_{i,j+1} = V_{i,j-1}$ and the coefficient of $V_{i,j+1}$ becomes

$$d(i) + e(i) = \frac{4}{(\Delta r)^2}. \tag{3.13}$$

Here i=1,2,3,.....,N_z and j=1,2,3,.....,N_r where, N_z is the number of grid points in the axial coordinate and N_r is the number of grid points in the radial coordinate. Equation (3.3), in matrix form can be written as

$$[\mathbf{D}]\{\mathbf{V}\} = \{\mathbf{f}\}, \tag{3.14}$$

where,

$$\mathbf{D} = \begin{bmatrix} \mathbf{h} & \mathbf{t_2} & & & & & \\ \mathbf{t_1} & \mathbf{h} & \mathbf{t_2} & & & & \\ & \mathbf{t_1} & \mathbf{h} & \mathbf{t_2} & & & \\ & & & & & & \\ & & & & & & \\ & & & & & & \\ & & & & & \mathbf{t_1} & \mathbf{h} & \mathbf{t_2} \\ & & & & & & \mathbf{t_1} & \mathbf{h} \end{bmatrix}$$

and $\{\mathbf{V}\}$, and $\{\mathbf{f}\} = -\{\rho\}/\{\epsilon\}$ are the column vectors of $N = N_r \times N_z$ elements. The block matrices $[\mathbf{h}]$, $[\mathbf{t_1}]$, and $[\mathbf{t_2}]$ are $N_z \times N_z$ squared matrices where,

$$\mathbf{h} = \begin{bmatrix} b(1) & c(1) & & & & & \\ a(2) & b(2) & c(2) & & & & \\ & a(3) & b(3) & c(3) & & & \\ & & & & & & \\ & & & & & & \\ & & & & & & \\ & & & & a(N_z-1) & b(N_z-1) & c(N_z-1) \\ & & & & & a(N_z) & b(N_z) \end{bmatrix},$$

$$\mathbf{t}_1 = \begin{bmatrix} d(1) & & & & & \\ & d(2) & & & & \\ & & d(3) & & & \\ & & & & & \\ & & & & & \\ & & & & & \\ & & & d(N_z-1) & & \\ & & & & & d(N_z) \end{bmatrix},$$

and

$$\mathbf{t}_2 = \begin{bmatrix} e(1) & & & & & \\ & e(2) & & & & \\ & & e(3) & & & \\ & & & & & \\ & & & & & \\ & & & & & \\ & & & e(N_z-1) & & \\ & & & & & e(N_z) \end{bmatrix}$$

The matrix [**D**] can be regarded as a block tri-diagonal matrix with [**h**] the cross-section matrix, and [$\mathbf{t_1}$] and [$\mathbf{t_2}$] the coupling matrices between the cross sections when we walk across the device from left to right. Dirichlet boundary conditions are used at the source, drain, and gate metals [63–65]. Von Neumann boundary conditions are used along the exposed surface of the dielectric. There, the radial component of the electric field is set to zero [63–65].

After solving Poisson's equation, Eq.(3.2), numerically we learn potentials at different grid points of the device. But to solve this equation, we have to determine the charge density before hand. The solution of the Schrodinger's equation provides us the charge density. In next section we develop the recursive Green's function algorithm (RGFA) to solve Schrodinger's equation.

3.2 Schrodinger's Solver

For charge density, we solve time independent Schrodinger's equation [69]

$$H\psi = E\psi, \tag{3.15}$$

where,

$$H = -\frac{\hbar^2}{2m}\nabla^2 + V. \tag{3.16}$$

Here, H is the Hamiltonian operator, E is the total energy of the particle, $\hbar$ is the reduce Plank constant, and m is the mass of the particle. Matrix representation of the Schrodinger's equation [69]

$$[\mathbf{H}]\{\psi\} = E\{\psi\}. \tag{3.17}$$

Here $[\mathbf{H}]$ is the Hamiltonian matrix. We can get Eq. (3.17) from Eq. (3.15) by using finite difference method. We can also generate Hamiltonian matrix by using atomistic Hamiltonian concept [69].

We can rewrite Eq. (3.17) as

$$[E\mathbf{I} - \mathbf{H}]\{\psi\} = \{\mathbf{0}\}. \tag{3.18}$$

Here $[\mathbf{I}]$ is the identity matrix.

To solve the Schrodinger's equation (Eq. (3.15)) efficiently and to reduce the computation time there are two algorithms: non-equilibrium Green's function algorithm and recursive Green's function algorithm. But the latter one is more efficient and we have used it in our simulation. Since the recursive Green's function algorithm is the modified form of non-equilibrium Green's function algorithm, we have discussed both of them in this chapter in next sections.

3.2.1 Non-equilibrium Green's Function Algorithm

We now solve the Schrodinger's equation numerically for a channel connected to two contacts: source and drain (see Figure 3.2), by using non-equilibrium Green's function algorithm [69].

The electrons in the source and the drain contacts have wavefunctions $\{\phi_{\mathbf{S}}\}$ and $\{\phi_{\mathbf{D}}\}$, respectively, before connecting to the channel. Using Eq. (3.18) we can write Schrodinger's equations for the isolated contacts as

$$[E\mathbf{I} - \mathbf{H}_S + i\eta]\{\phi_S\} = \{\mathbf{S}_S\}, \tag{3.19}$$

and

$$[E\mathbf{I} - \mathbf{H}_D + i\eta]\{\phi_D\} = \{\mathbf{S}_D\}, \tag{3.20}$$

where, $[\mathbf{H}_S]$ and $[\mathbf{H}_D]$ are the Hamiltonians for the contacts source and drain, respectively, and a small positive infinitesimal times an identity matrix, $[\eta] = 0^+[\mathbf{I}]$, is added to introduce levels broadening. While coupling of the source and the drain contacts with the channel, states from both the contacts spill over to the channel and vice versa. The contacts lose part of their states as they spread into the channel and also gain some states from the channel. Since the loss occurs from fixed energy levels while the gain is spread out over range of energies, the overall effect is to broaden the channel density of states from their initial sharp structure to a more diffuse structure. The source terms, $\{\mathbf{S}_S\}$ and $\{\mathbf{S}_D\}$, are representing the excitation for the source and drain contacts, respectively, by the channel. When we couple the device to the contacts the electronic states from the contacts spill over giving rise

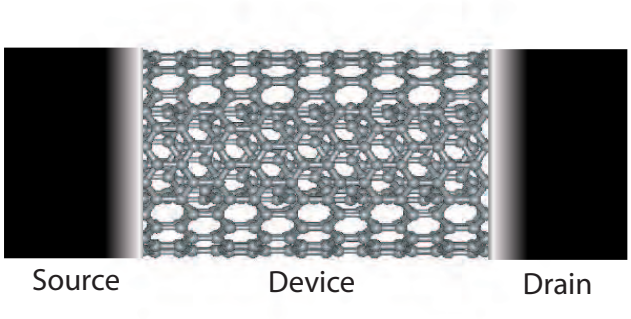

Figure 3.2: A carbon nanotube channel connected to two contacts.

to a wavefunction $\{\psi\}$ inside the device which in turn excites scattered waves $\{\chi_S\}$ and $\{\chi_D\}$ in the source and drain, respectively.

The overall wavefunction satisfies the composite Schrodinger's equation in matrix form for the source-device-drain system which can be written as

$$\begin{bmatrix} E\mathbf{I}-\mathbf{H}_S+i\eta & -\tau_S^\dagger & \mathbf{0} \\ -\tau_S & E\mathbf{I}-\mathbf{H} & -\tau_D \\ \mathbf{0} & -\tau_D^\dagger & E\mathbf{I}-\mathbf{H}_D+i\eta \end{bmatrix} \begin{Bmatrix} \phi_S+\chi_S \\ \psi \\ \phi_D+\chi_D \end{Bmatrix} = \begin{Bmatrix} \mathbf{S}_S \\ \mathbf{0} \\ \mathbf{S}_D \end{Bmatrix}, \tag{3.21}$$

where, $[\mathbf{H}]$ is the channel Hamiltonian, and $[\tau_S]$ and $[\tau_D]$ are the source-channel and drain-channel coupling Hamiltonian matrices, respectively. Using straightforward matrix algebra we can write

$$[E\mathbf{I}-\mathbf{H}_S+i\eta]\{\phi_S+\chi_S\}-[\tau_S]^\dagger\{\psi\}=\{\mathbf{S}_S\}, \tag{3.22}$$

$$-[\tau_S]\{\phi_S+\chi_S\}-[E\mathbf{I}-\mathbf{H}]\{\psi\}-[\tau_D]\{\phi_D+\chi_D\}=\{\mathbf{0}\}, \tag{3.23}$$

$$-[\tau_D]^\dagger\{\psi\}+[E\mathbf{I}-\mathbf{H}_D+i\eta]\{\phi_D+\chi_D\}=\{\mathbf{S}_D\}. \tag{3.24}$$

Substituting Eq. (3.19), in Eq. (3.22) we obtain

$$\{\chi_S\}=[\mathbf{G}_S][\tau_S]^\dagger\{\psi\}, \tag{3.25}$$

where,

$$[\mathbf{G}_S]=[E\mathbf{I}-\mathbf{H}_S+i\eta]^{-1}. \tag{3.26}$$

Similarly replacing Eq. (3.20) in (3.24) the result becomes

$$\{\chi_D\}=[\mathbf{G}_D][\tau_D]^\dagger\{\psi\}, \tag{3.27}$$

where,

$$[\mathbf{G}_D]=[E\mathbf{I}-\mathbf{H}_D+i\eta]^{-1}. \tag{3.28}$$

Here, $[\mathbf{G}_S]$ and $[\mathbf{G}_D]$ are the Green's function for the isolated reservoirs. Substituting Eqs. (3.25) and (3.27) in Eq. (3.23) considering coupling the Schrodinger's equation for the device becomes

$$[E\mathbf{I}-\mathbf{H}-\mathbf{\Sigma}_S-\mathbf{\Sigma}_D]\{\psi\}=\{\mathbf{S}\}, \tag{3.29}$$

where, $[\mathbf{\Sigma}_S] = [\tau_S][\mathbf{G}_S][\tau_S]^\dagger$ and $[\mathbf{\Sigma}_D] = [\tau_D][\mathbf{G}_D][\tau_D]^\dagger$, the self energy matrices, are the modification of the channel Hamiltonian [**H**], to incorporate boundary conditions from the source-channel and drain-channel interfaces, respectively. The broadening matrix for source contact is

$$\begin{aligned}[\mathbf{\Gamma}_S] &= i[\mathbf{\Sigma}_S - \mathbf{\Sigma}_S^\dagger] \\ &= [\tau_S][\mathbf{A}_S][\tau_S]^\dagger. \end{aligned} \tag{3.30}$$

Similarly, for drain contact the broadening matrix is

$$[\mathbf{\Gamma}_D] = [\tau_D][\mathbf{A}_D][\tau_D]^\dagger, \tag{3.31}$$

where, $[\mathbf{A}_S] = i[\mathbf{G}_S - \mathbf{G}_S^\dagger]$ and $[\mathbf{A}_D] = i[\mathbf{G}_D - \mathbf{G}_D^\dagger]$ are the spectral function for the isolated source and drain contacts, respectively. Also

$$\{\mathbf{S}\} = [\tau_S]\{\phi_S\} + [\tau_D]\{\phi_D\} \tag{3.32}$$

is the sum of the source terms $[\tau_S]\{\phi_S\}$ (from the source) and $[\tau_D]\{\phi_D\}$ (from the drain). To evaluate the density matrix, we define the channel Green's function

$$[\mathbf{G}] = [E\mathbf{I} - \mathbf{H} - \mathbf{\Sigma}_S - \mathbf{\Sigma}_D]^{-1} \tag{3.33}$$

and use it to express the channel wavefunction in terms of the source terms from Eq. (3.32)

$$\{\psi\} = [\mathbf{G}]\{\mathbf{S}\}. \tag{3.34}$$

Density matrix [69]

$$\rho = \int (dE/2\pi)\{[\mathbf{A}']f_S + [\mathbf{A}'']f_D\}, \tag{3.35}$$

where, spectral function $[\mathbf{A}'] = [\mathbf{G}][\mathbf{\Gamma}_S][\mathbf{G}]^\dagger$ arises from the spill over of states from the left contact and $[\mathbf{A}''] = [\mathbf{G}][\mathbf{\Gamma}_D][\mathbf{G}]^\dagger$ from the right contact. The total spectral function for the channel $[\mathbf{A}] = [\mathbf{A}'] + [\mathbf{A}'']$. Fraction $[\mathbf{A}']$ of the total spectral function of the channel remains in equilibrium with the source Fermi function f_S, while another fraction $[\mathbf{A}'']$ remains in equilibrium with the drain Fermi function f_D. The density of states of the channel at a particular energy level will be the summation of the diagonal elements of the spectral matrix [**A**] divided by 2π.

The net carrier flow at source terminal is given by the difference of inflow and out flow current [69]

$$I_D = \frac{\mathrm{tr}[\psi^\dagger \tau_S \phi_S - \phi_S^\dagger \tau_S^\dagger \psi]}{i\hbar} - \frac{\mathrm{tr}[\chi_S^\dagger \tau_S^\dagger \psi - \psi^\dagger \tau_S \chi_S]}{i\hbar}. \tag{3.36}$$

The first part of Eq. (3.36) is inflow and the second part outflow. Making use of Eq. (3.34) we can write Inflow =tr $[\mathbf{S}^\dagger \mathbf{G}^\dagger \mathbf{S}_S - \mathbf{S}_S^\dagger \mathbf{G}\mathbf{S}]/i\hbar$ =tr$[\mathbf{S}_S \mathbf{S}_S^\dagger \mathbf{A}]/\hbar$, since $\{\mathbf{S}\} = \{\mathbf{S}_S\} + \{\mathbf{S}_D\}$ and $\{\mathbf{S}_S\}^\dagger\{\mathbf{S}_D\} = \{\mathbf{S}_D\}^\dagger\{\mathbf{S}_S\} = 0$. $\{\mathbf{S}_S\}\{\mathbf{S}_S\}^\dagger = [\tau_S \phi_S \phi_S^\dagger \tau_S^\dagger]$. $\{\phi_S\}\{\phi_S\}^\dagger \Rightarrow \int \frac{dE}{D\pi} f_S[\mathbf{A}_S]$. So that

$$Inflow = \frac{S}{\hbar} \int (dE/2\pi) f_S \mathrm{tr}[\mathbf{\Gamma}_S \mathbf{A}]. \tag{3.37}$$

We make use of Eqs. (3.25) and (3.30) to write the outflow term as: Outflow = $\mathrm{tr}[\psi^\dagger \tau_S \mathbf{G}_S^\dagger \tau_S^\dagger \psi - \psi^\dagger \tau_S \mathbf{G}_S \tau_S^\dagger \psi]/i\hbar = \mathrm{tr}[\psi\psi^\dagger \mathbf{\Gamma}_S]/\hbar$. So that

$$Outflow = \frac{S}{\hbar}\int (dE/2\pi)\mathrm{tr}[\mathbf{\Gamma}_S[\mathbf{A}' f_S + \mathbf{A}'' f_D]]. \tag{3.38}$$

The net current at source terminal is given by the difference between the inflow and the outflow multiplied by the charge (-q) of an electron

$$I_D = \frac{q}{h}\int dE T(E)[f_S - f_D], \tag{3.39}$$

where, transmission, $T(E) = \mathrm{tr}[\mathbf{\Gamma}_S \mathbf{A}_D]$, tells us the rate at which carriers transmit from the source contact to the drain contact by propagating through the device.

3.2.2 Recursive Green's Function Algorithm

The recursive Green's function (RGF) algorithm [58] is most powerful for the nearest neighbor tight-binding model. In the derivation of the RGF we divide the 2-terminal device domain into N blocks in the longitudinal direction (see Figure 3.3). Each block can be single atomic layer or may be a unit cell. In Figure 3.3, L_1, L_2,...., L_N are different layers of carbon nanotube. For our simulation of the whole thesis each layer is considered as block of recursive Green's function algorithm. The block size is chosen so that the matrix elements are non-zero only between nearest neighbor blocks. Upper case G's are reserved for exact Green function elements. The term $[\mathbf{g}^l_{L,L}]$ indicates that the Green's function takes into account everything exactly on the left with the coupling elements immediately on the right, $[\mathbf{t}_{L,L+1}]$ and $[\mathbf{t}_{L+1,L}]$, set to zero. The term $[\mathbf{g}^r_{L,L}]$ indicates that the Green's function takes into account everything exactly on the right with the coupling elements immediately on the left, $[\mathbf{t}_{L,L-1}]$ and $[\mathbf{t}_{L-1,L}]$, set to zero. The right connected Green's function is created from

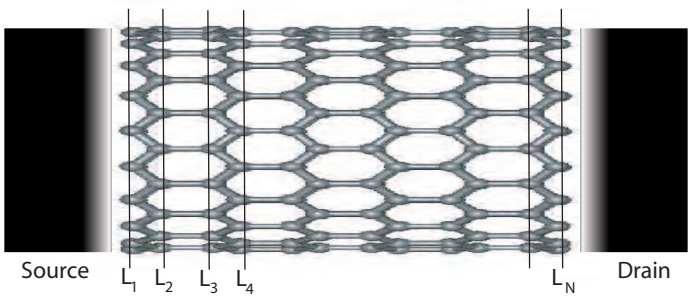

Figure 3.3: A carbon nanotube channel divided into N blocks for recursive Green's function algorithm.

$$[\mathbf{g}^r_{L,L}] = [E\mathbf{I} - \mathbf{H}_L - \mathbf{t}_{L,L+1}\mathbf{g}^r_{L+1,L+1}\mathbf{t}_{L+1,L}]^{-1}, \tag{3.40}$$

where, $[\mathbf{H}_L]$ is the layer Hamiltonian. The simulation started from the right hand side with boundary self-energy $[\Sigma_{N,N}] = -i[t_{N,N+1}]$. At atomic layer 1, the full Green's function is calculated from the following equation:

$$[\mathbf{G}_{1,1}] = [E\mathbf{I} - \mathbf{H}_1 - \Sigma_{1,1} - \mathbf{t}_{1,2}\mathbf{g}^r_{2,2}\mathbf{t}_{2,1}]^{-1}, \tag{3.41}$$

where, $[\Sigma_{1,1}] = -i[t_{1,0}]$ is left boundary self-energy. The $\{2, ..., N\}$ block-diagonal elements are calculated from

$$[\mathbf{G}_{L,L}] = [\mathbf{g}^r_{L,L} + \mathbf{g}^r_{L,L}\mathbf{t}_{L,L-1}\mathbf{G}_{L-1,L-1}\mathbf{t}_{L-1,L}\mathbf{g}^r_{L,L}] \tag{3.42}$$

and the corresponding spectral function $[\mathbf{A}_{L,L}] = i[G_{L,L} - G^\dagger_{L,L}]$. The first block column of the Green's function is created from

$$[\mathbf{G}_{L,1}] = [\mathbf{g}^r_{L,L}][(-\mathbf{t}_{L,L-1})][\mathbf{G}_{L-1,1}] \tag{3.43}$$

and the left-connected spectral function is given by

$$[\mathbf{A}^l_{L,L}] = [\mathbf{G}_{L,1}][\Gamma_{1,1}][\mathbf{G}^\dagger_{L,1}], \tag{3.44}$$

where, $[\Gamma_{1,1}] = i[\Sigma_{1,1} - \Sigma^\dagger_{1,1}]$. Finally we calculate the charge density $\{\rho\}$, the Jacobian $\{\frac{\partial\rho}{\partial V}\}$, and the current

$$\{\rho_L\} = (2q)\int \frac{dE}{2\pi}\mathrm{tr}\{f_S[\mathbf{A}^L_{L,L}] + f_D\left[\mathbf{A}_{L,L} - \mathbf{A}^L_{L,L}\right]\}, \tag{3.45}$$

$$\{\frac{\partial\rho_L}{\partial V}\} = (2q)\int \frac{dE}{2\pi}\mathrm{tr}\{\frac{\partial f_S}{\partial E}[\mathbf{A}^L_{L,L}] + \frac{-\partial f_D}{\partial E}\left[\mathbf{A}_{L,L} - \mathbf{A}^L_{L,L}\right]\}, \tag{3.46}$$

$$I_D = \frac{2q}{h}\int dE T(E)\left(f_S - f_D\right), \tag{3.47}$$

where, h is Planck's constant and the transmission is calculated from [58]

$$T(E) = \mathrm{tr}\left[\Gamma_{1,1}\left(A_{1,1} - G_{1,1}\Gamma_{1,1}G^\dagger_{1,1}\right)\right]. \tag{3.48}$$

3.3 Self-Consistent Loop

The self-consistent loop between Schrodinger's and Poisson's solver is started with Poisson's solver by initial guess of charge density throughout the device zero. After setting appropriate boundary conditions, Eq. (3.14) is solved using Newton-Rapshon method and updated in each iteration in the self-consistent loop as

$$\{\mathbf{V^{i+1}}\} = \{\mathbf{V^i}\} + m\{\triangle\mathbf{V}\}, \tag{3.49}$$

where,

$$\begin{aligned}\{\triangle\mathbf{V}\} &= \left[\mathbf{D} - \frac{\partial\mathbf{f}}{\partial V}\right]^{-1}\{\mathbf{f} - \mathbf{DV}\} \\ &= -\left[\mathbf{D} + \frac{1}{\epsilon}\frac{\partial\rho}{\partial V}\right]^{-1}\left\{\mathbf{DV} + \frac{\rho}{\epsilon}\right\}\end{aligned} \tag{3.50}$$

and m is a mixing factor. Here, $m = 0$ means to take the old input vector once more and $m = 1$ corresponds to use the output vector of the actual iteration directly as input vector for the following iteration. The latter choice in most cases leads to oscillations. For simple mixing scheme the value of m between 0-1 is assumed arbitrarily. Here, the convergence depends very sensitively on the choice of the mixing parameter, but experience has shown that $m \approx 0.5$ is a good choice for simple systems.

3.3.1 Anderson Mixing Scheme

The simple mixing scheme usually needs many iterations before convergence is reached since it does not save all the information gained from previous iterations and, even worse, fixes the linear combination of input and output vector without any jurisdiction. For self-consistent loop each iteration itself costs a lot of CPU time and thus reducing their number by accelerating convergence would save computer resources or else allow for the larger systems to be investigated. The simple mixing scheme takes into account only the input and output vector of the actual iteration to calculate the new input vector. But the mixing scheme introduced by Anderson [70], in addition, considers the vectors of the previous iterations and combines them in wisely. Though the Anderson scheme is one of the most powerful methods which leads to very fast convergence, it is still quite simple as concerns the underlying concept. Now we fix the coefficients $x_j^{(l)}$ by the requirement that they yield that particular linear combination which minimizes the norm of the general residual vector from the following relation

$$\sum_{j=1}^{M} \langle \triangle \mathbf{V}^{(l)} - \triangle \mathbf{V}^{(l-i)} | \triangle \mathbf{V}^{(l)} - \triangle \mathbf{V}^{(l-j)} \rangle x_j^{(l)} = \langle \triangle \mathbf{V}^{(l)} - \triangle \mathbf{V}^{(l-i)} | \triangle \mathbf{V}^{(l)} \rangle \quad (3.51)$$

which has to be solved in order to yield the coefficients $x_j^{(l)}$ and, hence, the linear combination with the shortest residual vector. Here, $0 \leq M \leq l-1$ and $i = 1, ..., M$. Considering M previous iterations the estimated values

$$|\overline{\mathbf{V}}^{(l)}\rangle = |\mathbf{V}^{(l)}\rangle + \sum_{j=1}^{M} x_j^{(l)} (|\mathbf{V}^{(l-j)}\rangle - |\mathbf{V}^{(l)}\rangle) \quad (3.52)$$

and

$$|\overline{\triangle \mathbf{V}}^{(l)}\rangle = |\triangle \mathbf{V}^{(l)}\rangle + \sum_{j=1}^{M} x_j^{(l)} (|\triangle \mathbf{V}^{(l-j)}\rangle - |\triangle \mathbf{V}^{(l)}\rangle). \quad (3.53)$$

Now we fix the potential for the subsequent iteration by

$$|\mathbf{V}^{(l+1)}\rangle = |\overline{\mathbf{V}}^{(l)}\rangle + m|\overline{\triangle \mathbf{V}}^{(l)}\rangle. \quad (3.54)$$

The updated potential, the solution of Anderson mixing scheme is incorporated in Hamiltonian matrix to calculate charge density through recursive Green's function algorithm. This calculated charge density is used in Poisson's solver to calculate potential again. This process continues until the loop converges. About 4-11 iteration in self-consistent loop is sufficient for convergence. If the loop converges by using Eq. (3.47) we calculate current.

Chapter 4

Strain Effect on Single-Walled and Double-Walled Carbon Nanotubes

In this chapter we study the effect of both the uniaxial ($\leq$ 10 %) and the torsional strain ($\leq 5^o$) on the band gap of the single-walled as well as double walled carbon nanotubes. Previously Yoon *et al.* considered uniaxial strain $\leq$10% and torsional strain $\leq 5^o$ in their literature [49]. Through experiment up to 12% tensile strain is applied on carbon nanotube [71,72]. The Young's modulus and mechanical strength of carbon nanotube are around 2 TPa and 50 GPa, respectively [72]. We have compared the band gap of the single-walled and double-walled nanotubes. We have taken into consideration of those single-walled nanotube from which double-walled nanotube is constructed. We show the variation of band gap of SW and DW CNTs with uniaxial and torsional strain using p_z orbital basis quantum simulation. The DW nanotube is generated from two semiconducting, zigzag, SW nanotubes. For DWs [(19, 0) (10, 0)], [(19, 0) (9, 0)] and [(19, 0) (8, 0)] the wall separations are 0.35 nm, 0.39 nm and 0.42 nm, respectively [59–61]. It is shown that the band gap of DW CNT is the minimum of the band gaps of the two tubes from which it is produced. We have also investigated the effect of intertube bonding energy on band gap of DW CNT. For DW CNT the band gap variation with uniaxial or torsional strain depends on the band gap variation of each CNT from which DW CNT is constructed. The band gap of DW CNT is the minimum of band gaps of two CNTs it constituted with for every value of strain. The bonding energy between inner and outer tubes atoms has insignificant effect on band gap.

4.1 Simulation Model

Figures 4.1 (a) and (b) show the single-walled and double-walled carbon nanotubes structures, respectively. Figures 4.1 (c), (d), and (e) exhibit, respectively, unstrained, uniaxially strained, and torsionally strained forms of same single-walled CNT. Here, L_1, L_4, L_n etc. in Figure 4.1 (c) are different layers of carbon nanotube. The CNT is modeled using p_z orbital basis of carbon atom [35, 49, 63]. Without strain, the bonding energy between two atoms of inner tube and outer tube is calculated from [73–76]

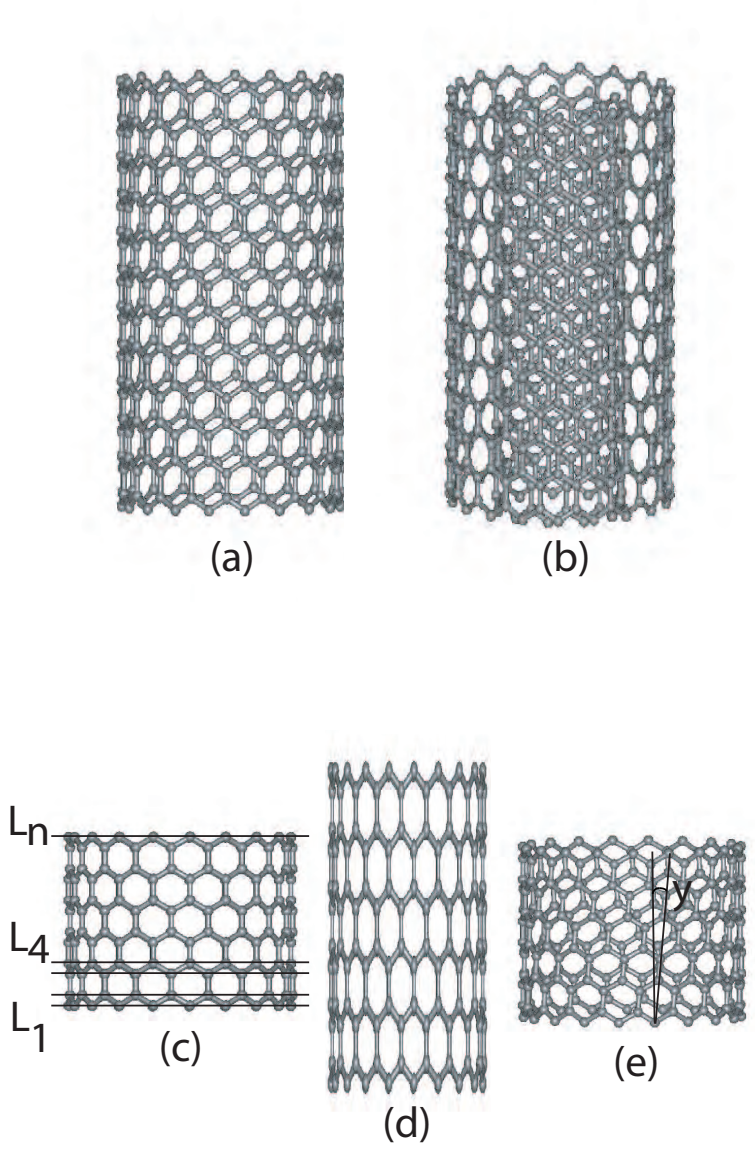

Figures 4.1: Structure of (a) unstrained single-walled tube, (b) unstrained double-walled tube, (c) single-walled tube before strain, (d) single-walled tube after tensile strain, and (e) single-walled tube after torsional strain.

$$\begin{aligned}\gamma^0(\mathbf{R_1},\mathbf{R_2}) &= V^0_{pp\sigma}\exp\left(-\frac{d-c/2}{\delta}\right)\left(\frac{\mathbf{p}_1.\mathbf{d}}{d}\right)\left(\frac{\mathbf{p}_2.\mathbf{d}}{d}\right)\\ &\quad -V^0_{pp\pi}\exp\left(-\frac{d-a_0}{\delta}\right)[(\mathbf{p}_1.\mathbf{e})(\mathbf{p}_2.\mathbf{e})\\ &\quad +(\mathbf{p}_1.\mathbf{f})(\mathbf{p}_2.\mathbf{f})], \qquad (4.1)\end{aligned}$$

where, for unstrained case, $\mathbf{R_1}$ and $\mathbf{R_2}$ are the atomic positions in inner tube and outer tube respectively, $V^0_{pp\sigma}$ and $V^0_{pp\pi}$ are the energy integrals between π orbitals decomposed into the directions parallel and perpendicular, respectively, to the vector $\mathbf{d} = \mathbf{R}_1 - \mathbf{R}_2$, $\mathbf{p}_1$ and $\mathbf{p}_2$ are unit vectors directed along π orbitals at $\mathbf{R}_1$ and $\mathbf{R}_2$, respectively, $d = |\mathbf{d}|$, $\mathbf{e}$ and $\mathbf{f}$ are unit vectors perpendicular to $\mathbf{d}$ and to each other, a_0 is the distance between two nearest neighbor carbons in two dimensional graphite, c is the lattice constant along the c axis in bulk graphite, and δ is the decay rate of π orbital. Within the layer, the on-site energy is ϵ_p and the nearest-neighbor carbon-carbon bonding energy is $V^0_{pp\pi}$ [49, 63].

When strain is applied, within tube, we assume that the on-site energy does not change and the carbon-carbon bond energy changes following Harrison's formula $V_{pp\pi} = V^0_{pp\pi}(r_0/r)^2$ [39, 49, 77]. Here r_0 and r are the carbon-carbon bond length of the unstrained and strained CNTs, respectively. A detail explanation about incorporating strain to bond lengths and calculating lattice positions is provided in chapter 2.

After computing the position of all atoms, we have determined the distance, r between two atoms of inner tube and outer tube. Then, the bonding energy between these each pair of atoms is calculated by using the relation $\gamma = \gamma^0(r_0/r)^2$ [39,49,77].

Next, we have formed Hamiltonian matrix using atomistic Hamiltonian (also known as full band Hamiltonian) concept [63, 69]. According to atomistic Hamiltonian concept the element of Hamiltonian matrix is the bonding energies of all atoms with each other. The Hamiltonian parameter values are taken from [78]. The eigen values of the Hamiltonian matrix is the eigen energies of the carbon nanotube. After forming Hamiltonian matrix, we determine band diagram using this matrix. The band gap is the difference of energy between the bottom of the conduction band and the peak of the valence band.

4.2 Numerical Results and Discussions

The results shown here, we get by following the method described in section 4.1. In Figures 4.2 the energy band diagram in unstrained case is shown. Dotted lines in Figure 4.2 (a) represent the energy band diagram for (10, 0) SW CNT. The bottom of the conduction band of (19, 0) CNT is lower than the that of (10, 0) CNT and the peak of the valence band of (19, 0) CNT is higher than that of (10, 0) CNT indicating lower band gap in (19, 0) CNT in unstrained case. The energy band diagram of DW [(19, 0) (10, 0)] CNT in Figure 4.2 (b) represents that it is a combination of energy band of SW (19, 0) and SW (10, 0) CNTs. So the band gap of DW [(19, 0) (10, 0)] CNT will be equal to the band gap of SW (19, 0) CNT.

The energy band diagram is sketched in Figure 4.3 (a) for SW (19, 0) and (10, 0) CNTs and in (b) for DW [(19, 0) (10, 0)] CNT with 5 % tensile strain.

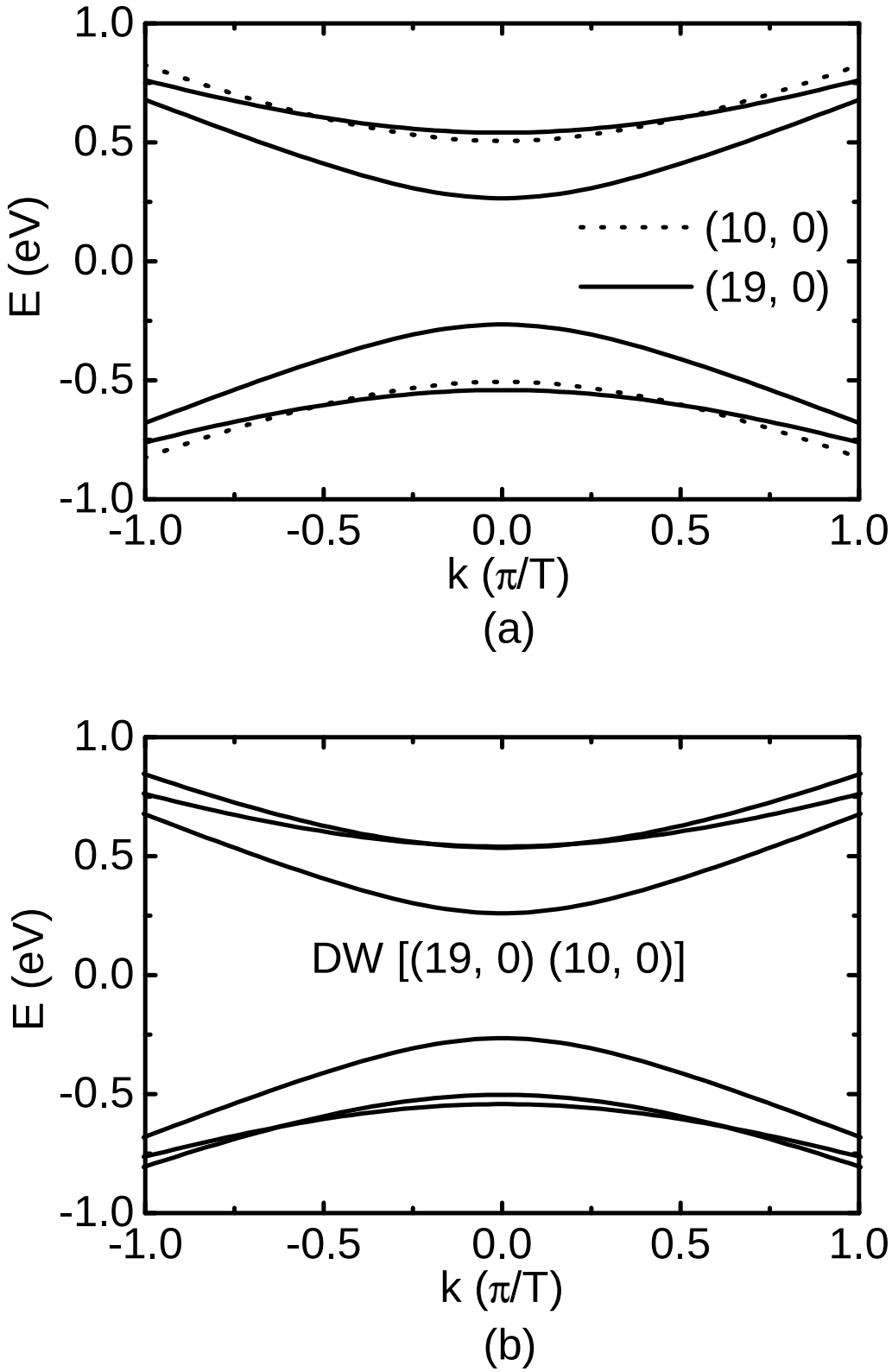

Figures 4.2: Partial energy band diagram of (a) single-walled and (b) doubled-walled CNTs without strain.

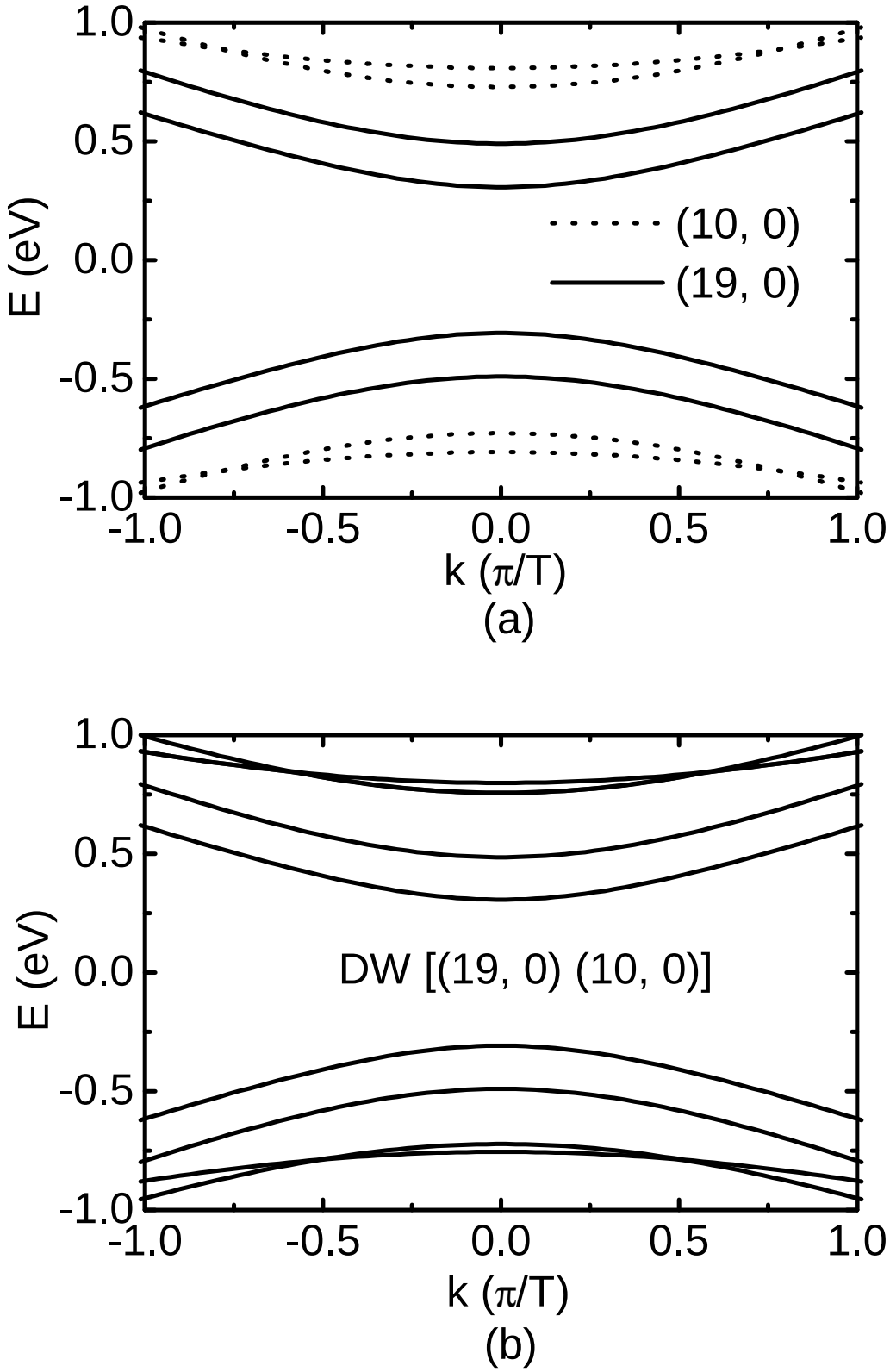

Figures 4.3: Partial energy band diagram of (a) single-walled and (b) doubled-walled CNTs with 5 % tensile strain.

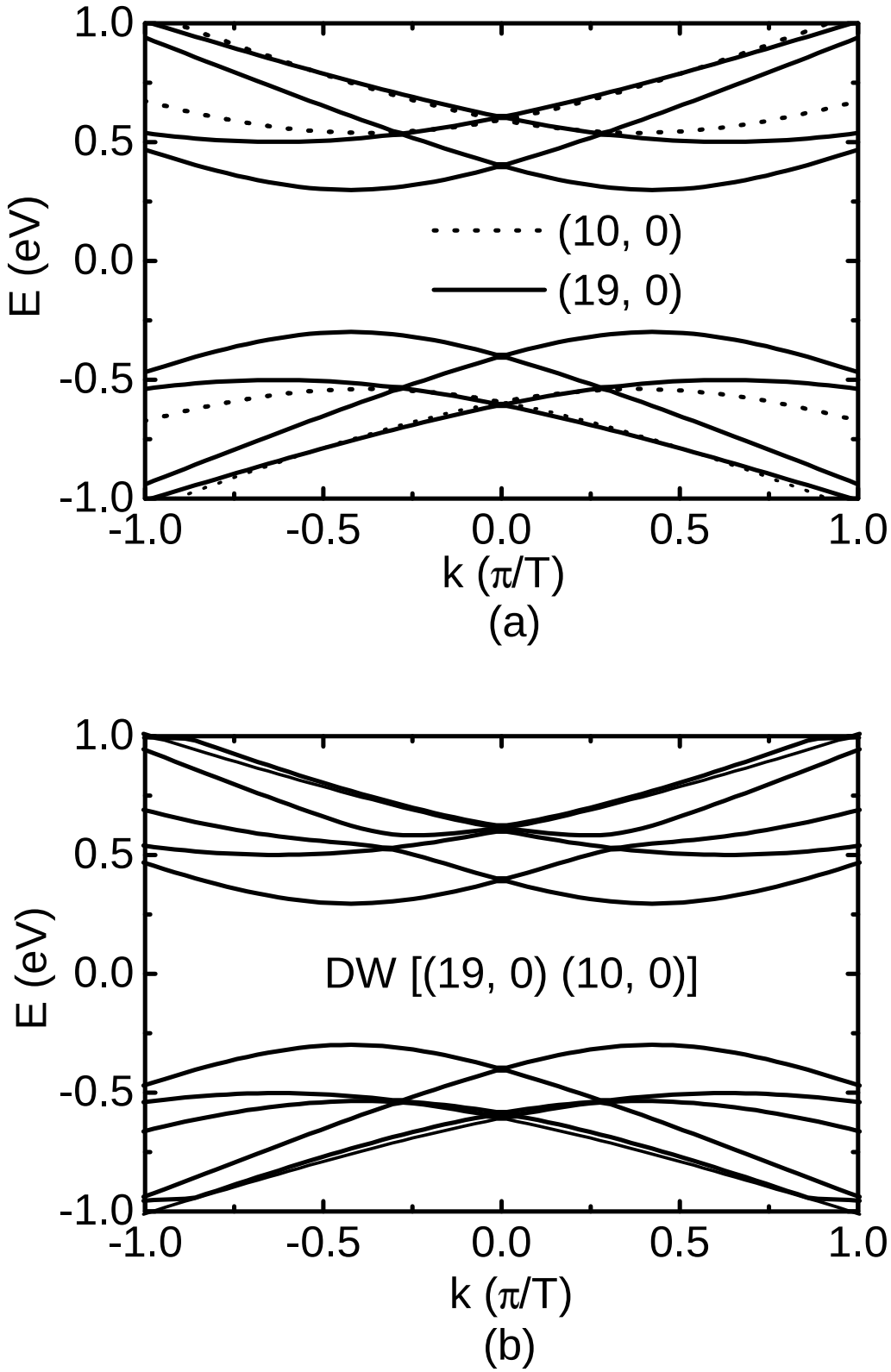

Figures 4.4: Partial energy band diagram of (a) single-walled and (b) doubled-walled CNTs with 4 degree torsional strain.

Experimentally tensile strain up to 12 % is applied on carbon nanotube [71,72]. So, we choose a tensile strain $\leq$ 12 % randomly to observe the effect of uniaxial strain on E-k diagram. With the application of tensile strain the carbon-carbon bond length increases which corresponds to increase in tube length. This is quite visible in Figure 4.1 (d). With this strain for both the SW (19, 0) and (10, 0) CNTs each the bottom of conduction band shifts upward but still the bottom of the conduction band of (19, 0) CNT is lower than the that of (10, 0) CNT. The peak of valence band for both (19, 0) and (10, 0) CNT each shifts downward and again the peak of (19, 0) is higher than that of (10, 0) CNT corresponds to lower band gap in (19, 0) CNT. Alike unstrained case, the energy band diagram of DW [(19, 0) (10, 0)] CNT is still the combination of energy band diagram of SW (19, 0) and (10, 0) CNTs and obviously the band gap of DW CNT is determined by the band gap of (19, 0) CNT.

The shape of energy band diagram of zigzag CNT with the application of torsional strain is quite different from the shape with unstrained and uniaxially strained. Previously torsional strain up to 5^o is considered [49]. The energy band diagrams for SW (19, 0) and (10, 0) CNTs and for DW [(19, 0) (10, 0)] CNT are stated in Figures 4.4. Here, also the band gap of SW (19, 0) CNT is lower than that of (10, 0) CNT. But unlike unstrained and uniaxially strained case we here get minimum energy difference between valence and conduction band at $k \neq 0$. Like before the band gap of DW [(19, 0) (10, 0)] CNT is the lowest of SW (19, 0) and (10, 0) CNTs.

The band gap variation of SW (19, 0) and (10, 0) CNTs with the application of uniaxial strain is plotted in Figure 4.5 (a). In unstrained case the conduction behavior (metallic or semiconducting) of the SW tube is determined by mod (n-m,3) rule [35, 39, 79, 80]:

$$\begin{aligned} \text{mod (n-m,3)} = 0 &\rightarrow \text{metallic} \\ = 1 \text{ or } 2 &\rightarrow \text{semiconducting.} \end{aligned}$$

Here mod stands for modulo or remainder. For strained (uniaxial or torsional) case SW tubes having same mod follow same trend of band gap variation with strain [35, 39, 49]. Both (19 , 0) and (10, 0) SW CNTs have mod (n-m,3) = 1, which indicates for small tensile strain the band gap proportionately increases and for compressive strain the band gap decreases which is quite discernable in this figure [35, 39, 49]. With the application of uniaxial strain in both inner and outer tubes of DW [(19, 0) (10, 0)] CNT, this DW CNTs energy band gap versus uniaxial strain plot shown in Figure 4.5 (b) by solid line follows the minimum path of the same plot for SW (19, 0) and (10, 0) CNTs in Figure 4.5 (a). From -10% to –7% compressive strain the band gap of DW CNT follows SW (10, 0) strained CNT; with further reduction of compressive strain the band gap of SW (10, 0) CNT becomes higher than the that of (19, 0) SW CNT. So, now it follows the path of (19 , 0) SW CNT for rest of the curve up to 10 % tensile strain. If we apply the uniaxial strain only in outer tube and leave the inner tube unstrained, then in that case the energy band gap of this DW CNT follows the minimum of band gaps of unstrained (10, 0) and strained (19, 0) CNTs, which is quite noticeable in Figure 4.5 (b). The band gap variation of unstrained inner tube (10, 0) and strained outer tube (19, 0) is sketched in dashed line. The band gap of unstrained (10, 0) SW CNT is 1.0 eV. Since the band gap of SW (19, 0) uniaxially strained CNT for -10% to 10% strain is below 1.0 eV, so the band gap of DW unstrained inner tube (10, 0) and strained

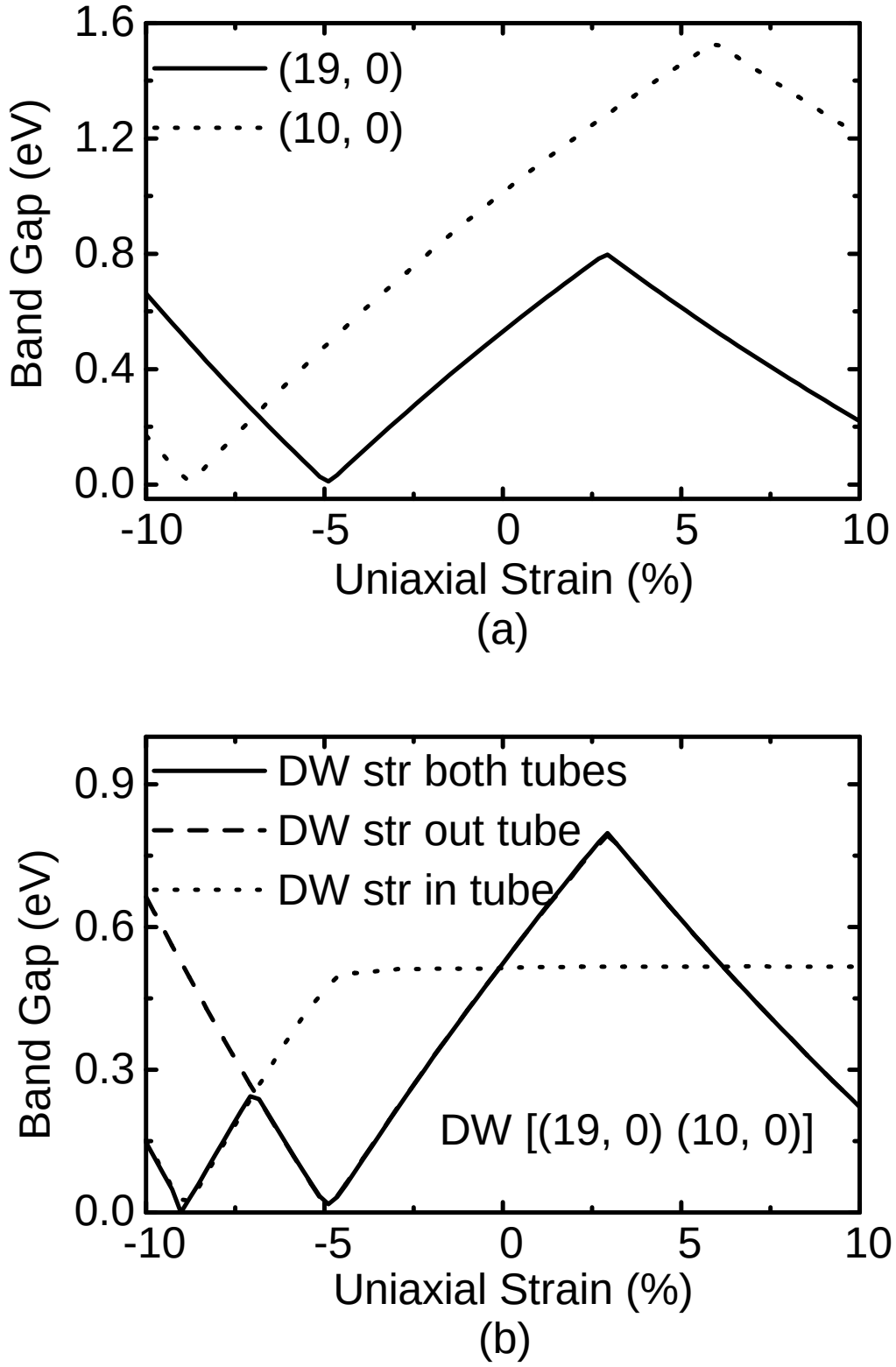

Figures 4.5: Band gap versus uniaxial strain curves for SW (19, 0) and (10, 0) and DW [(19, 0) (10, 0)] CNTs. Compressive uniaxial strain is represented as negative strain and tensile uniaxial strain is represented as positive strain.

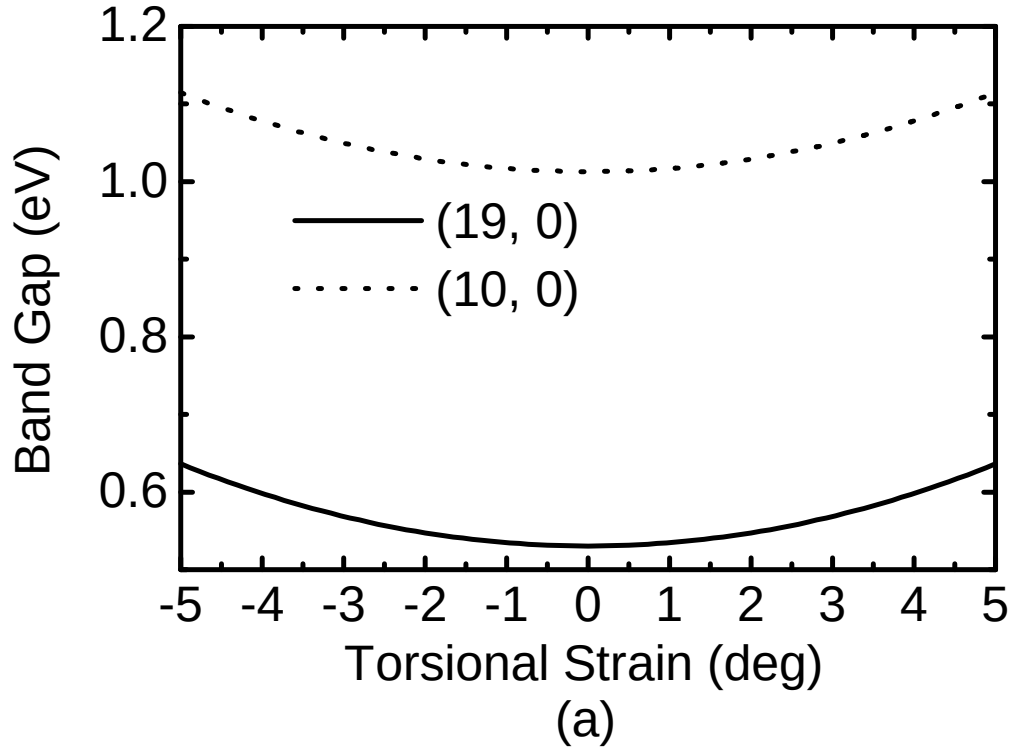

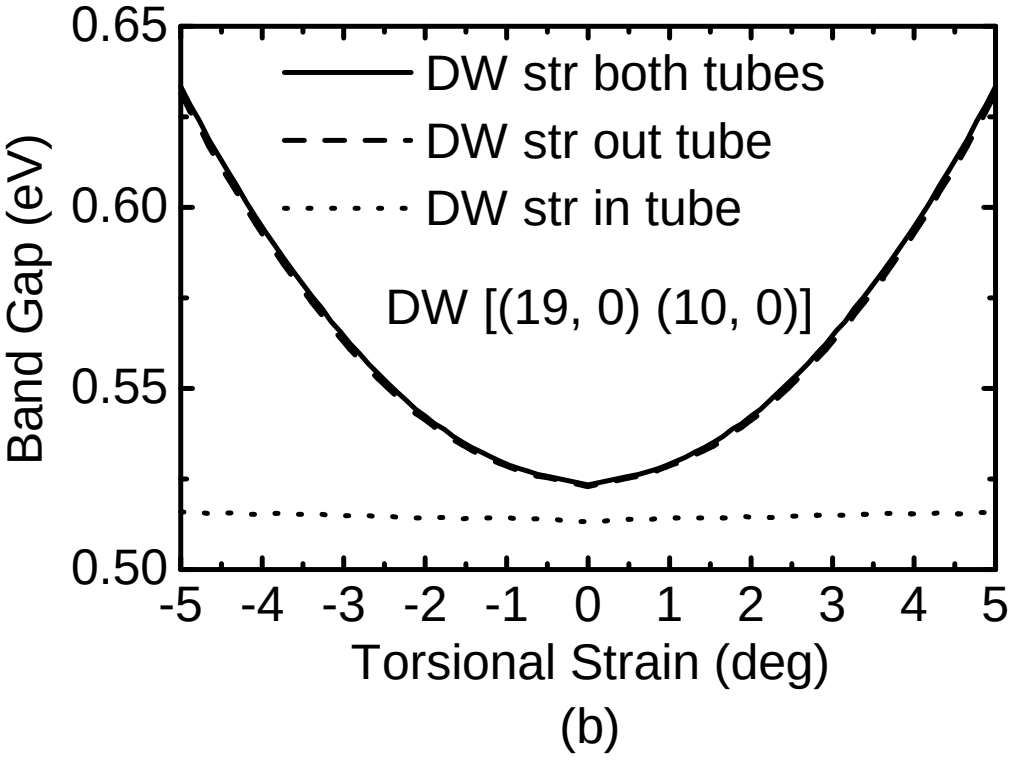

Figures 4.6: Band gap versus torsional strain curves for SW (19, 0) and (10, 0) and DW [(19, 0) (10, 0)] CNTs. Torsional strain in anti-clockwise direction is represented as negative strain and in clockwise direction is represented as positive strain.

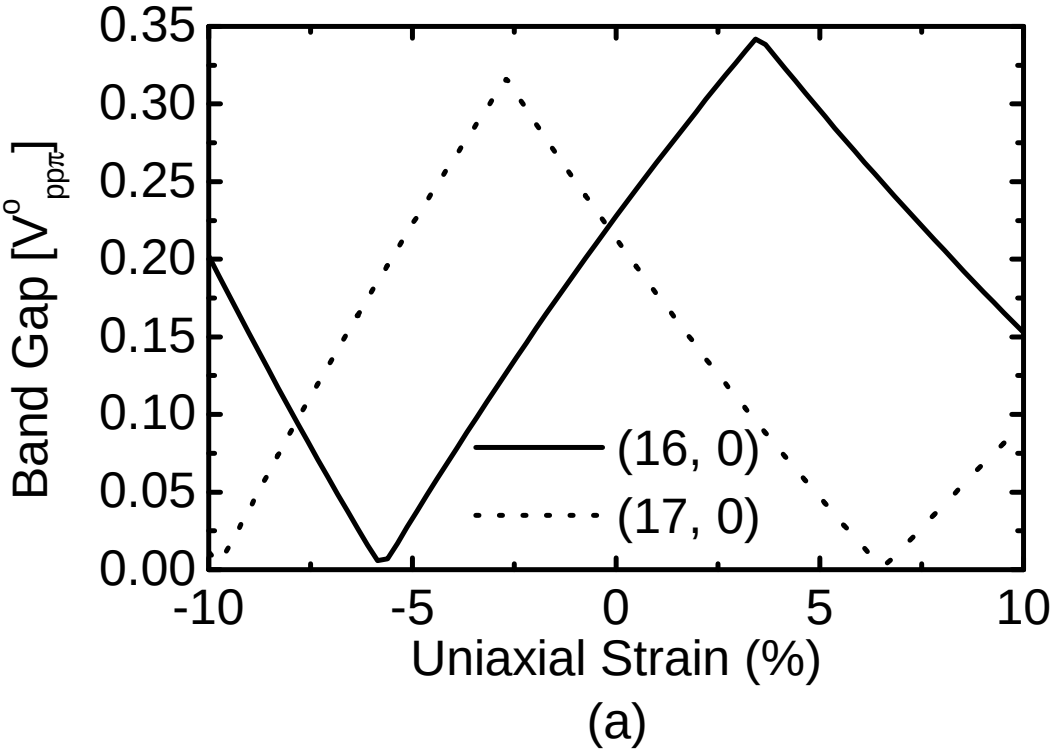

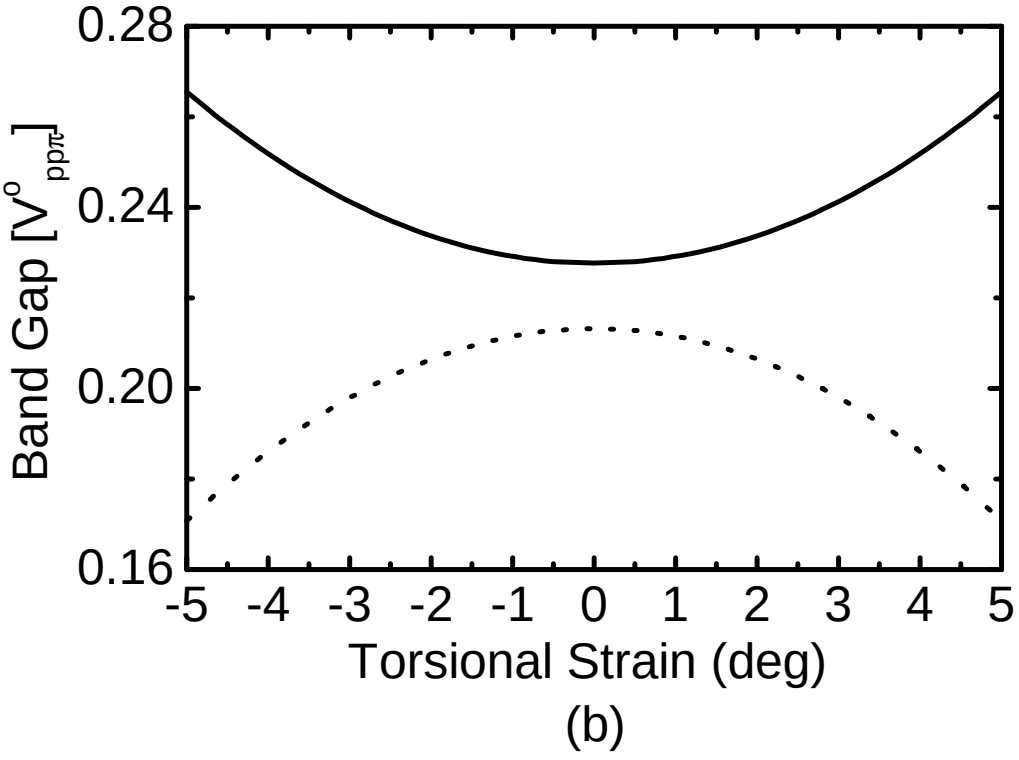

Figures 4.7: The band gap versus (a) uniaxial strain and (b) torsional strain curves for SW (16, 0) and SW (17, 0) CNTs. Here, $V^0_{pp\pi}$ is the nearest-neighbor carbon-carbon bonding energy in unstrained case.

outer tube follows the band gap variation of SW (19, 0) uniaxially strained CNT. The band gap variation of uniaxially strained inner tube and unstrained outer tube DW CNT is shown by dotted line in Figure 4.5 (b). The band gap of unstrained SW (19, 0) CNT is 0.53 eV. So, from -10% to -5% compressive strain the band gap of SW (10, 0) CNT is below 0.53 eV the band gap of SW (19, 0) unstrained CNT. After -5% compressive strain the band gap of (10, 0) strained SW CNT becomes higher so the band gap of this DW CNT follows the band gap of (19, 0).

For SW (19, 0) and (10, 0) and for DW [(19, 0) (10, 0)] CNTs, the band gap variation with torsional strain is shown in Figures 4.6 (a) and (b), respectively. According to mod(n-m,3) = 1, the band gaps of both (19, 0) and (10, 0) SW CNTs increase with torsional strain [35, 39, 49]. For same amount of strain the band gap of (19, 0) SW CNT is always lower than that of (10, 0). With the application of torsional strain in both inner and outer tubes of DW [(19, 0) (10, 0)] CNT the band gap variation shown in solid line goes after the minimum band gap of SW (19, 0) and (10, 0) CNT as like uniaxial strain we have observed above. The band gap of DW CNT with torsional strain in outer tube only, denoted by dashed line follows the band gap variation of SW torsionally strained (19, 0) CNT, since its band gap is always lower than that of unstrained (10, 0) CNT. But for torsional strain in inner tube only the band gap of this DW is insensitive of torsional strain because the band gap of torsional strained SW (10, 0) CNT is always higher than that of unstrained SW (19, 0) CNT and band gap of DW CNT is the minimum of the two tubes from which it is constructed. For the verification of our work we have performed strain analysis on SW (16, 0) and SW (17, 0) tubes [49]. The result are provided in Figures 4.7. The results almost match with the previous report [49].

To generalize that the band gap of the DW CNT is always the minimum of the two tubes from which it is generated in every possible case, we also perform the test for DW [(19, 0) (9, 0)] and [(19, 0) (8, 0)] CNTs. The SW (9, 0) and (8, 0) follow mod (n-m,3) = 0, mod (n-m,3) = 2, respectively. In Figures 4.8 the band gap versus uniaxial strain plots and in Figures 4.9 the band gap versus torsional strain plots for SW (19, 0) and (9, 0) and for DW [(19, 0) (9, 0)] CNTs are displayed.

According to mod 3 rule the SW (9, 0) CNT behaves as metallic [35]. However, the application of uniaxial or torsional strain open the band diagram converting it to semiconducting tube [35]. As before the band gap variation of DW CNT with both the inner and outer tubes uniaxially strained symbolized by solid line, follows the minimum of two band gaps of strained SW (19, 0) and (9, 0) CNTs. For strained in outer tube only the band gap of this DW CNT is numb of strain. But for strain only in inner tube the band gap remains insensitive from -10% to -5%, then it follows SW (9, 0) strained CNT, after 5% it again becomes insensitive. The band gap variation with uniaxial strain only in outer tube and also only in inner tube is represented by dashed line and dotted line, respectively. As Figure 4.9 (a) the band gaps of both SW (19, 0) and (9, 0) CNT increase with the application of strain; but the band gap of (9, 0) CNT is always lowest. So, the band gap of DW CNT indicated by solid line shown in Figure 4.9 (b) is always follows (9, 0). The band gap of this DW CNT with strain only in outer tube is insensitive of strain, but the band gap with strain only in inner tube merges with band gap of strain in both.

Since the band gap of SW (8, 0) CNT is always higher than that of SW (19, 0), for same uniaxial strain and even it is always higher than that of unstrained SW (19, 0) as conspicuous in Figure 4.10 (a), the band gap of corresponding DW CNT

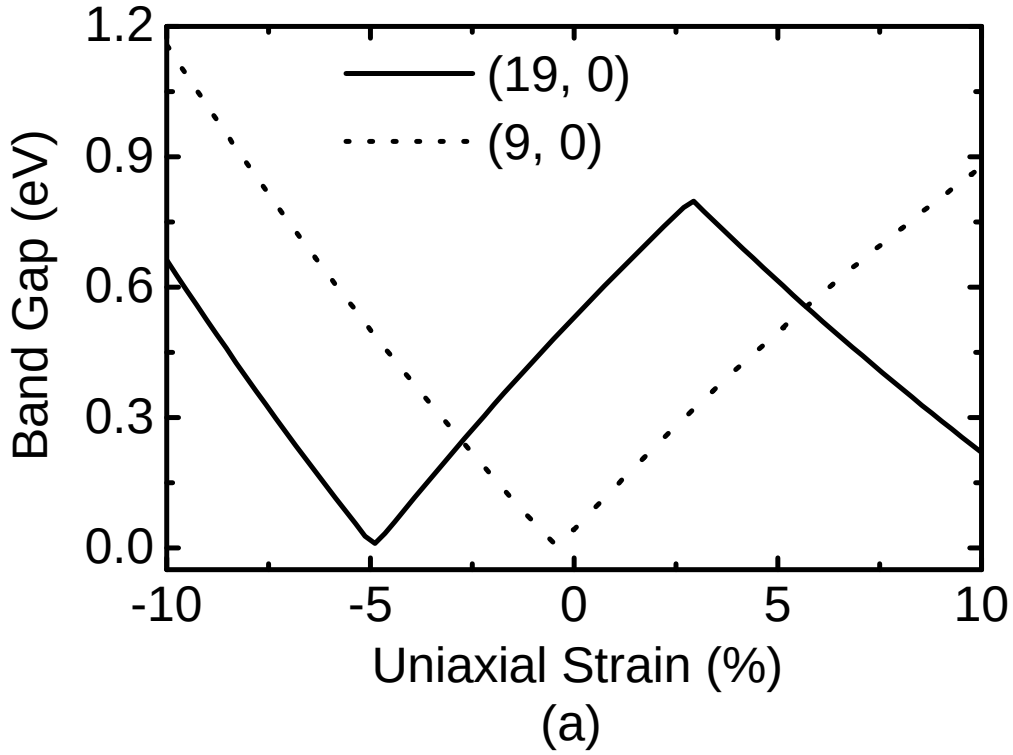

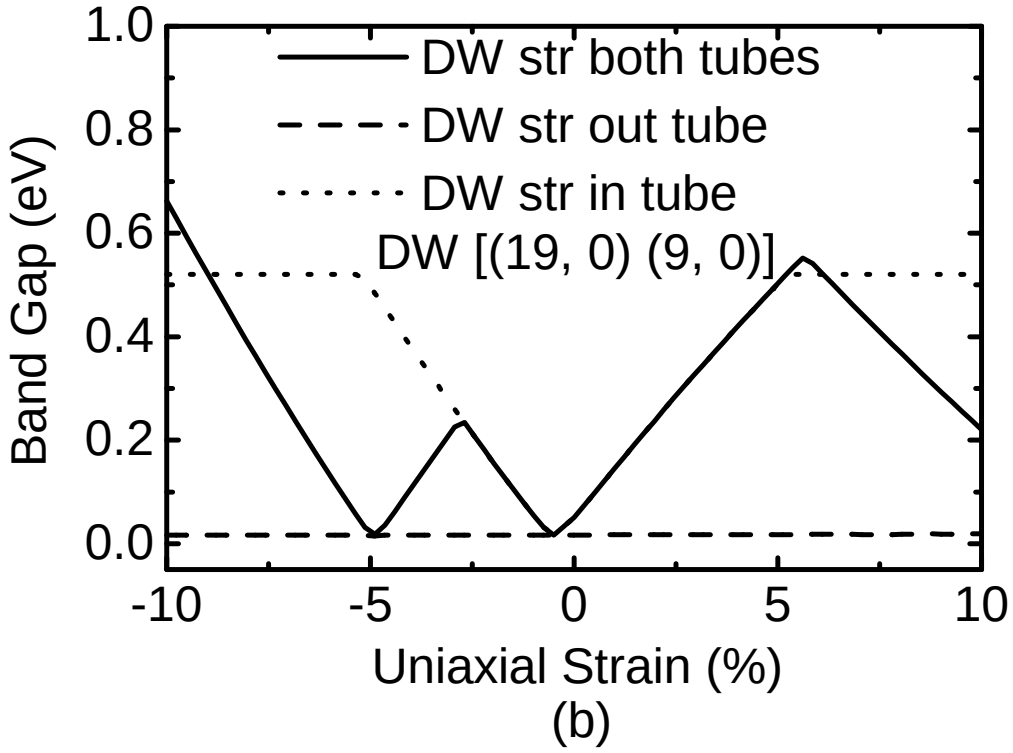

Figures 4.8: Band gap versus uniaxal strain curves for SW (19, 0) and (9, 0) and DW [(19, 0) (9, 0)] CNTs. Compressive uniaxial strain is represented as negative strain and tensile uniaxial strain is represented as positive strain.

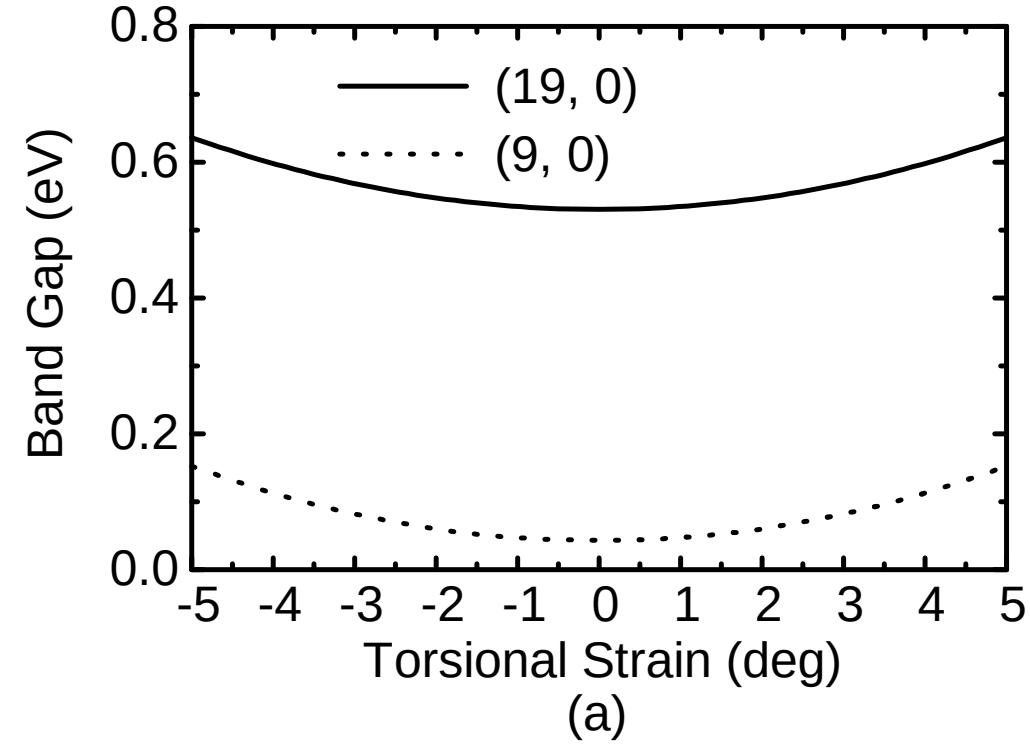

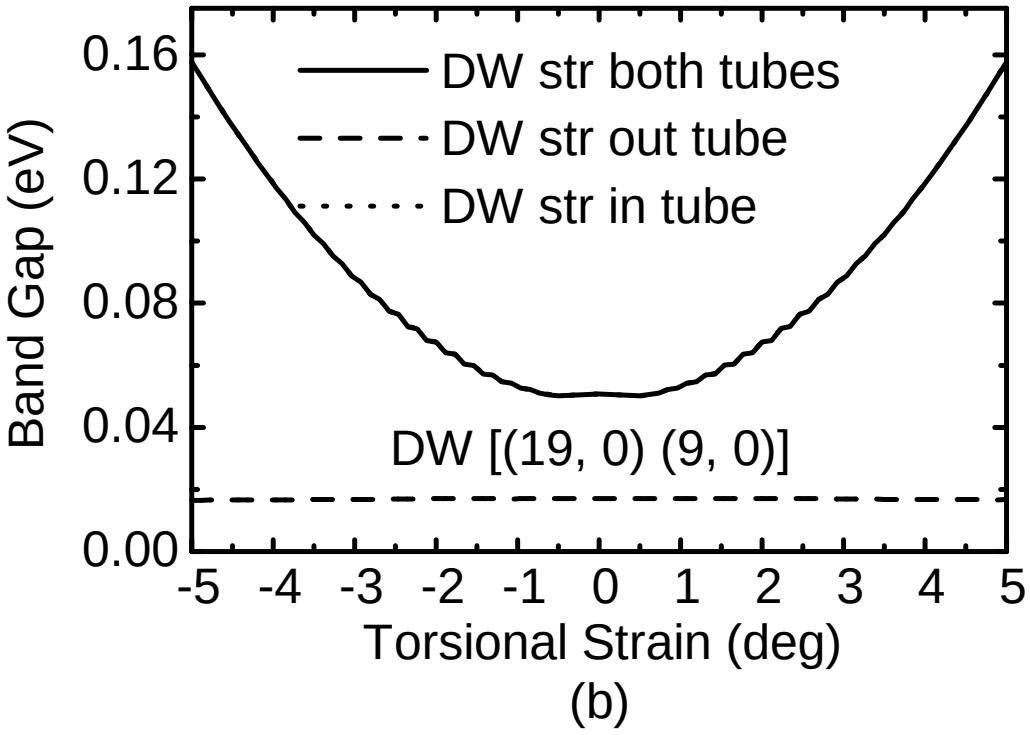

Figures 4.9: Band gap versus torsional strain curves for SW (19, 0) and (9, 0) and DW [(19, 0) (9, 0)] CNTs. Torsional strain in anti-clockwise direction is represented as negative strain and in clockwise direction is represented as positive strain.

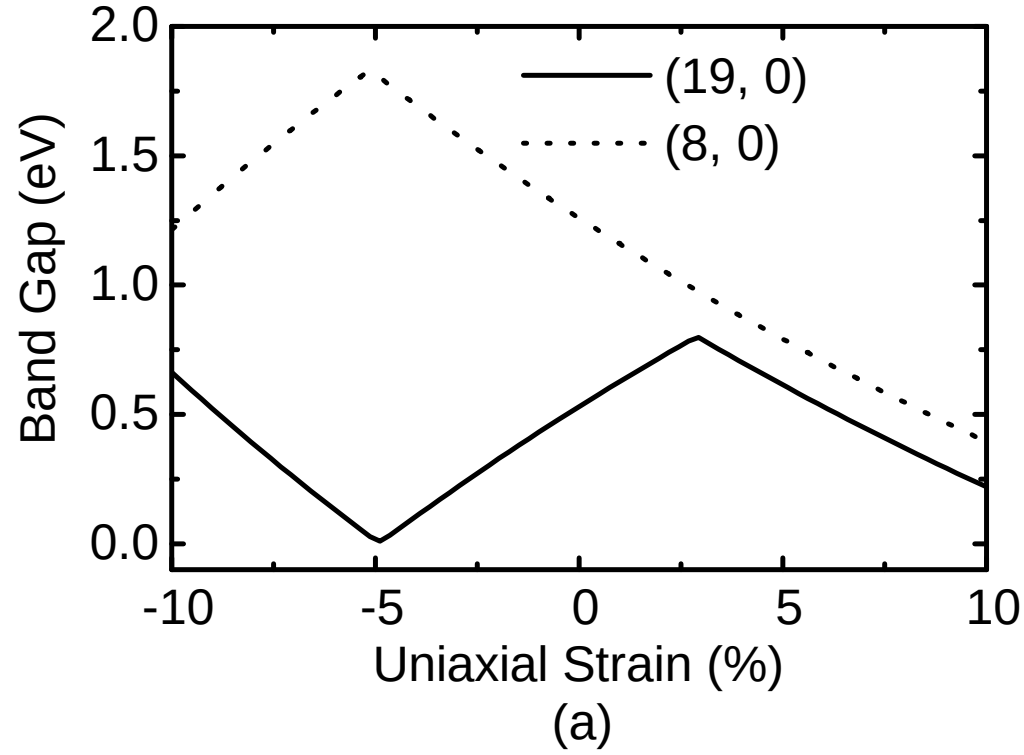

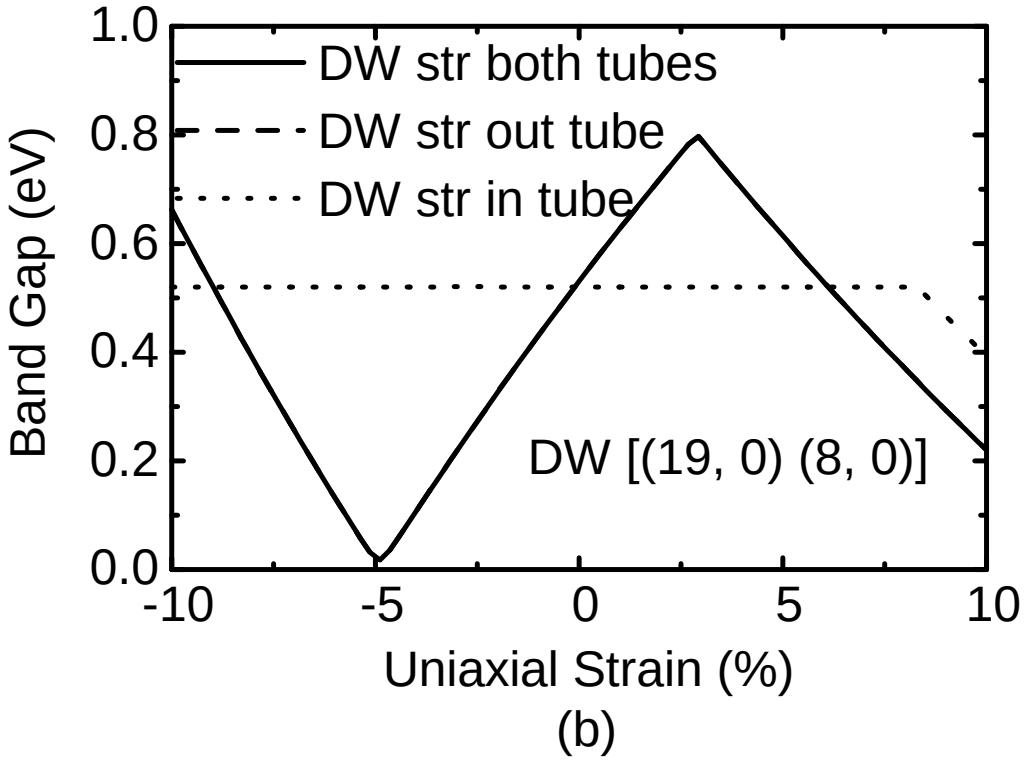

Figures 4.10: Band gap versus uniaxial strain curves for SW (19, 0) and (8, 0) and DW [(19, 0) (8, 0)] CNTs. Compressive uniaxial strain is represented as negative strain and tensile uniaxial strain is represented as positive strain.

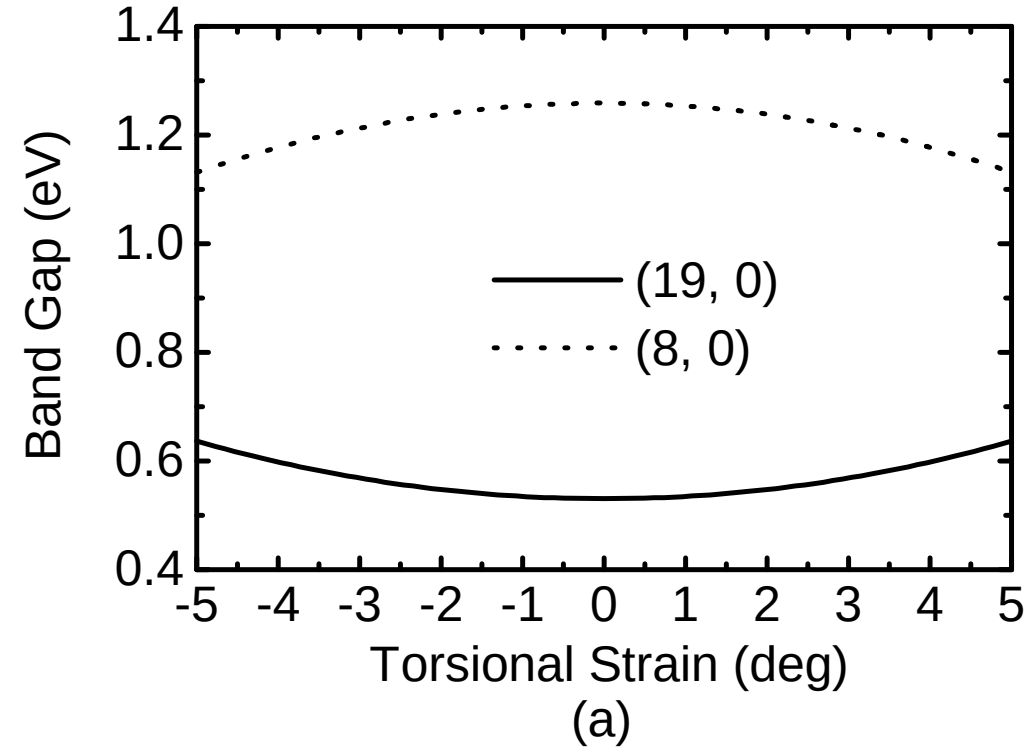

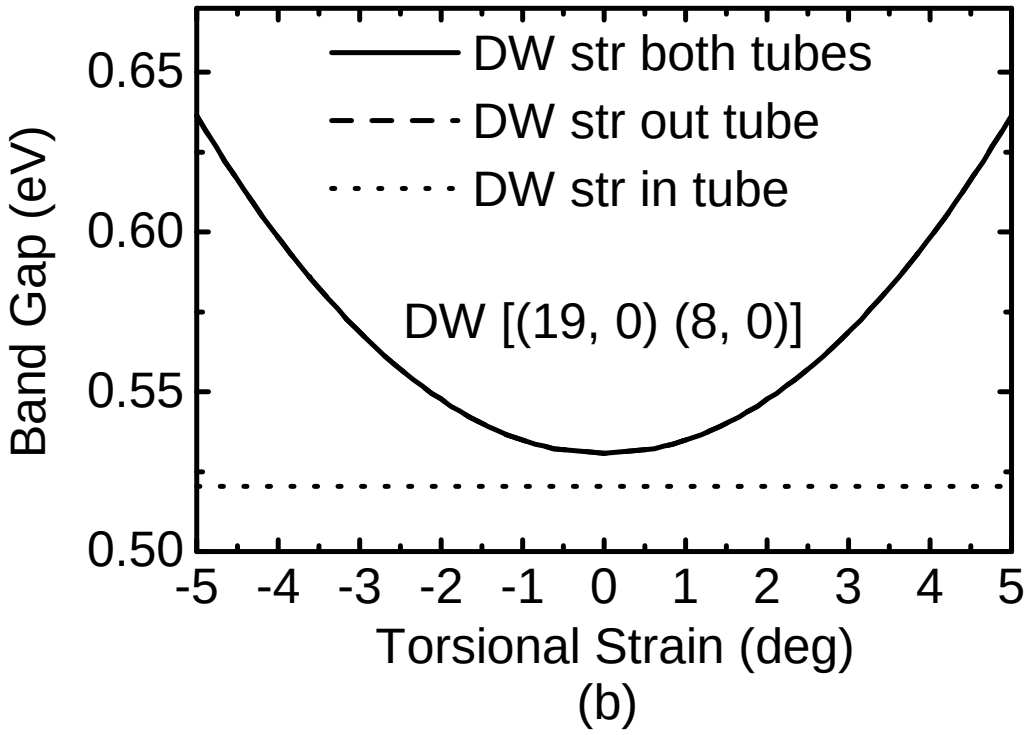

Figures 4.11: Band gap versus torsional strain curves for SW (19, 0) and (8, 0) and DW [(19, 0) (8, 0)] CNTs. Torsional strain in anti-clockwise direction is represented as negative strain and in clockwise direction is represented as positive strain.

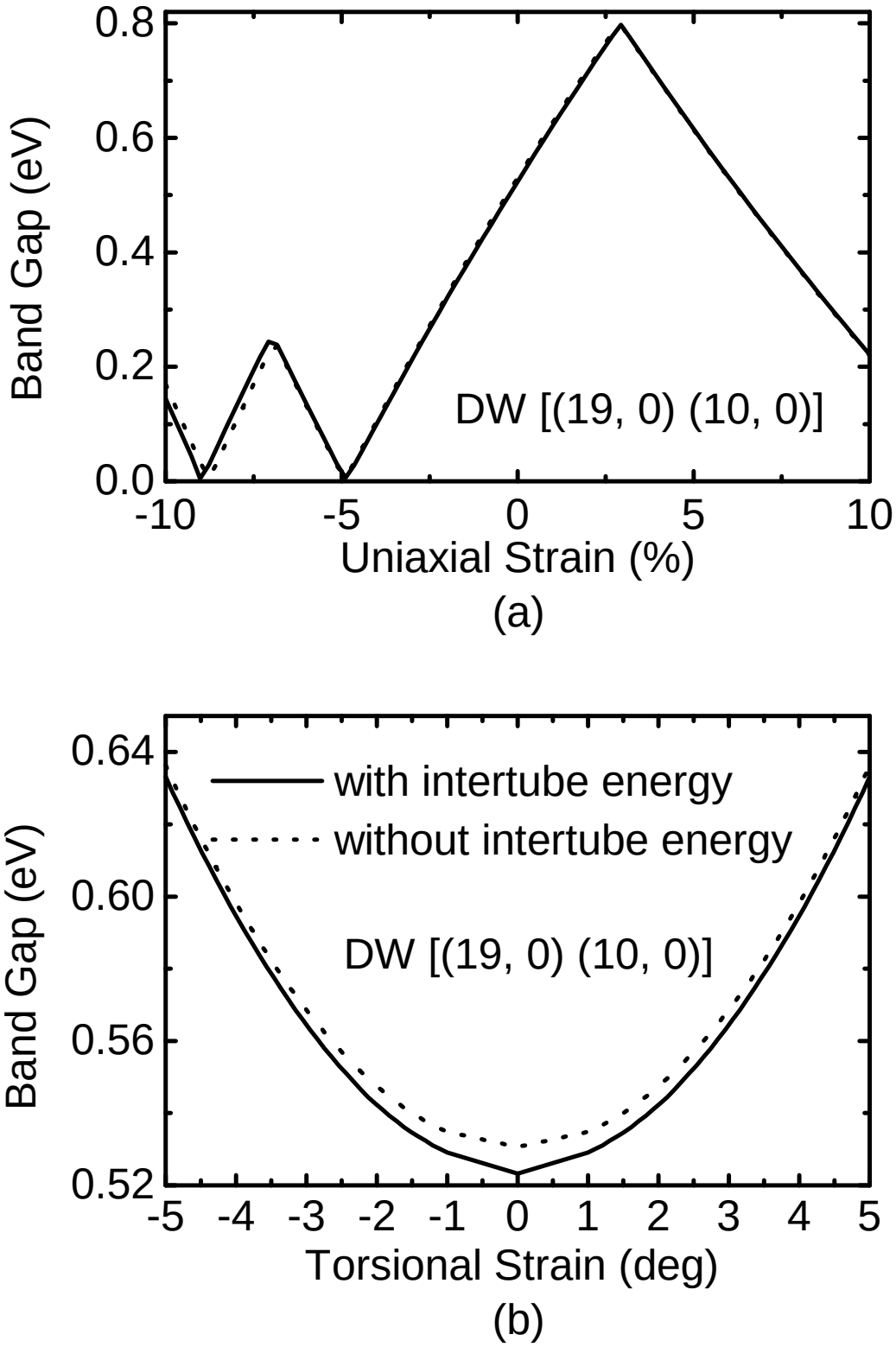

Figures 4.12: Effect of intertube bonding energy on band gap versus strain curve for DW [(19, 0) (10, 0)] CNTs.

with strain both in inner and outer tube, and outer tube only, merges each other and both follow the band gap versus uniaxial strain curve of SW (19, 0) CNT. But, for strain only in inner tube most of the cases the band gap is insensitive of strain except uniaxial strain greater than 8%. With the application of torsional strain the band gap of SW (8, 0) CNT decreases, noticeable in Figure 4.11 (a) according to mod (n-m,3) rule. The band gap of DW CNT with torsional strain in both inner and outer tube or inner tube only tracks the that of SW (19, 0) CNT. The band gap for strain only in inner tube is insensitive of torsional strain.

The effect of intertube bonding energy on band gap for different type strains is shown in Figures 4.12. The atomic bonding energy between inner and outer tube atoms have negligible effect on band gap [56]. The solid line represents band gap variation with strain considering intertube bonding energy and the dotted line for zero intertube bonding energy.

In conclusion, band gap variations of DW CNT and the SW CNTs from which DW CNT is generated with strain are invesigated using a π-bond atomistic quantum simulation. It is found that the band gap of the DW CNT is always the minimum of the two tubes from which it is produced. To generalize we have considered three different type zigzag inner tubes for same outer tube. At last, we explored that the intertube bonding energy between inner and outer tubes atoms has trifling effect on band gap.

Chapter 5

Strain Effects on Schottky-Barrier Single-Walled and Double-Walled Carbon Nanotube Transistors

From previous chapter we observe that band gap of DW CNT is the minimum of band gaps of two CNTs it constructed with for every value of strain. In this chapter the effects of uniaxial and torsional strain on the performance of both SW (19, 0) and DW [(19, 0) (10, 0)] zero-Schottky-barrier CNTFETs are analyzed through atomistic quantum simulation. For the CNT devices we have applied strain to channel materials only and other parts have been left unstrained. For DW CNTFET we have considered strain on both tubes. We have limited our analysis with tensile and compressive strains below 2 % and torsional strain below 6^o [49]. The Young's modulus and mechanical strength of carbon nanotube are around 2 TPa and 50 GPa, respectively [72]. The number of unit cell in our channel is 114 for the whole analysis of this chapter. With the application of the tensile strain and torsional strain both the off-state current and on/off current ratio improve greatly. The on-state current improves with compressive strain. But, this improvement is comparatively small for both devices. Previously off-state and on-state currents improvement with strain is reported for SW CNTFET [49]. The off-state current, on-state current, and on/off current ratio improvement is slightly better in SW CNTFET. With the increase of the compressive strain the I-V curves shift upward verifying high conductivity [49]. The opposite result occurs with tensile strain. With the increase of the torsional strain the band gap increases corresponding to low conductivity. So the I-V characteristics shift downward with the torsional strain. The I-V characteristics saturate at gate voltage $V_{GS} \geq E_g/(2q)$, one important finding of DW CNTFET with or without strain. Thermal component as well as tunnel component of I-V curves saturate at this region. Thermal component saturates for the saturation of the peak of conduction band near source-channel interface after $V_{GS} \geq E_g/(2q)$ for both SW and DW CNTFET. For DW CNTFET near on-state region the inner tube acts as a second gate. This gate screens the effect of main gate on conduction band of outer tube. That is why tunneling current saturates which is absent in SW CNTFET. This current saturation corresponds to very low on-state transconductance and consequently low switching speed.

One important advantage of DW CNTFET over SW CNTFET is better inverse subthreshold slope with or without strain. But, the change of inverse sub-

threshold slope with strain is smaller in DW CNTFET. The capacitance-voltage characteristics, transconductance, intrinsic switching delay and intrinsic cut-off frequency all peak at gate voltage $V_{GS} \geq E_g/(2q)$ where, flat band condition exists between the source and channel under the gate region. This is reported before for SW CNTFET [65, 81, 82]. Due to application of strain with the increase of the band gap the peaks of the capacitance-voltage characteristics, transconductance, intrinsic switching delay and intrinsic cut-off frequency shift to higher gate voltage. Unlike SW CNTFET in DW CNTFET with the increase of compressive strain on-state transconductance decreases and with tensile strain it increases. The on-state transconductance also increases with torsional strain. The inner tube in DW CNTFET acts as a second gate. It reduces the modulation of conduction band with gate voltage near on-state region. The screening of main gate by inner tube is responsible for this behavior. A details physics is provided later in this chapter to explain the variation of on-state transconductance of DW CNTFET with strain. The intrinsic switching delay follows the variation of gate capacitance for both devices. The on-state intrinsic switching delay improves with compressive strain for both devices. But for this case also SW CNTFET exhibits better variation with strain. The on-state intrinsic cut-off frequency follows the variation of transconductance with strain. Unlike SW CNTFET, in DW CNTFET the on-state intrinsic cut-off frequency increases with tensile and torsional strain depending on the behavior of on-state transconductance with strain.

5.1 Device Structure

We simulate coaxially gated zero-Schottky-barrier SW and DW CNTFETs. A zero-Schottky-barrier metal-CNT contact for the valence band or p-channel CNTFET has been demonstrated experimentally using different metals, such as palladium (Pd) and rhodium (Rh) [24, 25]. Recently, zero-Schottky-barrier ballistic n-type CNTFET has been realized using scandium (Sc) [26]. The SW CNT is a (19, 0) zigzag tube with diameter of 1.5 nm and band gap of 0.5202 eV, and the DW CNT is generated from (10, 0) and (19, 0) zigzag tubes that has a band gap of 0.5163 eV. The device, shown in Figure 3.1, has a gate length L_g of 5 nm and the source and drain underlaps L_u of 22.5 nm each in strainless case. The gate oxide thickness t_{ox} is 2 nm, and the gate dielectric is SiO_2 with dielectric constant 3.9. The absolute physical thickness limit of SiO_2 is 0.7 nm [67]. Below this thickness, the Si reaches the interfacial regions from the channel and causes an effective "short" through the dielectric, rendering it useless as an insulator [67]. The chemical composition and electronic structure of gate oxides as thin as one nanometer have been measured using electron-energy-loss spectroscopy [83]. The spatial extent of the interfacial states that result from the spillover of the silicon conduction-band wavefunctions into the oxide places a fundamental limit of 0.7 nm (four silicon atoms across) on the thinnest usable silicon dioxide gate dielectric, and for present-day oxide growth techniques, interface roughness raises this limit to 1.2 nm [83]. Poisson solver uses an extended dielectric thickness t_{ox-ex} of 6 nm. Source and drain metal extensions L_{ex} of 15 nm are included in Poisson solver to take care of fringing electric fields [63–66]. The gate metal has the same work function as the CNT has. The work function of CNT is 4.5 eV [68]. The source and drain metal Fermi levels align with the conduction band of the CNT. Ballistic transport is assumed. Ballistic transport in

short CNTs (~ 60 nm) has been confirmed experimentally by measuring conductance at different temperatures [84].

5.2 Simulation Model

We perform a self-consistent solution between Poisson's equation and Schrodinger's equation. Our device is a coaxially gated CNTFET (see Figure 3.1) so that the potential V is independent of circumferential direction ϕ. We obtain electrostatic potential by solving two-dimensional Poisson's equation in cylindrical coordinates. The Poisson's equation, Eq. (3.2), is discretized using finite difference and solved by standard Newton-Raphon method. We have attached a detail explanation about the development of Poisson's solver in chapter 3. The potential is fixed to $V_{GS} - \Phi_G/q$ at the gate electrode, to $-\Phi_S/q$ at the source electrode, and to $V_{DS} - \Phi_D/q$ at the drain electrode. Here V_{GS} and V_{DS} are the gate to source and drain to source voltages, and Φ_G, Φ_S, and Φ_D are the work functions of gate, source, and drain metallizations. Von Neumann boundary conditions are used along the exposed surface of the dielectric. There, the radial component of the electric field is set to zero [63–65].

For charge density calculation, we use nearest-neighbor π-bond model to create Hamiltonian and recursive Green function (RGF) algorithm to solve Schrodinger's equation [58, 63]. A detail procedure of calculating Hamiltonian matrix elements incorporating strain is provided in chapter 4. We can incorporate strain in our tubes through the method in chapter 2. The recursive Green function algorithm is used to solve non-equilibrium Green function (NEGF) equation to calculate charge density and current as described in chaper 3.

5.3 Numerical Results and Discussion

The band gap variations with uniaxial strain of SW CNTs are shown in Figure 4.5(a). The band gap variation of DW CNT for different combination, like strain applied on outer tube only and inner tube left unstrained or vice versa or strain applied to both tubes are demonstrated in Figure 4.5(b). The band gap variations with torsional strain of both SW and DW CNTs are shown in Figures 4.6. The DW CNT follows the minimum of two band gaps of the tubes, it is constituted with.

The log I_D versus V_{GS} characteristics for both devices with uniaxial strain are introduced in Figures 5.1 and with torsional strain in Figures 5.2. In unstrained case the shape of the log I_D versus V_{GS} characteristics agrees with the previous results [63–65]. For both devices the log I_D versus V_{GS} curve has shifted upward for compressive strain indicating higher current with reduced band gap than unstrained case and for tensile strain it has shifted downward indicating lower current with increased band gap. With the application of the torsional strain the conductivity decreases. So the I-V curve shift downward with the torsional strain for both devices. The log I_D versus V_{GS} characteristics of SW (19, 0) (mod(n-m,3) = 1) with strain exhibits same type of behavior as previous literature [49].

The two components of the drain current for SW and DW CNT devices are shown in Figures 5.3 with unstrained tube and in Figures 5.4 with strained tube. The increase of thermal current of DW CNTFET in subthreshold region is more rapid than SW CNTFET. Near the Fermi level the density of states (DOS) of SW

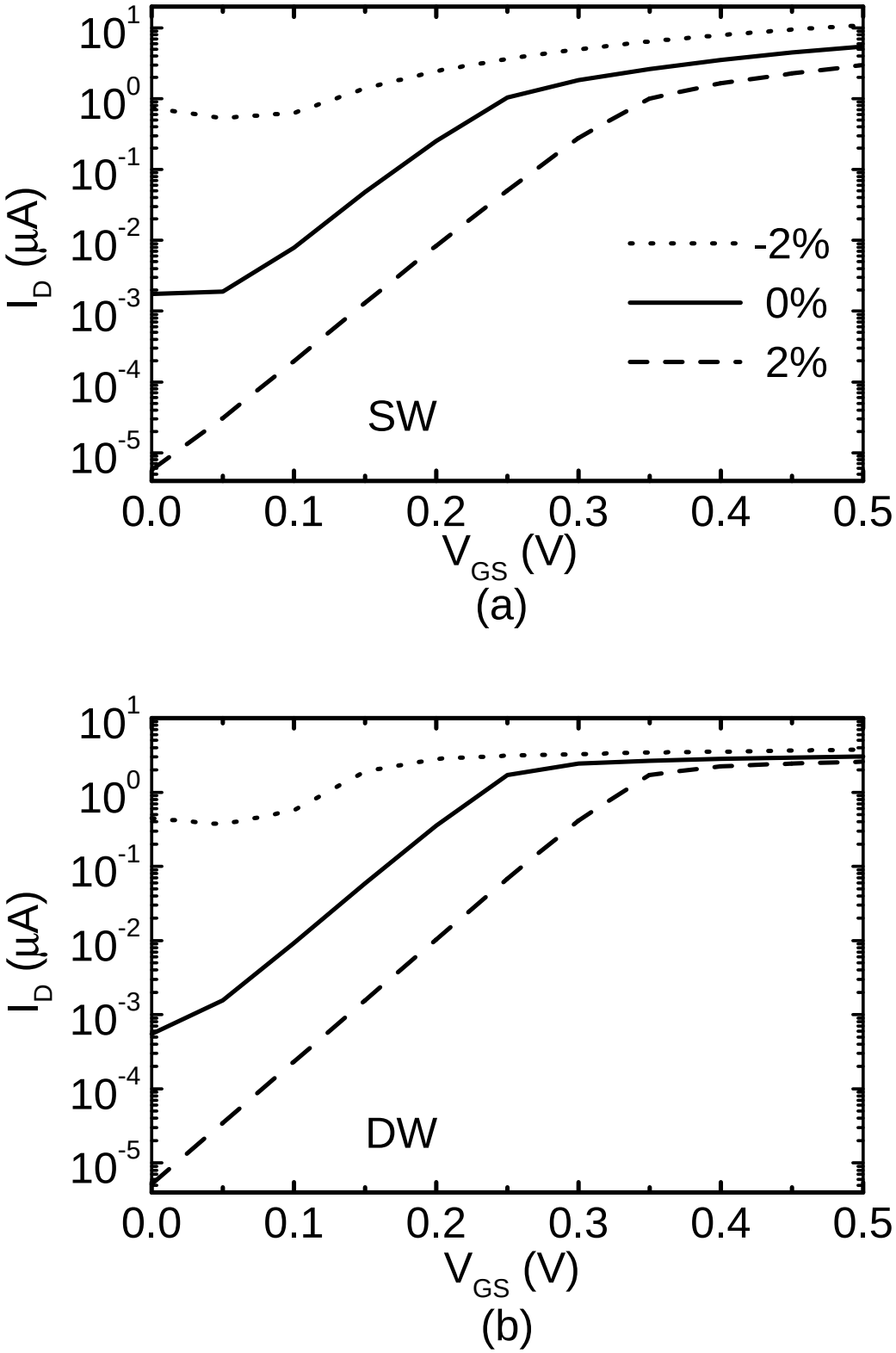

Figures 5.1: Simulated log I_D versus V_{GS} characteristics of (a) SW and (b) DW CNTFETs with uniaxial strain. Here, $V_{DS} = 0.5$V.

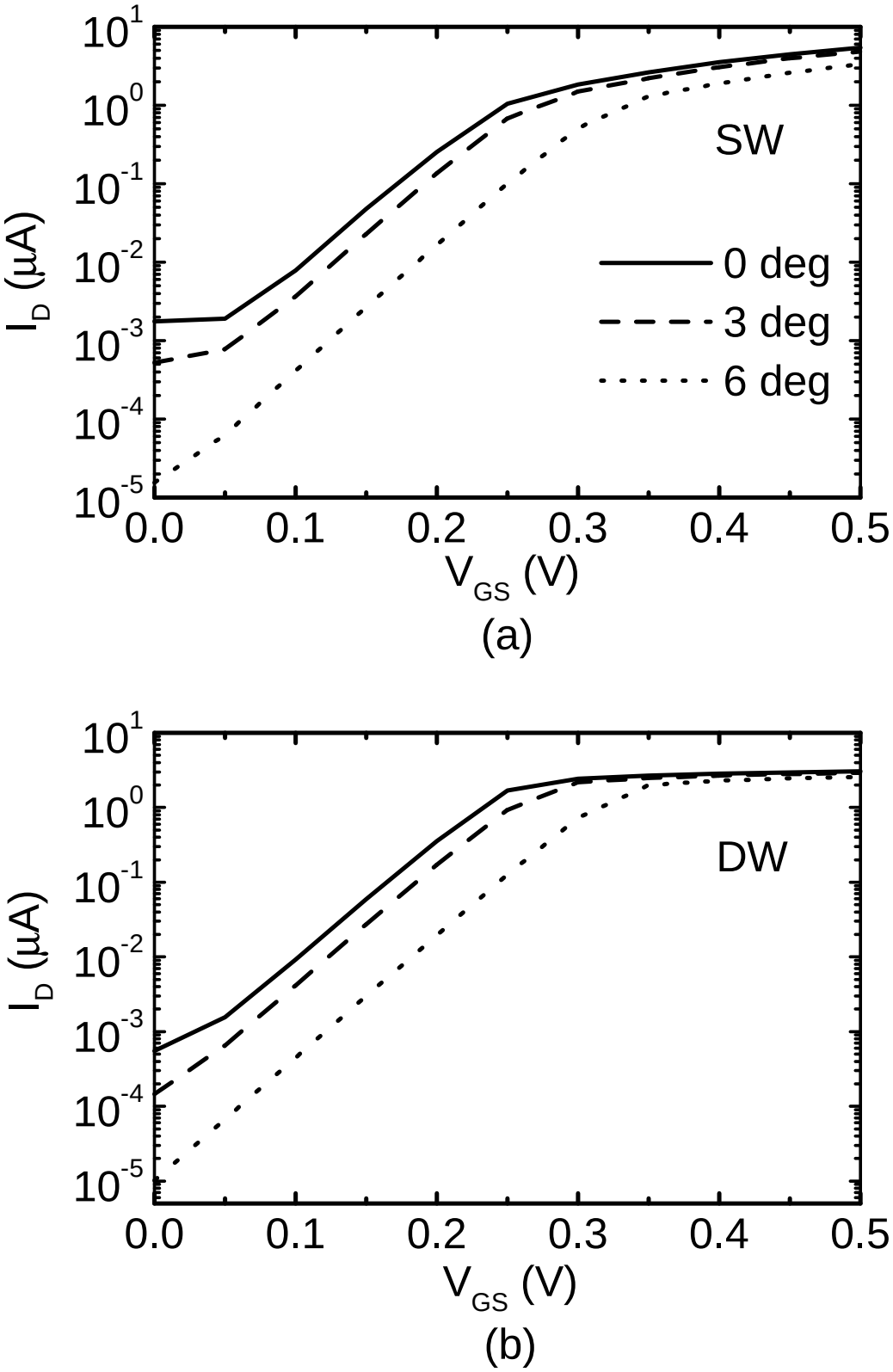

Figures 5.2: Simulated log I_D versus V_{GS} characteristics of (a) SW and (b) DW CNTFETs with torsional strain. Here, $V_{DS} = 0.5$V.

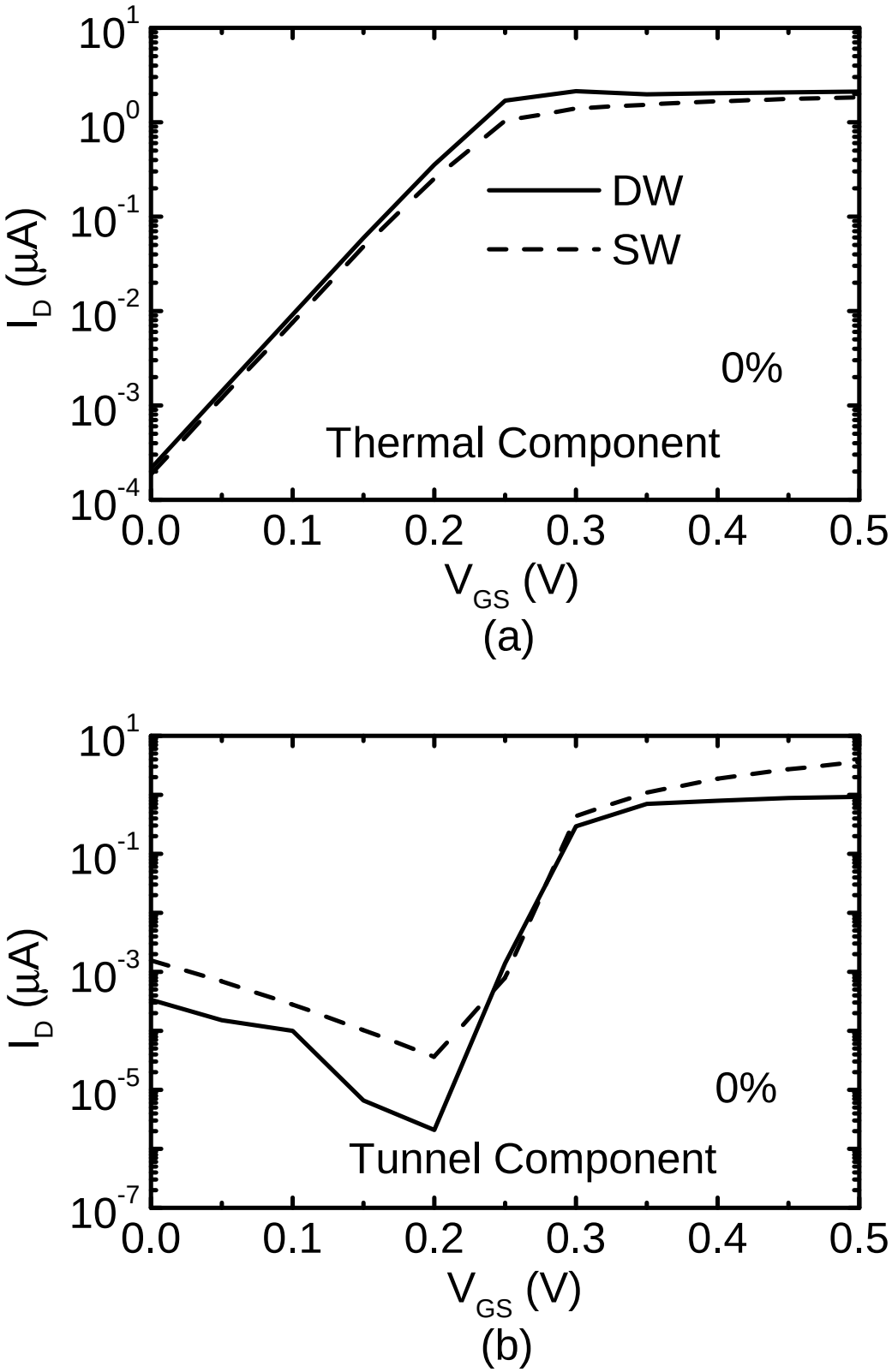

Figures 5.3: (a) Thermal component and (b) Tunnel component of the total current versus gate bias in for devices with SW and DW unstrained tube. Here, V_{DS} = 0.5V.

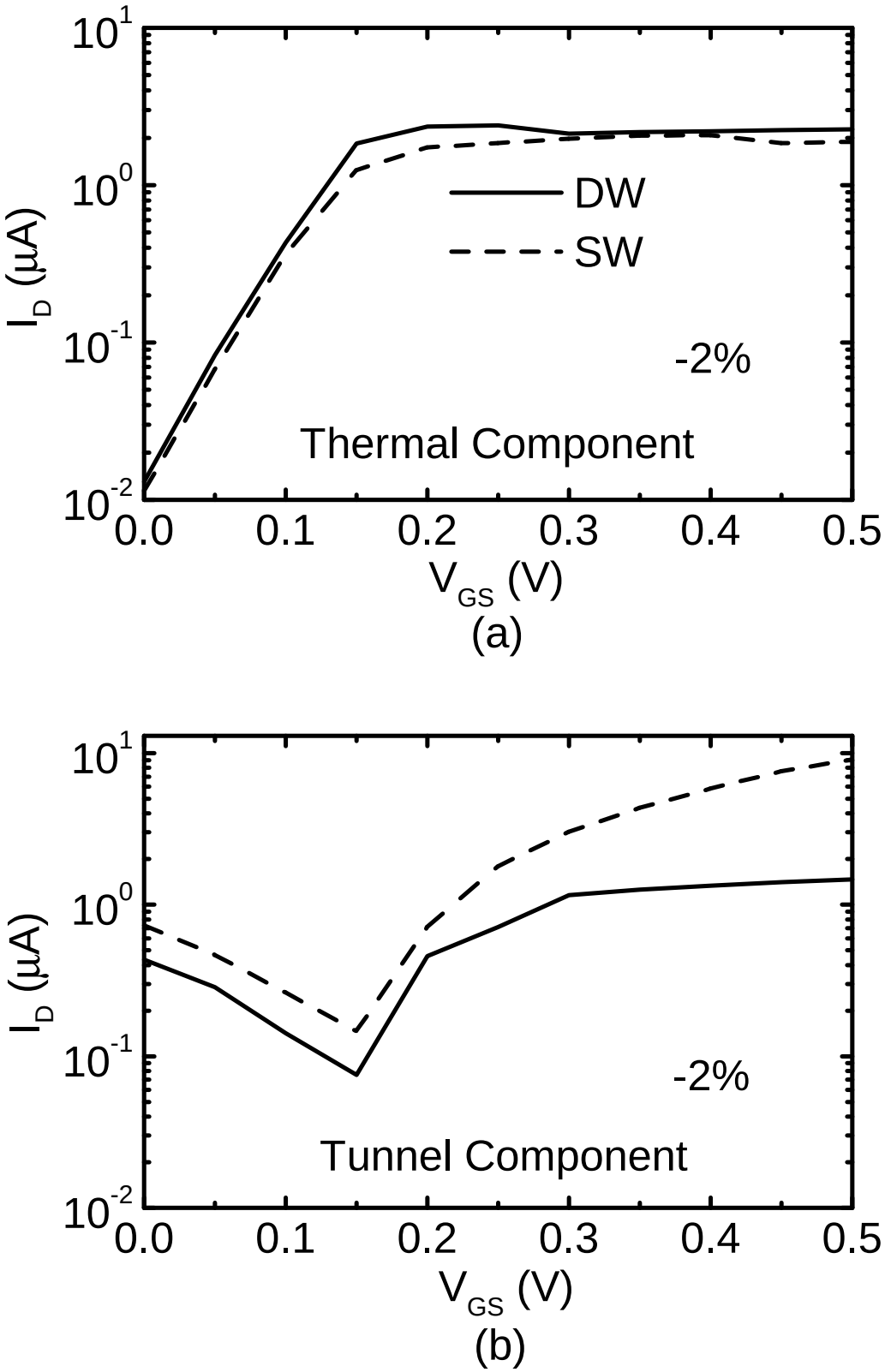

Figures 5.4: (a) Thermal component and (b) Tunnel component of the total current versus gate bias for devices with 2% compressed SW and DW tubes. Here, V_{DS} = 0.5V.

(19,0) and DW [(19, 0) (10, 0)] CNTs are almost equal (the band gap of inner tube (10, 0) is very high, so the states are available at energies far from the Fermi level). But the more far from the Fermi level the more are the density of states in DW [(19, 0) (10, 0)] CNT than SW (19,0) CNT for contribution of states of inner tube at high energy level (Figures 4.2, 4.3 and 4.4). These states from inner tube contribute in thermal current of DW CNTFET with outer tube. Irrespective of strain and irrespective of number of coaxial tubes in devices the thermal current saturates at $V_{GS} \geq E_g/(2q)$ [63]. Unlike thermal component, in tunnel component we get the lowest current at gate voltage other than zero volt with or without strain. Like thermal component for DW CNTFET the tunnel component also saturates after $V_{GS} \sim E_g/(2q)$. The inner tube in DW CNTFET acts as a second gate near on-state region. The concentration of electron in inner tube is very high in this region. This high concentration of electron increases the hole concentration and reduces the electron concentration on outer tube due to capacitive effect. But the main gate with the increase of positive gate voltage increases the electron concentration and reduces the hole concentration on outer tube due to capacitive effect. So, the inner tube screens the the gate effect on the conduction band of outer tube. The modulation of conduction band with the increase of gate voltage reduces near on-state region. That is why the tunnel current is almost insensitive to gate voltage near on-state region. The saturation of tunneling current near on-state region is missing in SW CNTFET with or without strain. But after $V_{GS} \geq E_g/(2q)$ this current increases slowly [63]. A detail explanation about the thermal component and tunnel component of I-V characteristics is provided with the help of band diagram in Figures 5.5 and current density in Figures 5.6.

To understand the off-state and on-state I-V characteristics of DW CNTFETs with different uniaxial strain, we plot, in Figures 5.5, the conduction band profiles, and in Figures 5.6, the energy spectrum of current, in off- and on-states of them. The conduction band profiles and the energy spectrums of current are reported before for SW CNTFET [63–66]. The band profiles of these devices is the energy versus position plots at the surface of outer tube. The conduction band is started with 0 eV from source side and ended with -0.5 eV near drain side depending on the bias voltages [63]. Under the gate region in off-state the energy of the conduction band is $E_g/2$ depending on work functions of different materials of the devices [63].

With the application of tensile strain the conductivity decreases and since it is a zero-Schottky-barrier device the whole conduction band shifts upward. We get opposite effect with the compressive strain. We get this variation in both off- and on-states. We get thermal current in the energy range $E_g/2 < E < \infty$ eV in off-state condition. We get thermal current in off-state in the energy ranges $0.13 < E < \infty$ eV, $0.26 < E < \infty$ eV, and $0.34 < E < \infty$ eV, respectively, for 2% compressive strained, unstrained, and 2% tensile strained CNTFETs. So with the increase of compressive strain thermal current increases and opposite effect occurs for tensile strain. The lower the top of the conduction band the higher the thermal current. The smaller the band gap the higher the possibility of having tunneling current near the band gap region. It is clearly visible in Figures 5.6. We get electron tunneling current for 2 % tensile strain in the region $0.15 < E < 0.34$ eV, for 0 % in the region $0 < E < 0.26$ eV, and for 2 % compressive strain in the region $-0.15 < E < 0.13$ eV. Near the band gap region both the electron and hole tunneling currents simultaneously exist. For the rest lower energy region we get solely hole tunneling current for all the

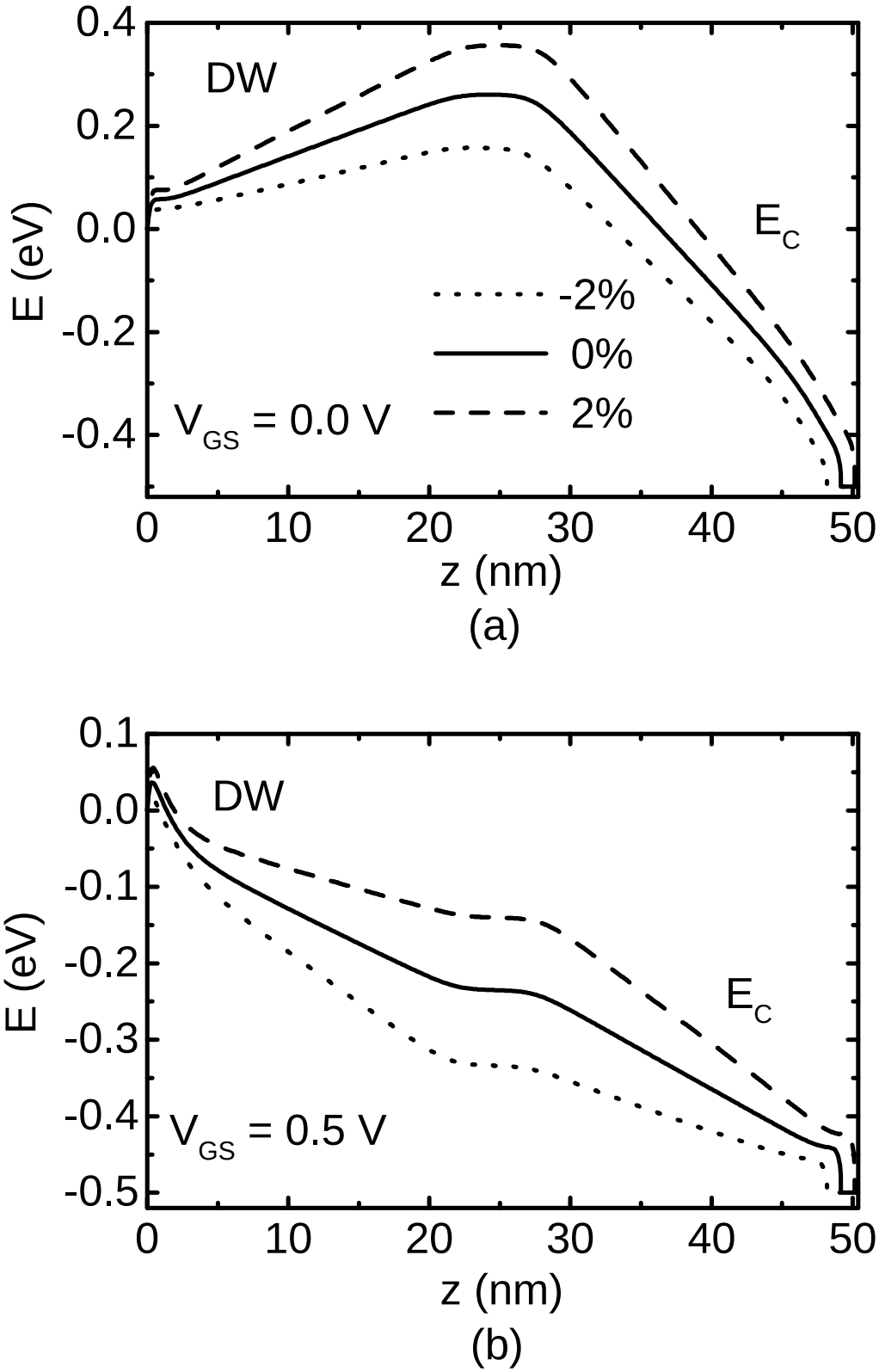

Figures 5.5: Conduction band profiles at three different values of uniaxial strain (a) off-state and (b) on-state for DW CNT devices. Here, $V_{DS} = 0.5$ V.

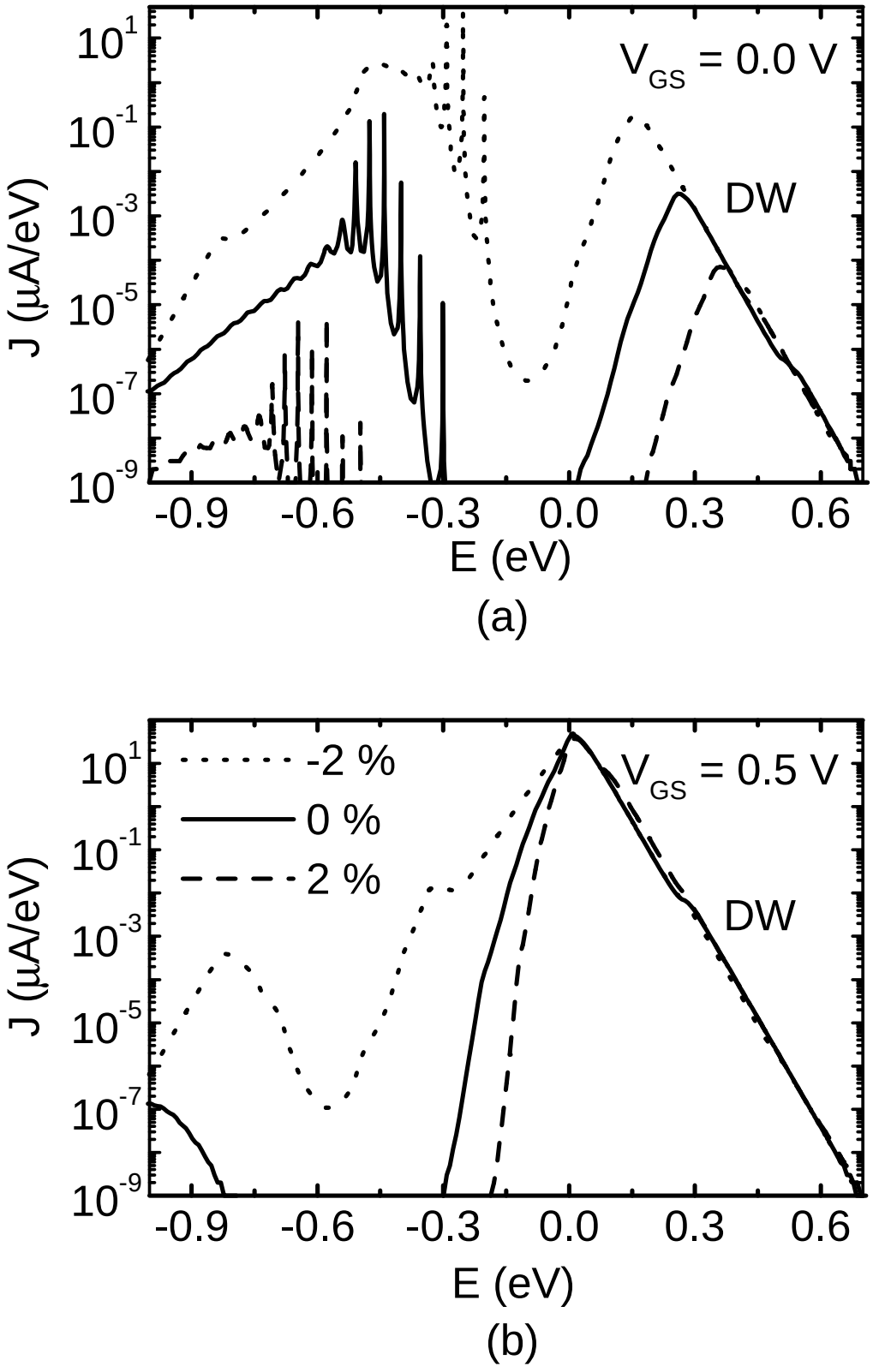

Figures 5.6: J vs E plot at three different values of uniaxial strain (a) off-state and (b) on-state for DW CNT devices. Here, $V_{DS} = 0.5$ V.

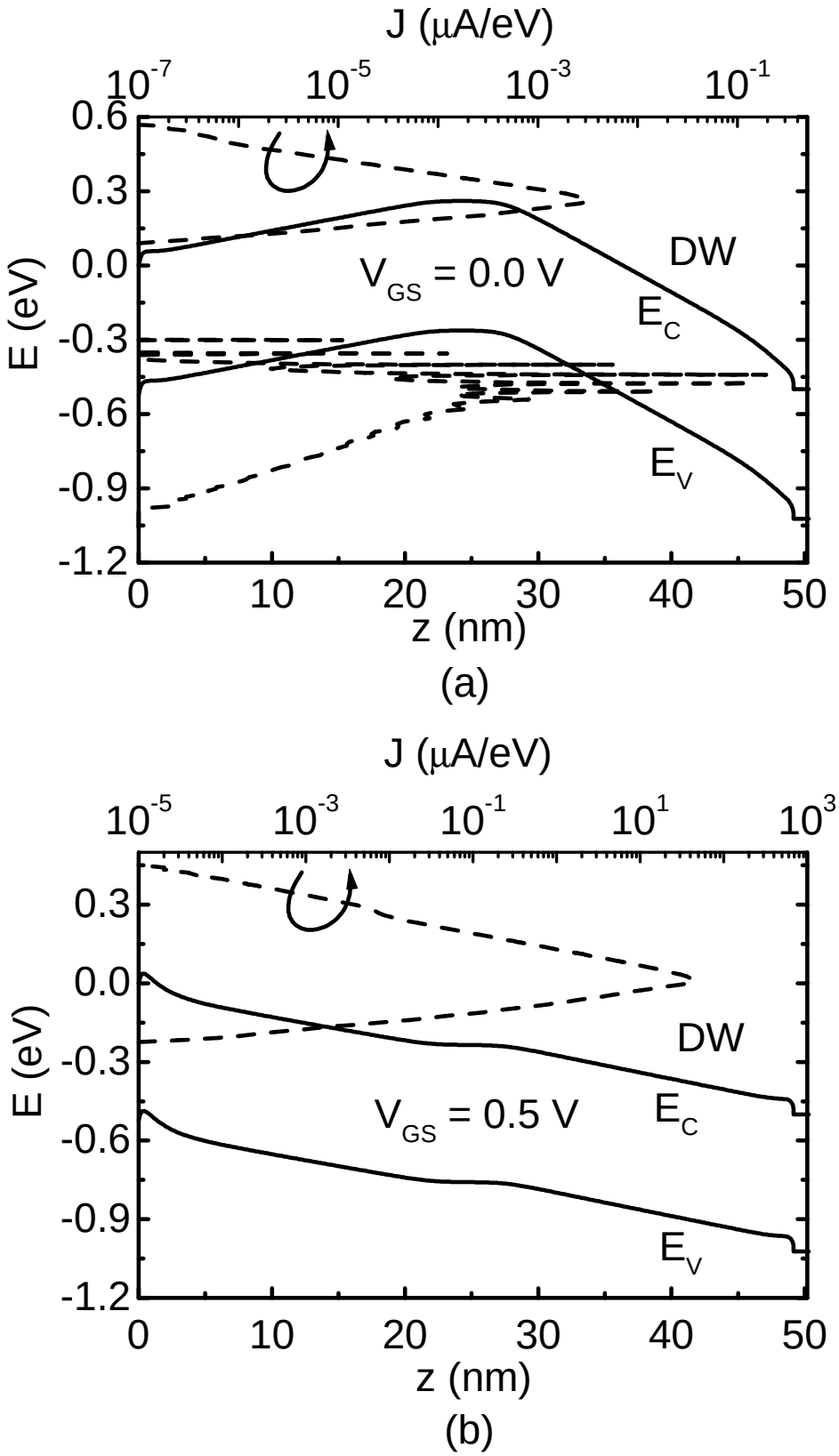

Figures 5.7: Current density versus energy superimposed on the band diagram in both (a) off-state and (b) on-state for DW CNTFET with unstrained tube. The drain bias is fixed to $V_{DS} = 0.5$ V.

DW CNTFET devices in this study. In the hole tunneling region we also get higher current for 2 % compressive strained CNTFET. Thermal current, electron tunneling current, and hole tunneling current of compressed CNT device dominate over others that is why we get higher current in off-state for compressed CNTFET. In on-state we get thermal current for all the strained or unstrained devices in our study in the energy range $0 < E < \infty$ eV. After gate bias above the half band gap potential, the thermal current does not change due to potential barrier saturation at ≈ 0 eV for all the devices. Here, we get the peak of all the conduction bands at source-channel interface at ≈ 0 eV. We get on-state electron tunneling current for 2 % tensile strain in the region $-0.17 < E < 0$ eV, for 0 % in the region $-0.3 < E < 0$ eV, and for 2 % compressive strain in the region $-0.65 < E < 0$ eV. For the rest lower energy region we get hole tunneling current. In on-state although the thermal currents same in all the devices, the 2 % compressed device has the both higher electron and hole tunneling currents. That is why again we get higher current for 2 % compressed device. But now in on-state. The physics behind the current variation with strain is the modulation of band gap (Figures 4.5 and 4.6) with strain. The current reduces with the type of strain that increases the band gap. The potential barrier height and length increase with larger band gap as shown in Figures 5.5. The increased height and length of the barrier reduces the current.

We plot current density versus energy superimposed on the band diagram in strainless case in Figures 5.7, to get clear cut idea about different components of the drain current. In off-state in Figure 5.7 (a) in the energy range $0.26 < E < \infty$ eV we get thermal current, in the energy range $0 < E < 0.26$ eV we get electron tunneling current, and in the energy range $-1.0 < E < -0.3$ eV we get hole tunneling current. In on-state in Figure 5.7 (b) in the energy range $0 < E < \infty$ eV we get thermal current, in the energy range $-0.26 < E < 0$ eV we get electron tunneling current. The hole tunneling current is negligible in on-state.

The off-state current, on-state current, and on/off current ratio versus uniaxial strain curves and torsional strain curves are shown in Figures 5.8 and 5.9, respectively. The shape of the off-current versus strain and on-state current versus strain curves follow the shape of previous report [49]. With 2 % compressive strain the off-state current becomes 423 time and 813 time of corresponding unstrained off-state current for SW CNTFET and DW CNTFET, respectively. The off-state current becomes 3.27×10^{-3} time and 7.58×10^{-3} time of corresponding unstrained off-state current for SW CNTFET and DW CNTFET, respectively, at 2 % tensile strain. With 2 % compressive strain the on-state current becomes 2 time and 1.23 time of corresponding unstrained on-state current for SW CNTFET and DW CNTFET, respectively. The on-state current becomes 1/1.82 time and 1/1.18 time of corresponding unstrained on-state current for SW CNTFET and DW CNTFET, respectively, at 2 % tensile strain. The on/off current ratio of SW CNTFET is 1/210 time of the untrained value and of DW CNTFET is 1/661 time of the unstrained value at 2 % compressive strain. At 2 % tensile strain the on/off current ratio of SW CNTFET is 168 time of the untrained value and of DW CNTFET is 112 time of the unstrained value. With 6^o torsional strain for SW and DW CNTFETs the off-state current becomes 8.86×10^{-3} and 18.54×10^{-3} times, respectively, of their unstrained value, on-state current becomes 1/1.625 and 1/1.18 times, respectively, of their unstrained value, and on/off current ratio becomes 70 and 46 times of their unstrained value. The change of off-state current and on/off current ratio with strain

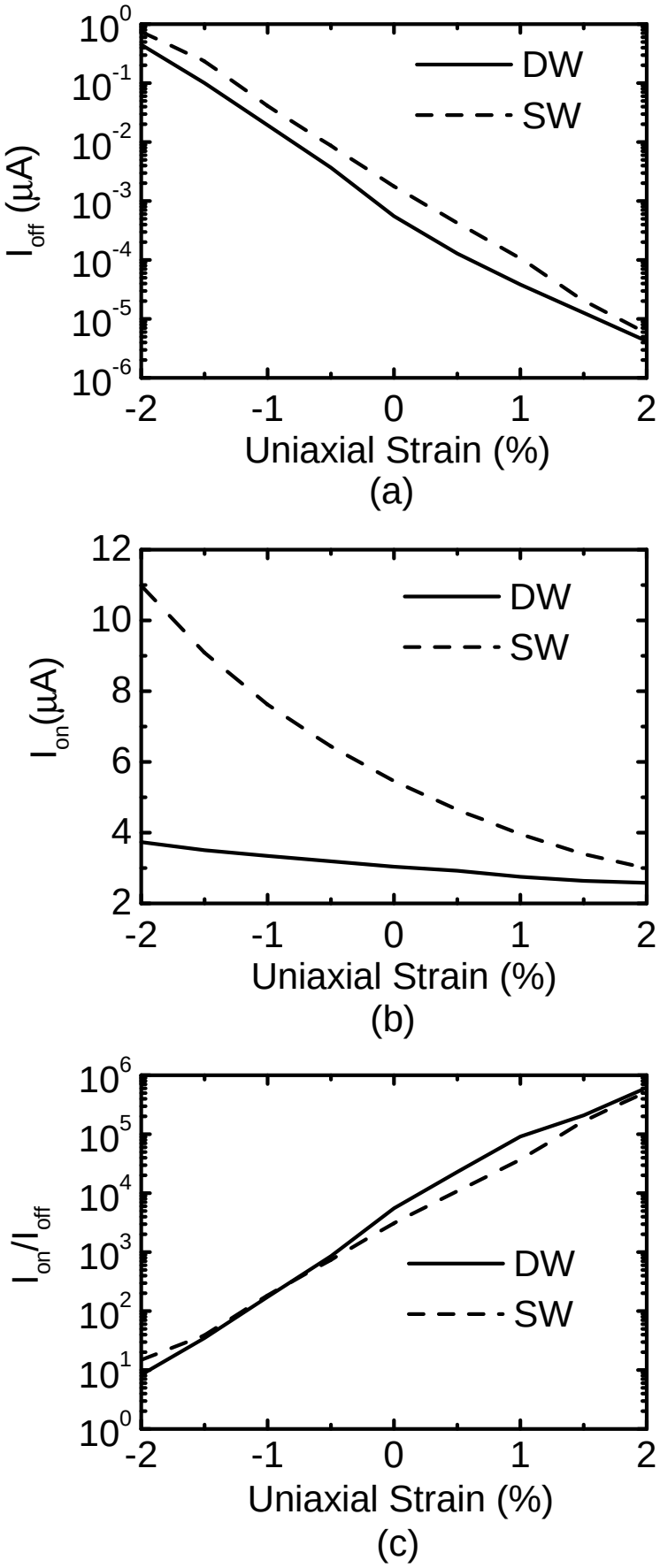

Figures 5.8: (a) The off-state current versus uniaxial strain, (b) the on-state current versus uniaxial strain and (c) on/off current ratio versus uniaxial strain curves for zero-Schottky-barrier SW and DW CNT devices.

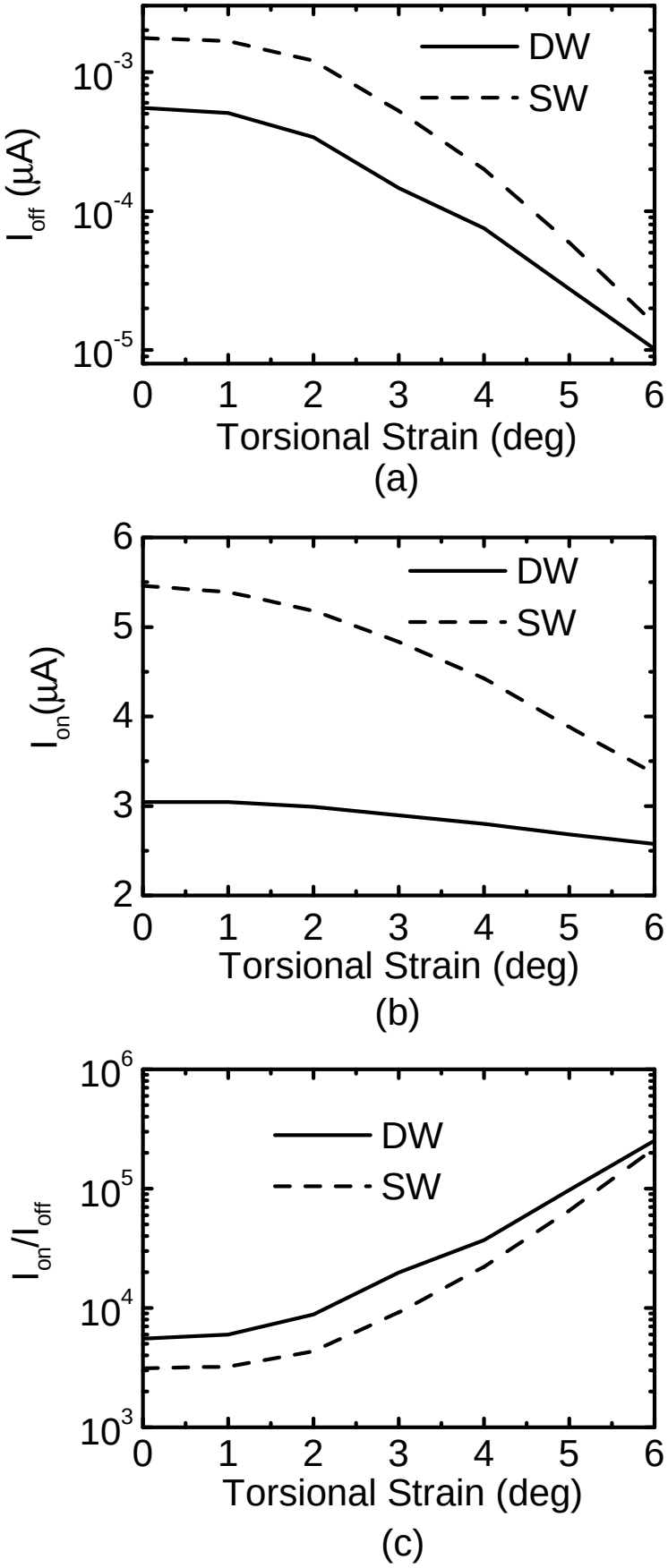

Figures 5.9: (a) The off-state current versus torsional strain, (b) the on-state current versus torsional strain and (c) on/off current ratio versus torsional strain curves for zero-Schottky-barrier SW and DW CNT devices.

is very high of both devices. On-state current variation with strain is small. This was reported for SW CNTFET in past [49].

The on-state transconductance versus uniaxial and torsional strain curves are shown in Figures 5.10 (a) and (b) respectively for both SW and DW CNTFETs. Transconductance is computed from $g_m = \partial I_D/\partial V_{GS}$. The on-state transconductance for SW and DW CNTFETs at 2 % compressive strain is 1.58 and 1/1.075 times, respectively, of their corresponding unstrained value, and at 2 % tensile strain is 1/1.37 and 1.48 times, respectively, of their corresponding unstrained value. The on-state transconductance is 1/1.31 time of the unstrained value for SW CNTFET and is 1.31 time of the unstrained value for DW CNTFET at 6^o torsional strain. Unlike SW the on-state transconductance of DW CNTFET increases with the increase of tensile strain and decreases with the increase of compressive strain. The inner tube of the DW CNTFET acts as a second gate. Near on-state its impact deepens. The more far from subthreshold region(deep on-state region) the more the effect of second gate. So the on-state transconductance decreases. The more the tensile strain the nearer the on-state to the onset of threshold region(Figures 5.1 and 5.2), the more the on-state transconductance. This type of behavior is also observable in DW CNTFET with torsional strain.

The variation of inverse subthreshold slope, defined as $S = (\partial log_{10} I_D/\partial V_{GS})^{-1}$, with uniaxial and torsional strain is shown in Figures 5.11(a) and (b), respectively. In Figures 5.11, DW CNTFET presents better inverse subthreshold slope than SW CNTFET in unstrained case which agrees qualitatively with experimental results [52]. In subthreshold region more rapid increase of thermal current in DW CNTFET is responsible for this better inverse subthreshold slope. With strain also DW CNTFET exhibits better inverse subthreshold slope. The inverse subthreshold slope of SW CNTFET is 3.07 time and 1/1.13 time of their unstrained value at 2 % compressive strain and at 2 % tensile strain, respectively. For DW CNTFET the inverse subthreshold slope is 2.48 time and 1/1.05 time of their unstrained value at 2 % compressive strain and at 2 % tensile strain, respectively. At 6^o torsional strain the inverse subthreshold slope is 1/1.13 time and 1/1.04 time of their corresponding unstrained value for SW CNTFET and DW CNTFET, respectively.

Finally we compare the performance metrics, namely the transconductance g_m, the intrinsic switching delay τ_S, and the intrinsic unity current gain frequency f_T. For this the gate capacitance is calculated from [64–66]

$$C_g = 2\pi R \int_0^{L_g} dz \frac{\delta D_r}{\delta V_g} + 2\pi \int_{t_{ox}}^{t_{ox-ex}} r dr \frac{\delta D_z}{\delta V_g}, \tag{5.1}$$

where, R is the radius of the dielectric covering t_{ox}. The first integral takes care of the fluxes emanating from the bottom surface of the gate metal and the second integral takes care of the fluxes emanating from the two sides of the gate metal facing to the source and drain. This gives the total gate capacitance $C_g = C_{gs} + C_{gd}$ which includes the effect fringing fields directly from the gate metal to the source and drain. The gate capacitance is the summation of gate-source capacitance, gate-drain capacitance and gate-channel capacitance. Among them the first two are the fixed capacitance for metal-metal capacitors. The last one depends on the density of states of carbon nanotube. That capacitance which depends on the density of states is known as quantum capacitance [69]. Since the density of states of carbon nanotube show up-down behavior with energy [33, 39, 41, 69], the capacitance also exhibits

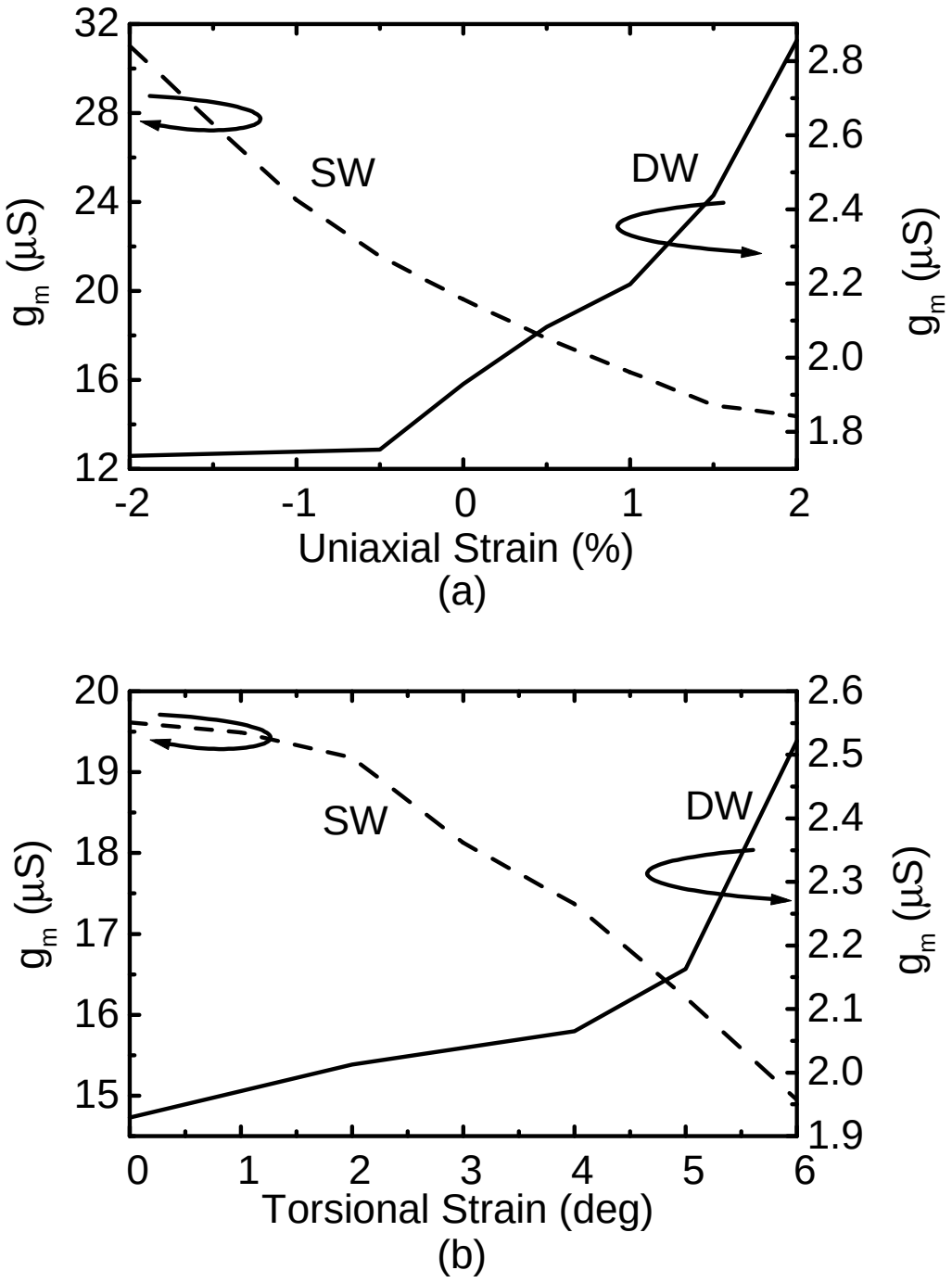

Figures 5.10: (a) The on-state transconductance versus uniaxial strain and (b) The on-state transconductance versus torsional strain curves for zero-Schottky-barrier SW and DW CNT devices.

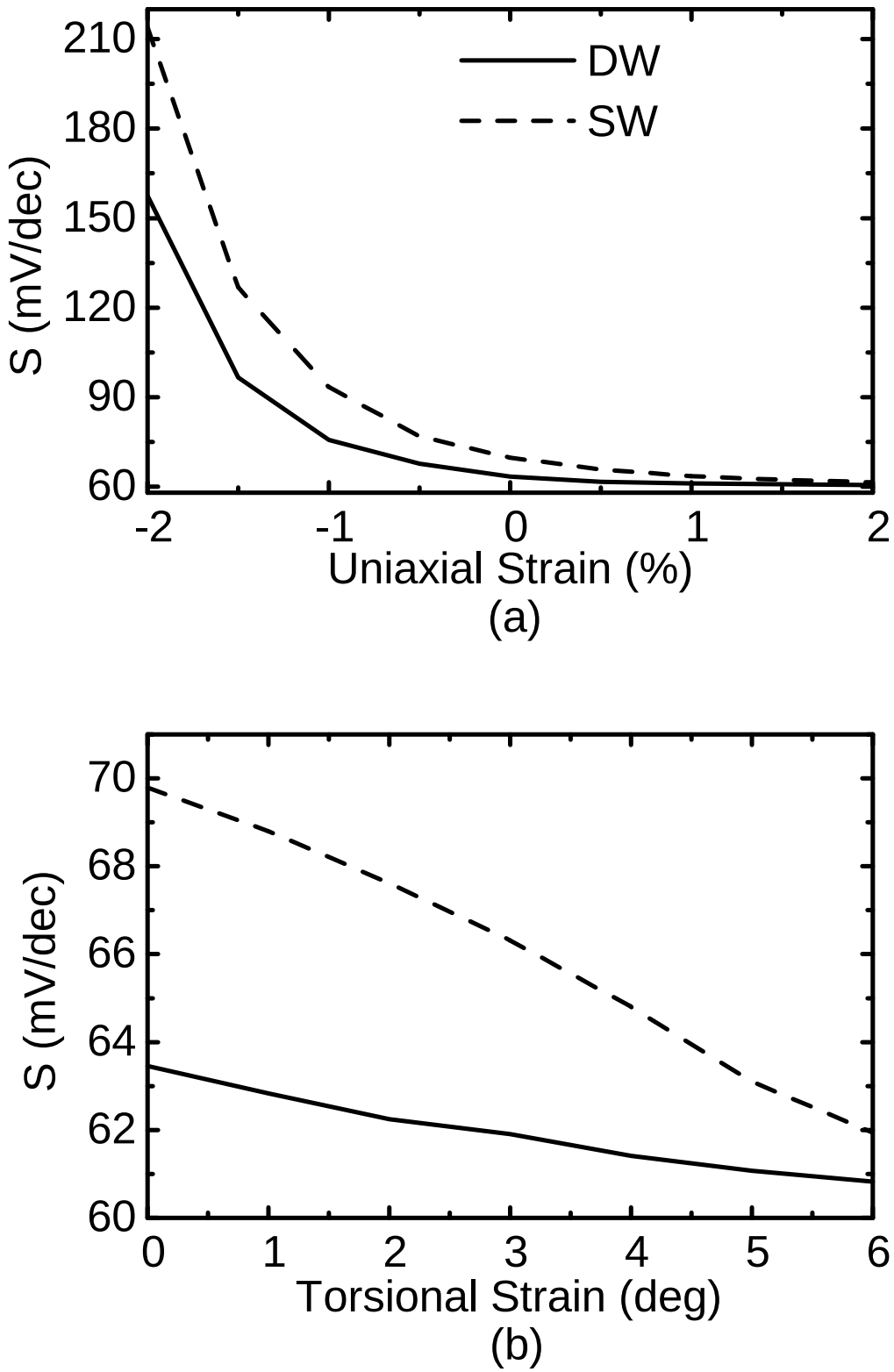

Figures 5.11: The inverse subthreshold slope versus (a) the uniaxial strain and (b) torsional strain curves of SW and DW CNT devices.

same behavior with gate voltage. This quantum capacitance is significantly small compare to other parts of gate capacitance [64, 65]. The intrinsic switching delay is calculated from $\tau_S = C_g V_{DD}/I_{ON}$ and the intrinsic unity current gain frequency from $f_T = g_m/2\pi C_g$, where, transconductance is computed from $g_m = \partial I_D/\partial V_{GS}$ [64–66]. V_{DD} is 0.5 V in our study.

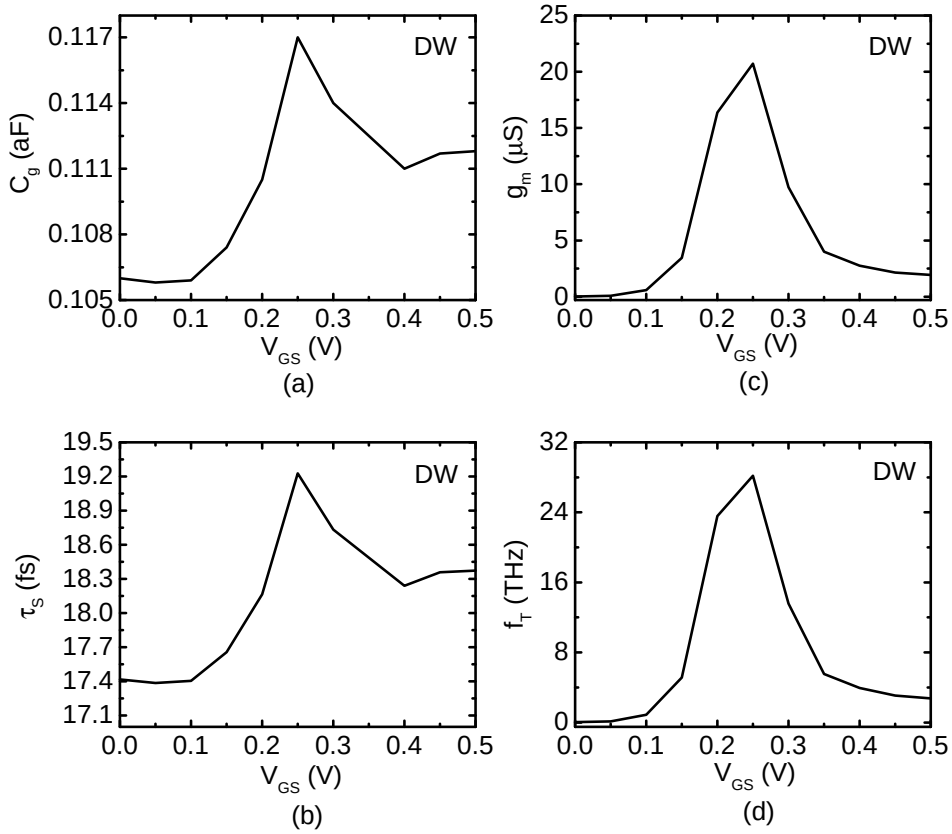

Figures 5.12: (a) The gate capacitance, (b) intrinsic switching delay, (c) transconductance and (d) intrinsic cut-off frequency versus gate voltage curves of zero-Schottky-barrier DW CNT devices with unstrained tubes.

The gate capacitance, the transconductance, the intrinsic switching delay, and the intrinsic cut-off frequency versus gate bias plots of DW CNTFET only in unstrained case is shown in Figures 5.12. The gate capacitance and transconductance peak as usual at a gate bias $\approx E_g/2q$ where, there is approximately a flat band situation between the potential under the gate region and the source Fermi level. This is reported before for SW CNTFET [65, 81, 82]. The intrinsic switching delay depends on gate capacitance. So, the shape of intrinsic switching delay is similar to gate capacitance [82]. Since the variation of gate capacitance is very small compare to transconductance. So, the intrinsic cut-off frequency follows the shape of transconductance [65, 81, 82]. The on-state value of g_m is much lower in DW CNTFET due to current saturation. Consequently we get low cut-off frequency in on-state.

For four different values of uniaxial strains we plot the transconductance versus gate voltage and gate capacitance versus gate voltage curves in Figures 5.13 (a) and (b) respectively. The variation of gate capacitance with gate voltage depends on the density of states [69]. The vaiation of density of states with strain is reported before [39]. With the increase of the band gap both the peaks of transconductance

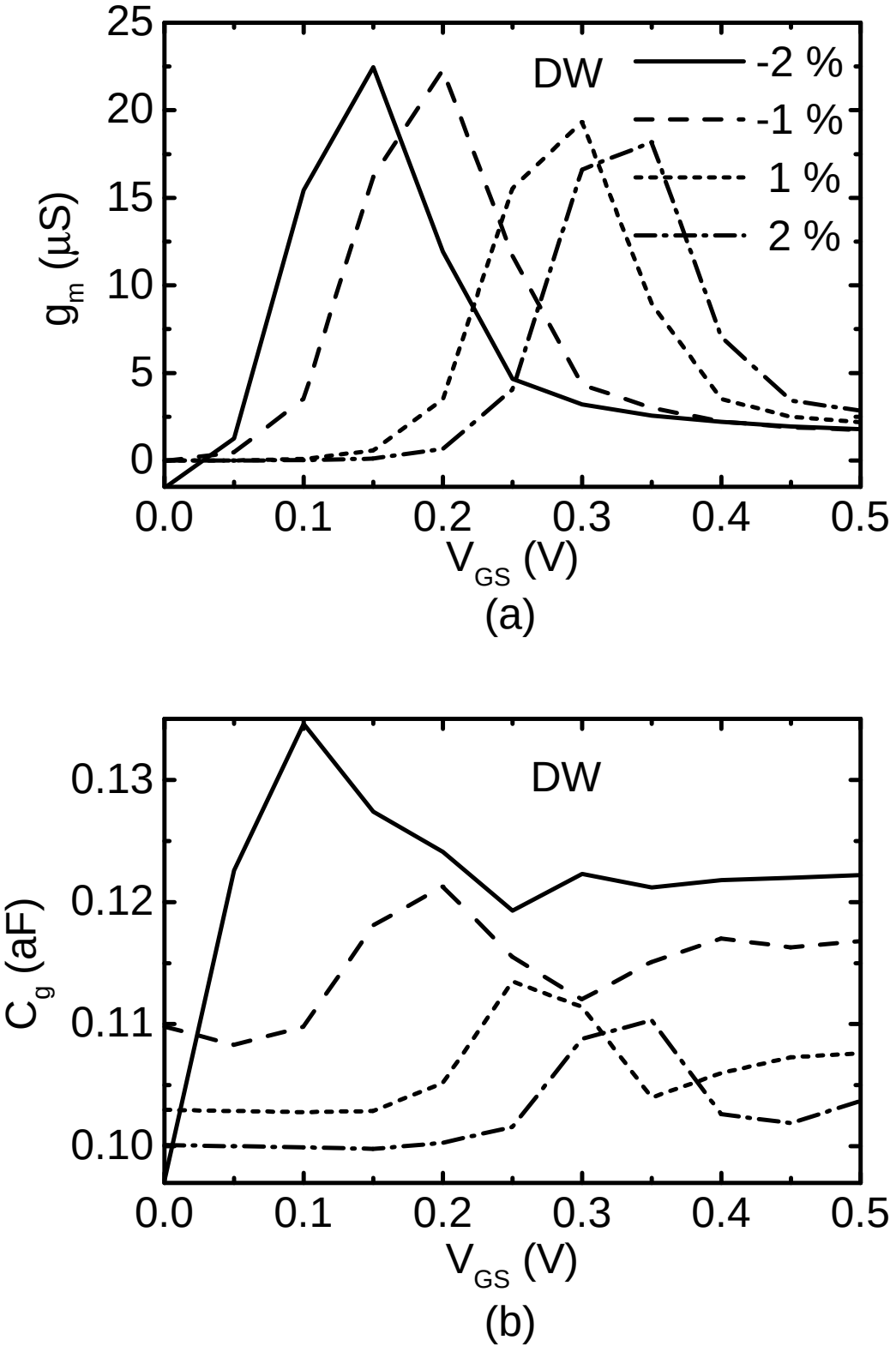

Figures 5.13: (a) Transconductance and (b) gate capacitance versus gate voltage curves at four different values of uniaxial strain of DW CNT devices.

versus gate voltage and gate capacitance versus gate voltage curves shift to higher gate voltage. Actually we get the peaks of these curves when the flat band condition exists between the source fermi level and conduction band under the gate region [65, 81, 82]. For higher band gap we need high gate voltage to achieve flat band. Due to application of uniaxial strain with the increase of the band gap the peaks of both the transconductance and the gate capacitance decreases. The on-state gate capacitance decreases as well. But the on-state transconductance increases.

The switching speed as well as the operating frequency of any device relies on intrinsic switching delay. The on-state intrinsic switching delay and intrinsic cut-off frequency for both devices are shown in Figures 5.14 (a) and (b), respectively, with different uniaxial strain. The on-state switching delays of SW CNTFET and DW CNTFET are 1.69 and 1.09 times, respectively, of their corresponding unstrained switching delay at 2 % tensile strain. At 2 % compressive strain the on-state switching delays of SW CNTFET and DW CNTFET become 1/1.87 and 1/1.12 times, respectively, of their corresponding unstrained switching delays. The variation of on-state switching delay of SW CNTFET with uniaxial strain is qualitatively similar with the previous reports [49]. The SW CNTFET shows shorter switching delay for 50 nm CNTFET device with or without strain. With the increase of tensile strain the on-state switching delay increases and with the increase of compressive strain it decreases for both SW and DW CNTFETs. We observe the opposite scenario for on-state intrinsic cut-off frequency versus strain curves. Unlike the SW CNTFET, for DW CNTFET the on-state intrinsic cut-off increases with the increase of tensile strain. Intrinsic cut-off frequency proportional to transconductance since the variation of gate capacitance compare to transconductance is very small. The on-state transconductance increases with the increase of tensile strain which is unlikely in SW CNTFET; consequently increase in on-state cut-off frequency. For compressive strain also we observe opposite behavior between SW and DW CNTFETs in terms of cut-off frequency. For SW CNTFET the on-state cut-off frequency at 2 % tensile strain is 1/1.26 time of the unstrained on-state cut-off frequency. At 2 % compressive strain this is 1.47 time of the unstrained value. For DW CNTFET with the application of 2 % tensile and 2 % compressive strains the on-state cut-off frequency becomes 1.59 time and 1/1.18 time, respectively, of unstrained value. With the application of the torsional strain (see Figures 5.15) the switching delay increases as usual for both devices. At 6^o torsional strain the on-state intrinsic switching delay becomes 1.59 time for SW CNTFET and 1.19 time for DW CNTFET of the corresponding unstrained values. The shape of the on-state switching delay versus torsional strain curves is almost similar to previous report [49].The on-state cut-off frequency for SW CNTFET is 1/1.28 time and for DW CNTFET is 1.29 time of the unstrained on-state cut-off frequency for 6^o torsional strain. Again unlike the SW CNTFET, for DW the intrinsic cut-off frequency increases with torsional strain.

In conclusion, with the application of strain I-V curves are shifted either upward or downward for both devices. The variation of off-state current and on/off current ratio are very high for both devices. The change of on-state current with strain is comparatively small. The SW CNTFET shows better variation of off-state current, on-state current and on/off current ratio with strain. With the application of tensile and torsional strains on-state transconductance increases and with torsional strain it decreases which is unlikely in SW CNTFET. Although the inverse subthreshold is better in DW CNTFET with or without strain, its variation with strain is smaller

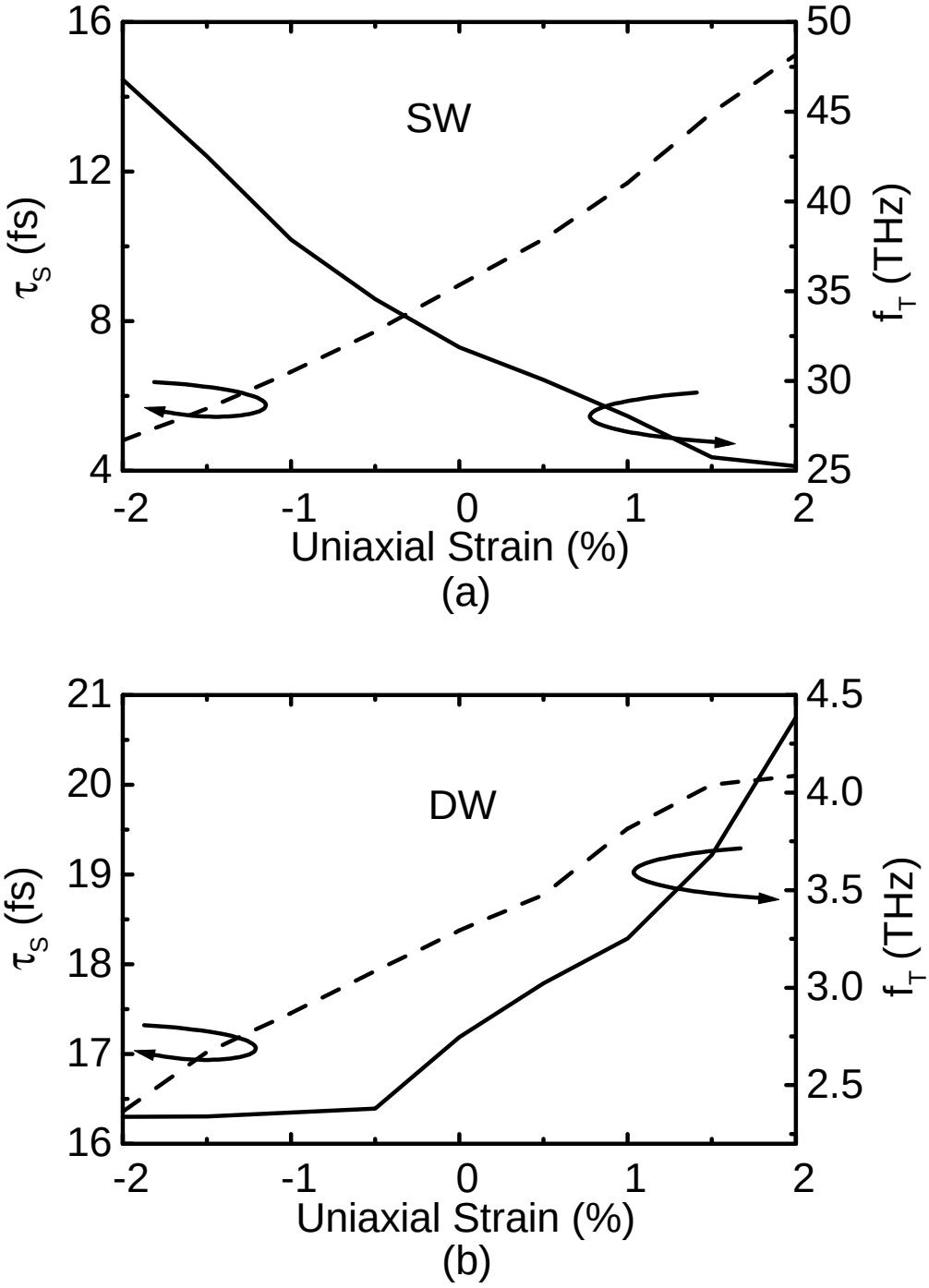

Figures 5.14: The on-state intrinsic switching delay and on-state intrinsic unity current gain frequency versus uniaxial strain for Schottky-barrier (a) SW CNTFET and (b) DW CNTFET.

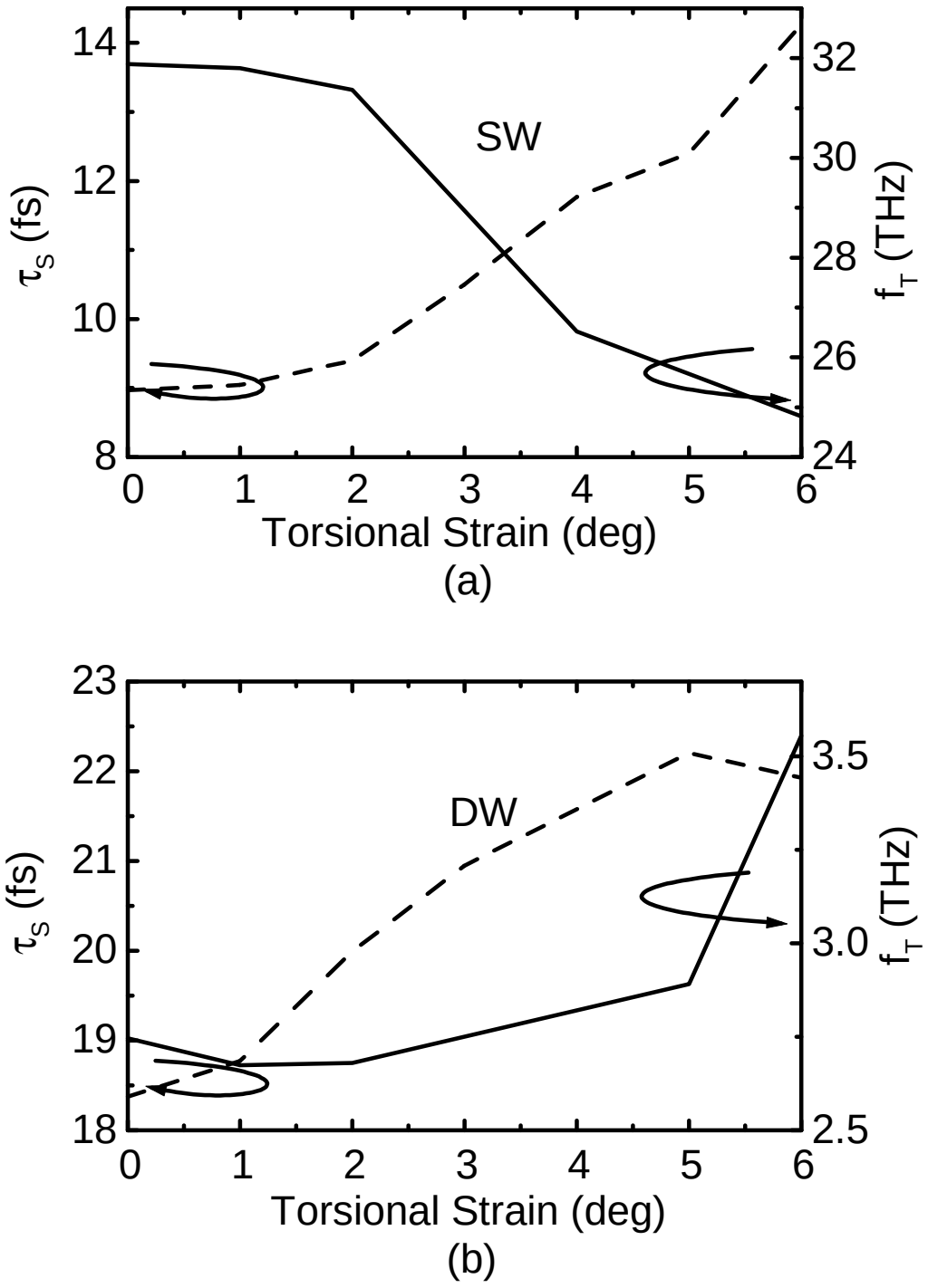

Figures 5.15: The on-state intrinsic switching delay and on-state intrinsic unity current gain frequency versus torsional strain for Schottky-barrier (a) SW CNTFET and (b) DW CNTFET.

compare to SW. Unlike SW CNTFET the on-state cut-off frequency increases with tensile or torsional strain following on-state transconductance. The variation of on-state intrinsic switching delay is smaller of DW CNTFET with strain.

Chapter 6

Scaling of Double-Walled Carbon Nanotube Field Effect Transistors

We have studied the current-voltage characteristics, capacitor-voltage characteristics and figures of merit for zero-Schottky-barrier CNTFETs with strain in previous chapter. To explain the current-voltage characteristics we have incorporated the help of band diagram and current density versus energy curve. For a 50 nm CNTFET with strain one important finding of DW over SW is better inverse subthreshold slope with or without strain. But the performance of DW CNTFET is very poor regarding switching speed. SW CNTFET has much better switching speed. Poor on-state current and transconductance are responsible for this. To extend our research we have also perform work by varying length of the different section of the devices and materials. With the increase of the channel length the I-V characteristics almost remain same. This was reported before for SW CNTFET [64]. But the gate capacitance of the devices drastically reduces which shortens the intrinsic switching delay and increases the intrinsic cut-off frequency. The gate capacitance of DW CNTFET is much sensitive to channel length over SW CNTFET. So the more the channel length, the more the switching speed of DW CNTFET over SW CNTFET. Unlike the channel length with the increase of the gate length the gate capacitance increases. But with the increase of both the gate length and channel length the gate capacitance reduces but much slower than that for increase of gate length only. With the increase of gate oxide thickness the gate capacitance increases. This has also been reported for SW CNTFET before [65]. As a result performance degrades. Later we use schottky-barrier height $E_g/4$ and $E_g/2$, and determine I-V characteristics. With the increase of barrier height the tunneling current significantly increases so that thermal current is negligible to it in both off- and on-states. Even there is no define off- and -on states for Schottky-barrier DW CNTFET with high barrier height. So it is useless as a switch. But for SW CNTFET although the on/off current ratio decreases, still it can be used as a switch [49].

6.1 Device Structure

The geometry consists of a coaxial channel, gate-oxide and gate with source and drain underlap as before (see Figure 3.1). Both the source and drain are metallic materials connected to the source and drain ends of the tube, respectively. First we have made simulation by assigning gate length $L_g = 5$ nm, $t_{ox} = 2$ nm, other things

as before and only varied the channel length. We have evaluated the performance of the device for channel length L = 50, 70 and 100 nm. We have measured the performance of the device again with L = 50 nm for different values of L_g such as 5, 15, 30 nm. Next the performance of the device by varying gate oxide thickness at three different values t_{ox} 2, 4 and 6 nm is estimated. We have also repeat the simulation of $L_g = 5$ nm, $t_{ox} = 2$ nm and L = 50 nm by varying only Schottky-barrier height.

6.2 Simulation Model

The simulation model uses a self-consistent solution between electrostatics and charge density. We use the same device structure as discussed in the previous chapter except the strainless channel. The electrostatic calculation solves the 2D Poisson's equation in cylindrical coordinates, which has been discussed in detail in the chapters 3 and 5. The charge density calculation solves the non equilibrium Green function equations using the recursive Green function algorithm with an atomic p_z orbital basis which is also discussed in chapter 3. Ballistic transport is assumed. Ballistic transport in short CNTs ($\sim$ 60 nm) has been confirmed experimentally by measuring the conductance at different temperatures [84].

6.3 Numerical Results and Discussion

We simulate coaxially gated Schottky-barrier SW DW CNTFETs as shown in Figure 3.1. The devices have a gate length L_g of 5 nm and source and drain extensions L_{uS} and L_{uD} depend on the channel length. The gate oxide is SiO_2 of dielectric constant 3.9 with thickness t_{ox} of 2.0 nm [67]. Poisson solver uses an extended dielectric thickness t_{ox-ex} (or gate metal thickness) of 6 nm and source and drain metal extensions L_{ex} of 15 nm so that the fringing electric fields are taken care of [63–66]. The gate metal has the same work function value as the CNT. The work function of the CNT is 4.5 eV [68]. The source and drain metal Fermi functions align with the conduction band of the CNT. We have performed this research with varying channel length to L = 50, 70 and 100 nm. We repeat this work now with variable gate length $L_g = 5$, 15 and 30 nm. Next we vary the gate oxide thickness to three different values $t_{ox} = 2$, 4, and 6 nm.

6.3.1 Effects of Channel Length

We have performed research with channel length L = 50, 70 and 100 nm in this section. The log I_D versus V_{GS} characteristics for both devices are introduced in Figures 6.1. For both devices the log I_D versus V_{GS} curve has shifted downward with the increase of channel length [64]. In upper portion of the subthreshold region the I-V characteristics are almost same irrespective of channel length for both SW and DW CNTFETs. There is only small variation in off-state and on-state region. However, current variation near on-state region for SW CNTFET is much higher over DW CNTFET.

To understand the I-V characteristics of DW CNTFETs with different channel lengths, we plot, in Figures 6.2, the conduction band profiles, and in Figures 6.3, the

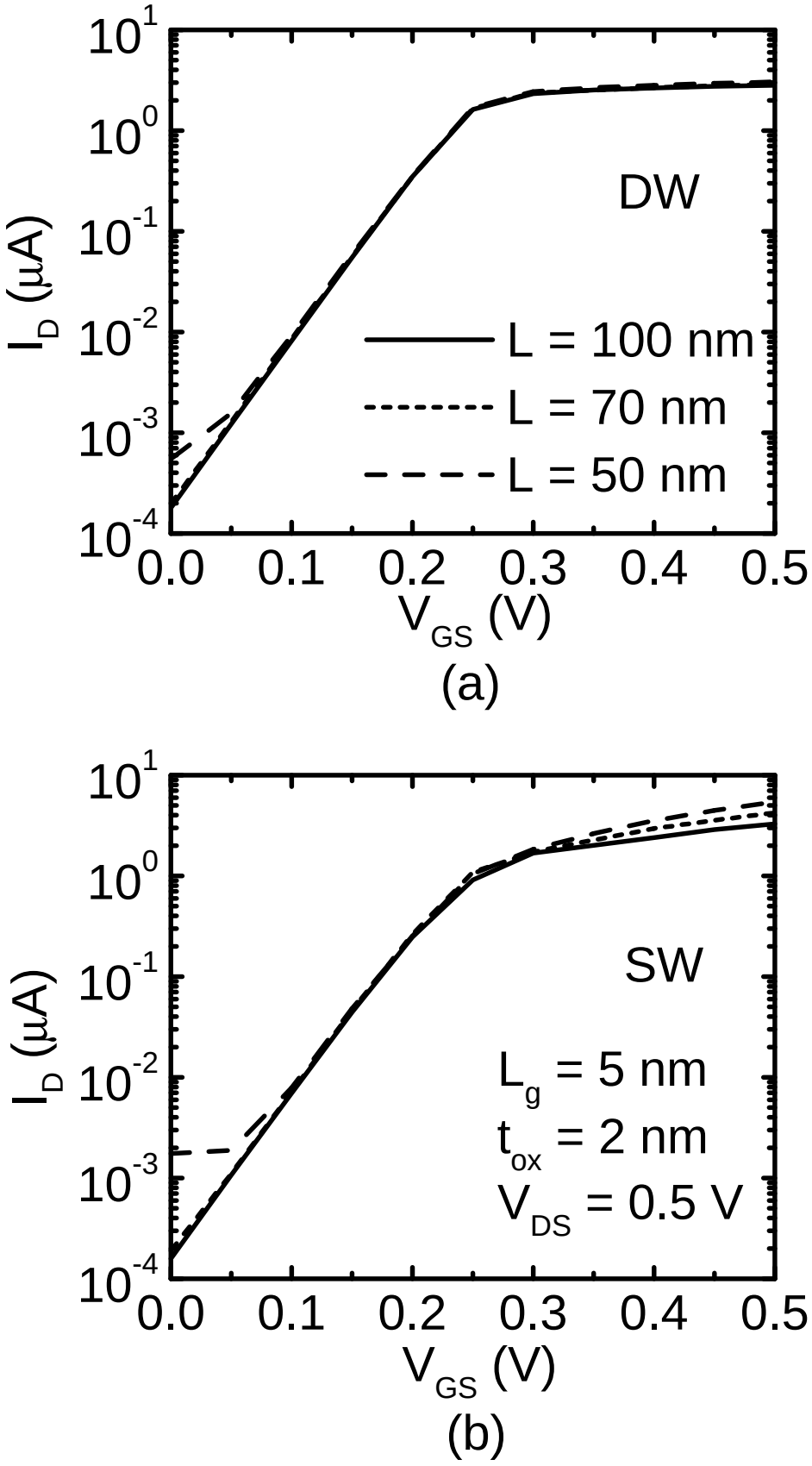

Figures 6.1: Simulated log I_D versus V_{GS} characteristics of (a) SW and (b) DW CNTFETs. Here, $V_{DS} = 0.5$V.

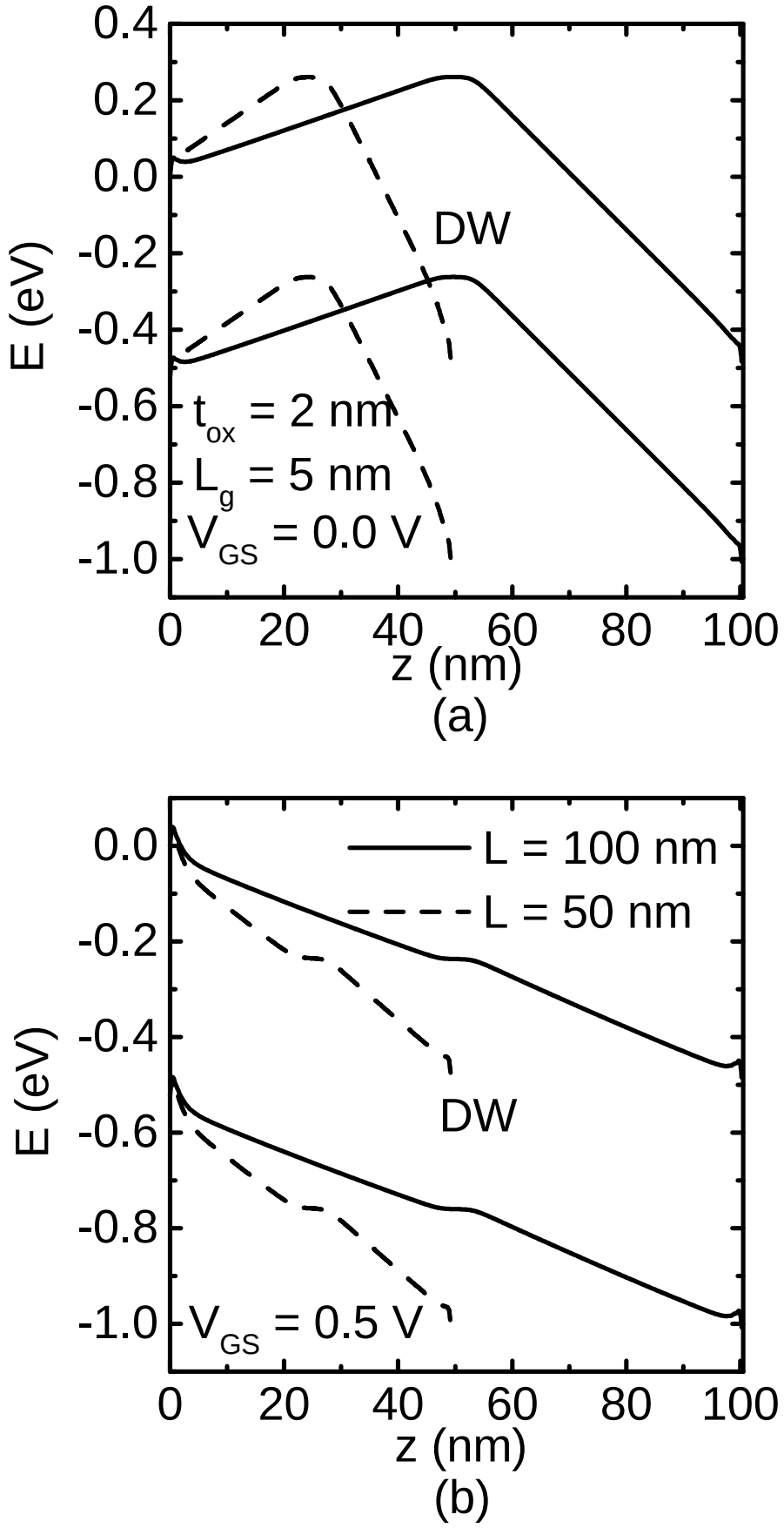

Figures 6.2: Conduction and valence band profiles at two different values of channel length (a) off-state and (b) on-state. Here, $V_{DS} = 0.5$V.

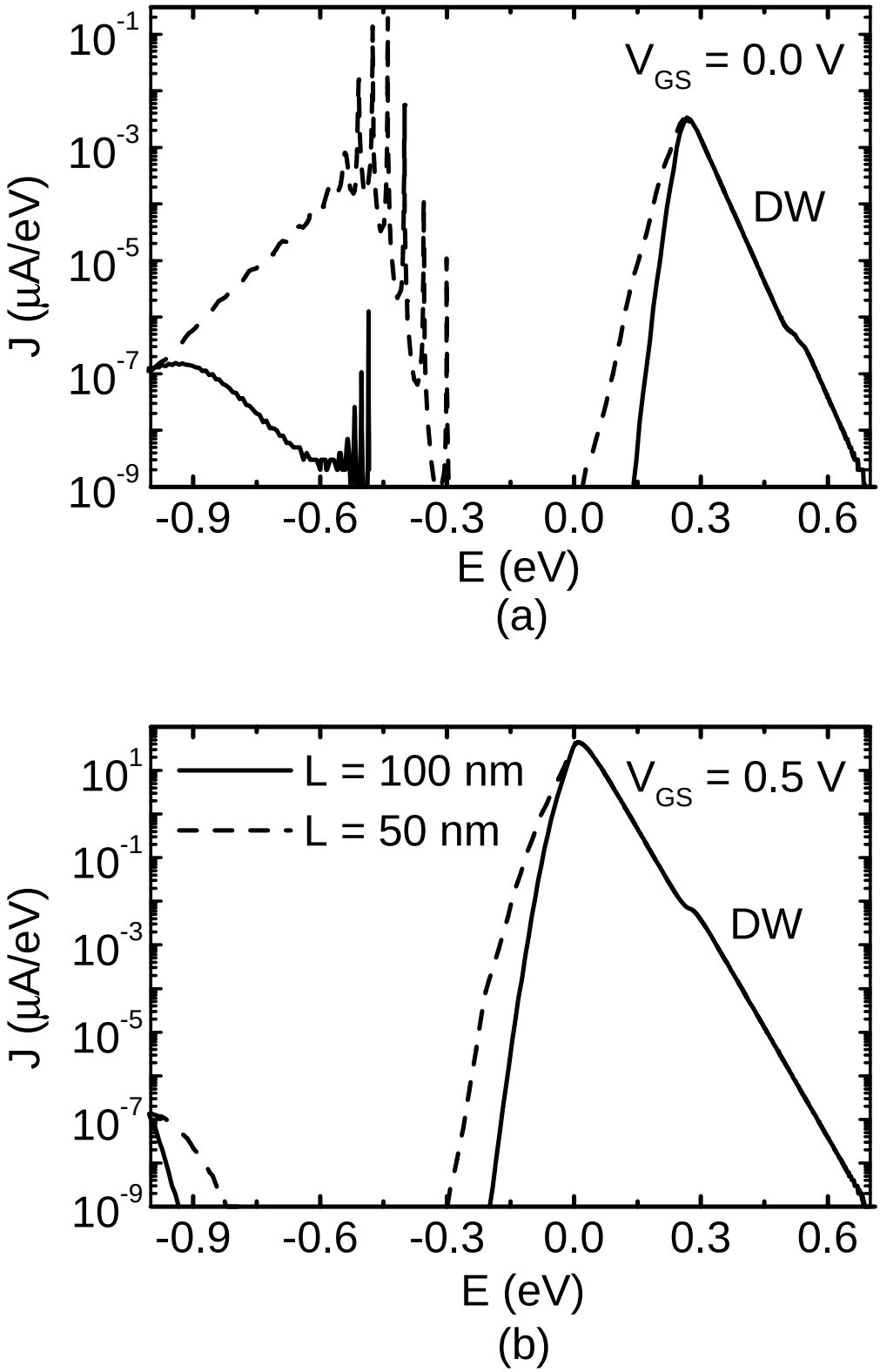

Figures 6.3: J vs E plot at two different values of channel length (a) off-state and (b) on-state. Here, $V_{DS} = 0.5$V.

Table 6.1: Performance metrics of zero-Schottky-barrier DW CNTFETs with L_g = 5 nm and t_{ox} = 2 nm.

L (nm)	I_{off} (μA)	I_{on} (μA)	I_{on}/I_{off}	S (mV/dec)	C_g (aF)	τ_S (fs)	f_T (THz)
50	5.5×10^{-4}	3.04	5.52×10^3	63.45	0.11	18.37	2.75
100	1.8×10^{-4}	2.82	1.56×10^4	60.97	0.01	1.81	21.12

energy spectrum of current, in off- and on-states for DW CNTFET only. Previously these profiles are reported for SW CNTFET [63–66]. The band profiles of DW CNTFET is the energy versus position plots at the surface of outer tube.

From the band profile of Figures 6.2 it is clear that with the increase of channel length height of the conduction band remain same (due to similar device structure and same band gap of the channel materials), but the width increases proportionately with the channel length. Due to similar height of the conduction band the thermal current remains same in both devices which is quite visible in Figures 6.3. Besides, in our model system the transport is ballistic, so the thermal current is independent of the length of the source and drain extensions. In off-state, both the electron tunneling current through the conduction band (0 < E < 0.26 eV of Figure 6.3 (a)) and hole tunneling current through the valence band (E < -0.26 eV of Figure 6.3 (a)) are much higher in CNT devices with shorter channel. The width of the conduction and the valence band is responsible for this variation of tunnel current. The on-state hole tunneling current (E < -0.52 eV of Figure 6.3 (b)) is negligible in both devices. The thermal current (0 < E < ∞ eV of Figure 6.3 (b)) is almost same in two devices due to ballistic transport and similar conduction band height. The electron tunneling current through the conduction band (-0.3 < E < 0 eV of Figure 6.3 (b)) is higher for shorter channel, making overall larger on-state current.

We compare the performance metrics, namely the transconductance g_m, the intrinsic switching delay τ_S, and the intrinsic unity current gain frequency f_T. For this the gate capacitance is calculated from Eq. (5.1).

The gate capacitance, the transconductance, the intrinsic switching delay, and the intrinsic cut-off frequency versus gate bias plots of DW CNTFET only at L = 70 nm is shown in Figures 6.4. Both the transconductance and gate capacitance peak at a gate bias $\approx$ $E_g/(2q)$ where, there is approximately a flat band situation between the potential under the gate region and the source Fermi level. This is reported previously for SW CNTFET [65, 81, 82]. As usual the on-state value of g_m is much lower in DW CNTFET due to current saturation. The intrinsic cut-off frequency peaks at V_{GS} = 0.25 V, this is very low at on-state.

The inverse subthreshold slope is defined as $S = (\partial log_{10} I_D/\partial V_{GS})^{-1}$. The most remarkable feature of DW CNTFET is its better inverse subthreshold slope [52].

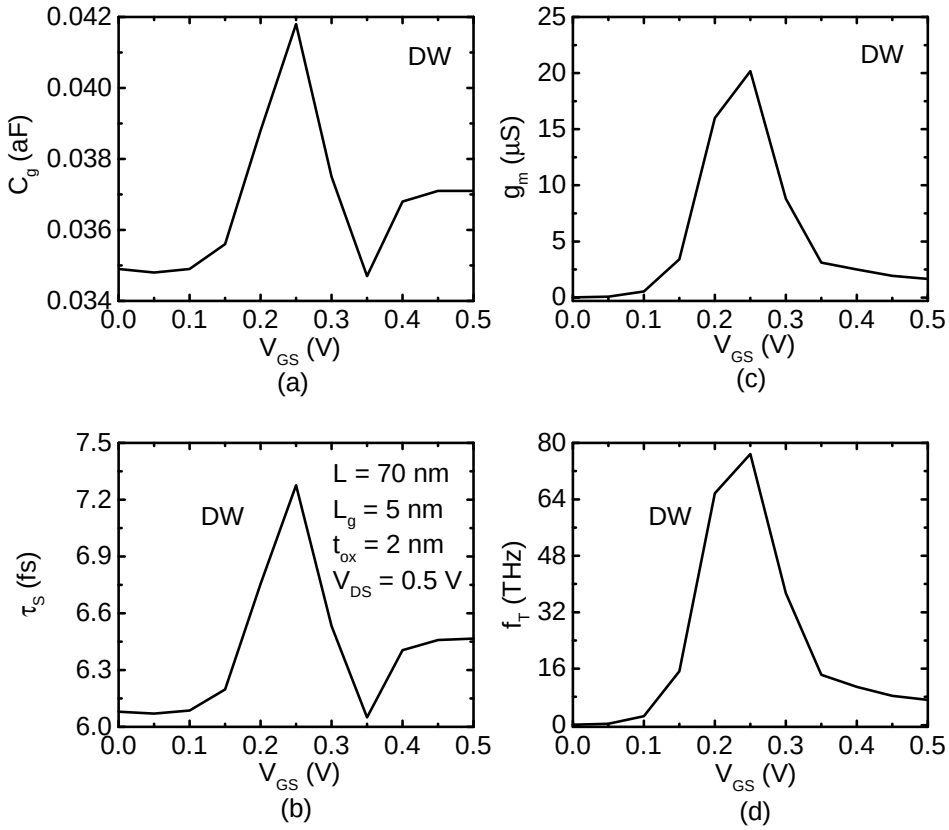

Figures 6.4: (a) Gate capacitance, (b) intrinsic switching delay, (c) transconductance and (d) intrinsic cut off frequency versus gate voltage for Schottky-barrier DW CNTFET at channel length L = 70 nm.

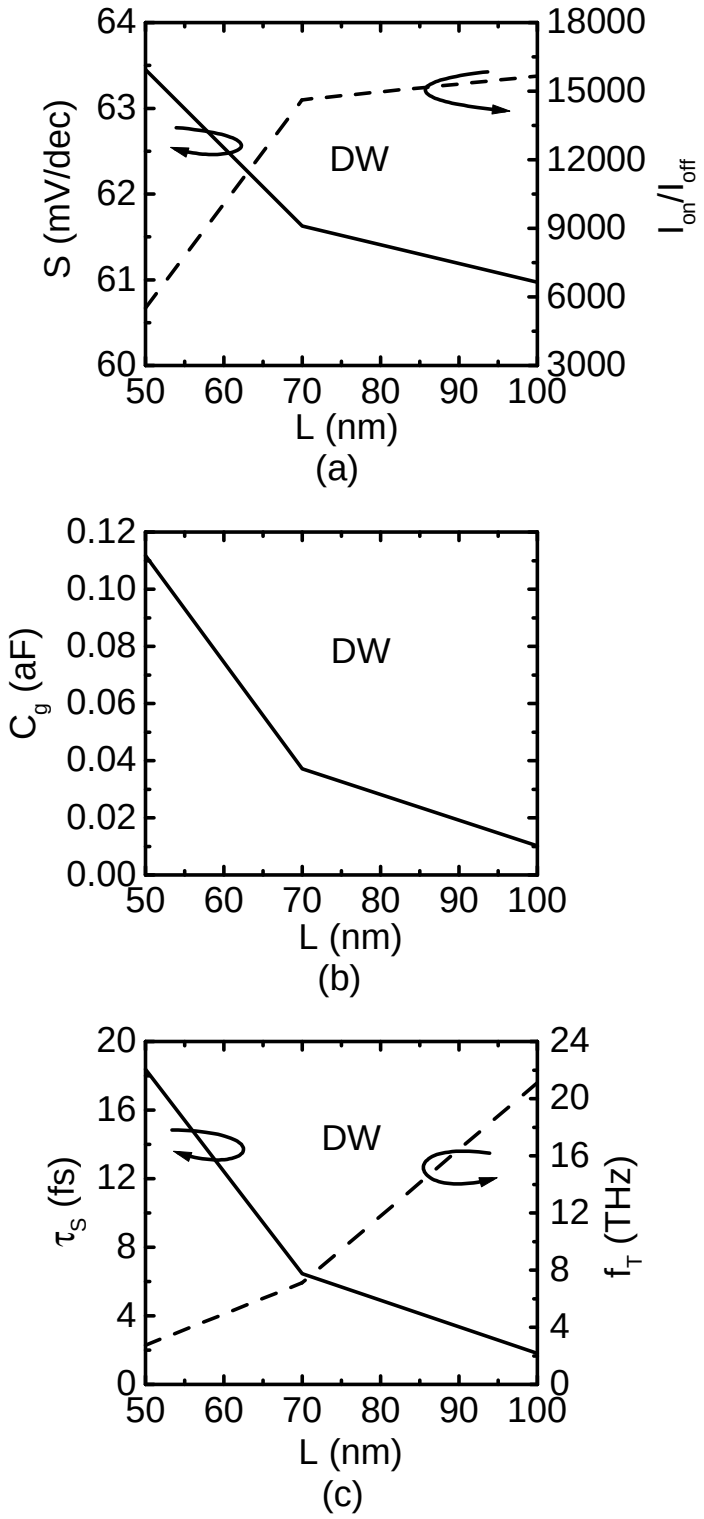

Figures 6.5: (a) Inverse subthreshold slope and on/off current ratio versus channel length. (b) On-state gate capacitance versus channel length. (c) On-state intrinsic switching delay and on-state intrinsic cut-off frequency versus channel length. Here, $V_{DS} = 0.5V$.

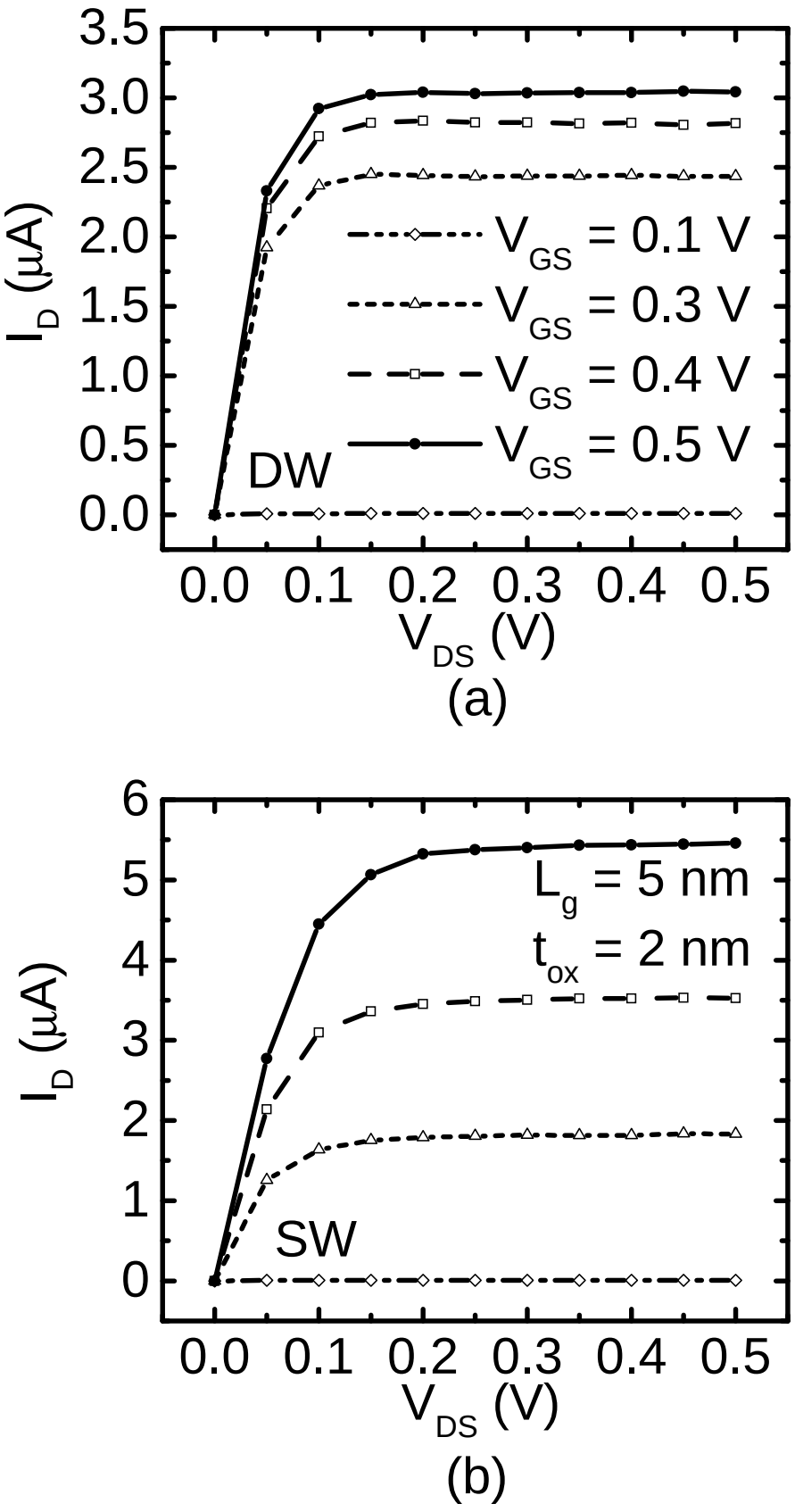

Figures 6.6: I_D-V_{DS} characteristics for different V_{GS} with channel length L = 50 nm.

The on/off current ratio and inverse subthreshold slope versus channel length are shown in Figure 6.5 (a). With the increase of channel length both the on current and off current reduces but on/off current ratio increases. This is reported before for SW CNTFET [64]. The inverse subthreshold slope decreases with the increase of channel length. So now we can say in terms of inverse subthreshold slope and on/off current ratio the performance improves with the increase of channel length. But with the increase of channel length both the device size and the chip size increases, one important limitation in this case. One important properties of DW CNTFET is with the increase of the channel length the capacitance decreases (Figure 6.5 (b)). Similar effect occurs for SW CNTFET. But for DW CNTFET it is more drastic. With shorter channel length the advantage of DW CNTFET over SW CNTFET is better inverse subthreshold slope. As a consideration of performance metrics the DW CNTFET exhibits much longer switching delay and smaller switching speed comparing to SW CNTFET (chapter 5). However, with the increase of the channel length both the intrinsic delay and switching speed improve. This is clear from Figure 6.5 (c). The switching speed of SW CNTFET also improves with larger channel. But for drastic reduction of gate capacitance of DW CNTFET its speed becomes higher than SW CNTFET. DW CNTFET exhibits better inverse subthreshold slope with smaller as well as larger channel. A detail numerical results of the performance metrics of DW CNTFET with channel length variation is supplied in Table 6.1.

The I_D vs V_{DS} curves are shown in Figures 6.6 (a) and (b), respectively, for DW and SW CNTFETs for 50 nm devices. For a particular gate voltage with the increase of the drain voltage the current first increases in linear region and then entering into saturation region it saturates. This happens for both SW and DW CNTFETs. For equal increase of gate voltage the I_D vs V_{DS} curves are equal spaced for SW CNTFET. But for DW CNTFET for high value of gate voltage the curves become closer. This is due to saturation of both the thermal current and the tunneling current of DW CNTFET at $V_{GS} \geq E_g/(2q)$ (chapter 5). The onset saturation voltage of SW CNTFET is higher than DW CNTFET and the saturation current of SW CNTFET is higher. Besides, in saturation region the drain currents become almost constant for DW CNTFET, but for SW CNTFET it slightly increases.

6.3.2 Effects of Gate Length

Now we discuss the results of the simulation of the previous device structure with constant channel length L = 50 nm and variable gate length. The I-V characteristics of the SW and DW CNTFET in Figures 6.7 exhibit same shape for same gate length. Near the upper subthreshold region current remains insensitive of gate length irrespective of SW/DW device. The I-V characteristics with gate length variation is reported before for SW CNTFET [63]. Current saturates at $V_{GS} \geq E_g/(2q)$ as usual for DW CNTFET. But for SW CNTFET in that region current moderately increases. Currents near off-state region and on-state region shift upward with the increase of gate length. But the off-state currents of both the SW and DW CNTFET vary significantly with gate length. The lowest point of the I-V curve of both devices shifts right with the increase of gate length.

To understand the I-V characteristics of DW CNTFETs with different gate lengths, we plot, in Figures 6.8, the conduction band profiles, and in Figures 6.9, the energy spectrum of current, in off- and on-states for DW CNTFET only. The conduction band profiles and the energy spectrums of current are reported before for

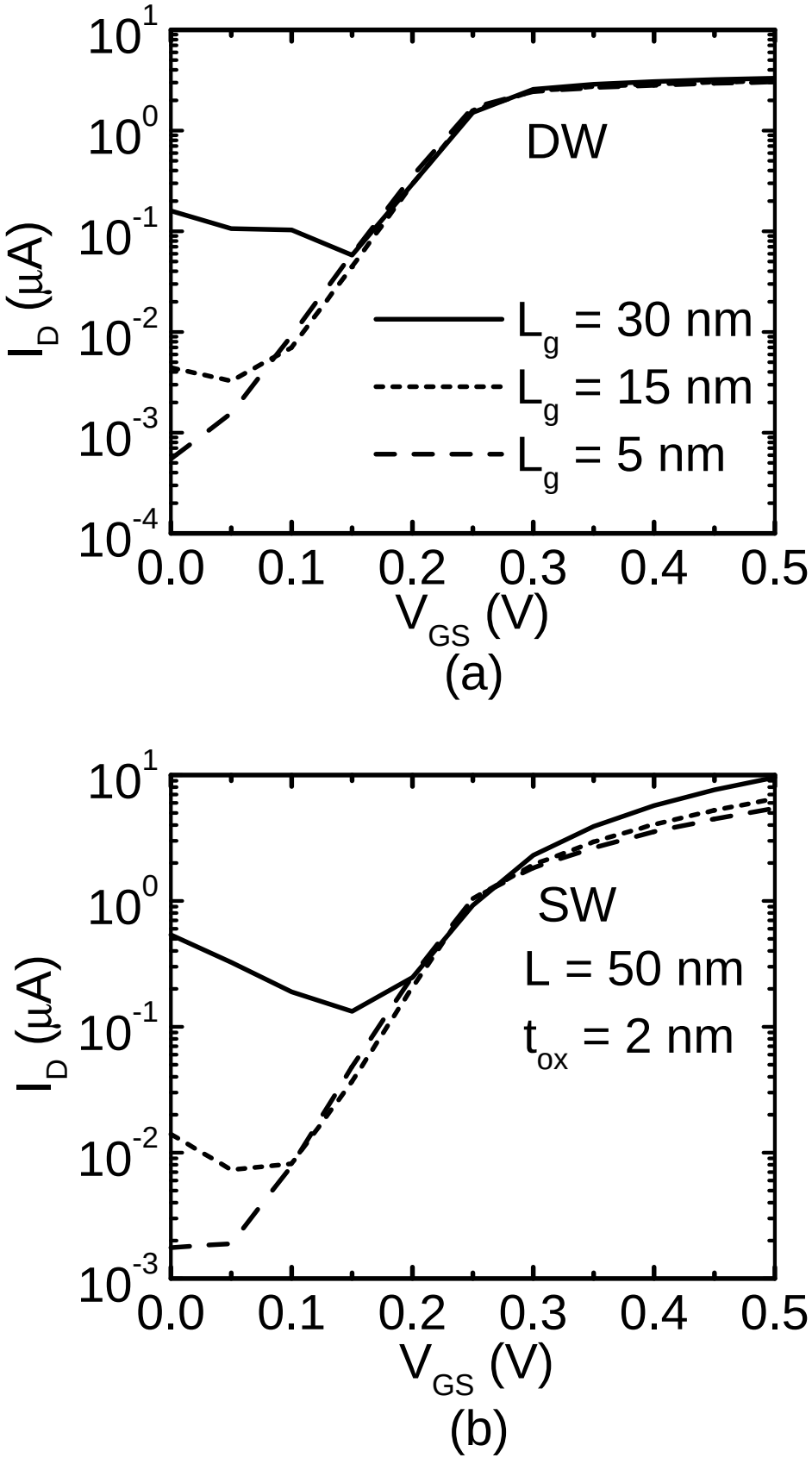

Figures 6.7: Simulated log I_D versus V_{GS} characteristics of (a) SW and (b) DW CNTFETs. Here, $V_{DS} = 0.5V$.

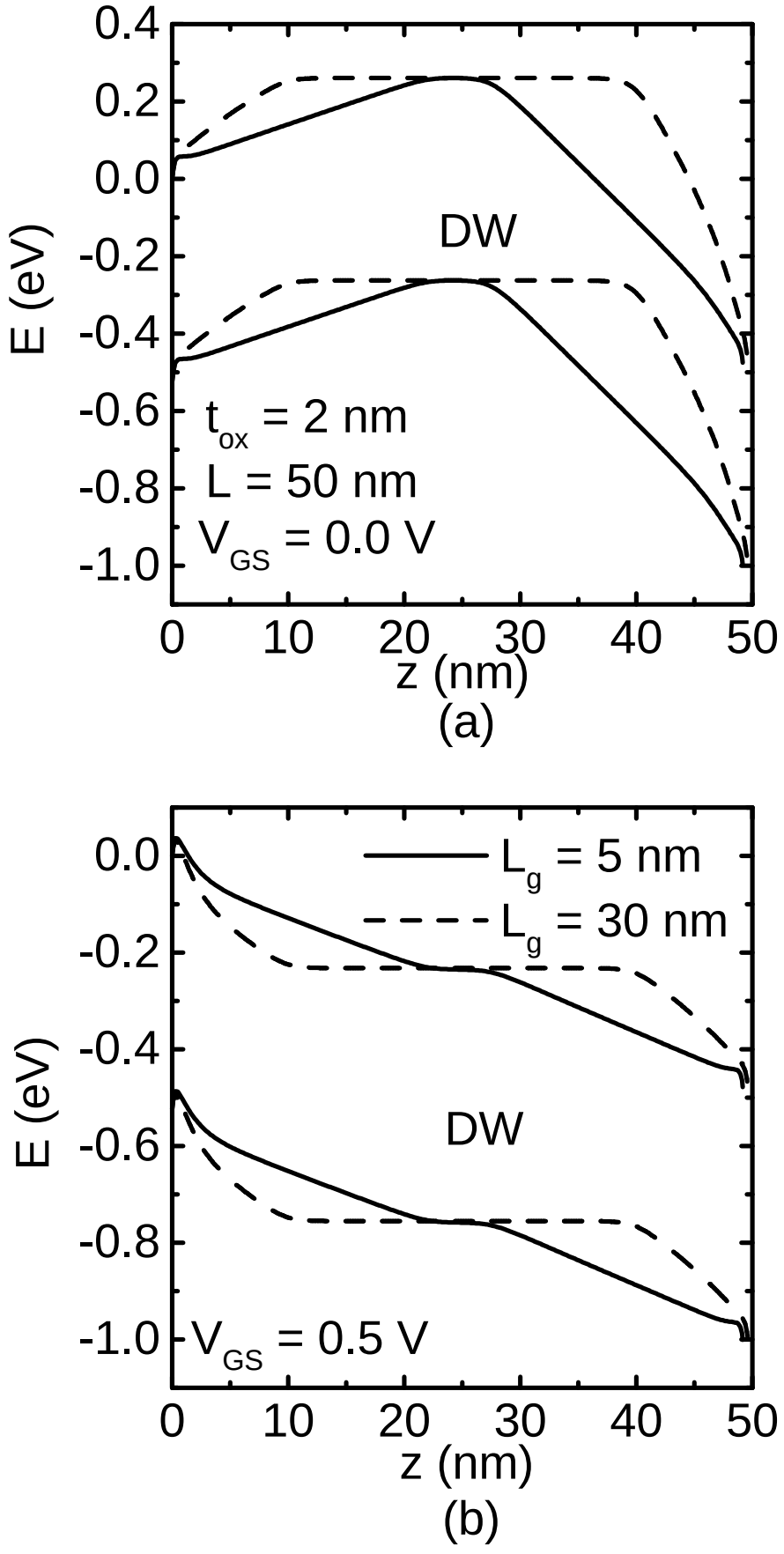

Figures 6.8: Conduction and valence band profiles at two different values of gate length (a) off-state and (b) on-state. Here, $V_{DS} = 0.5$V.

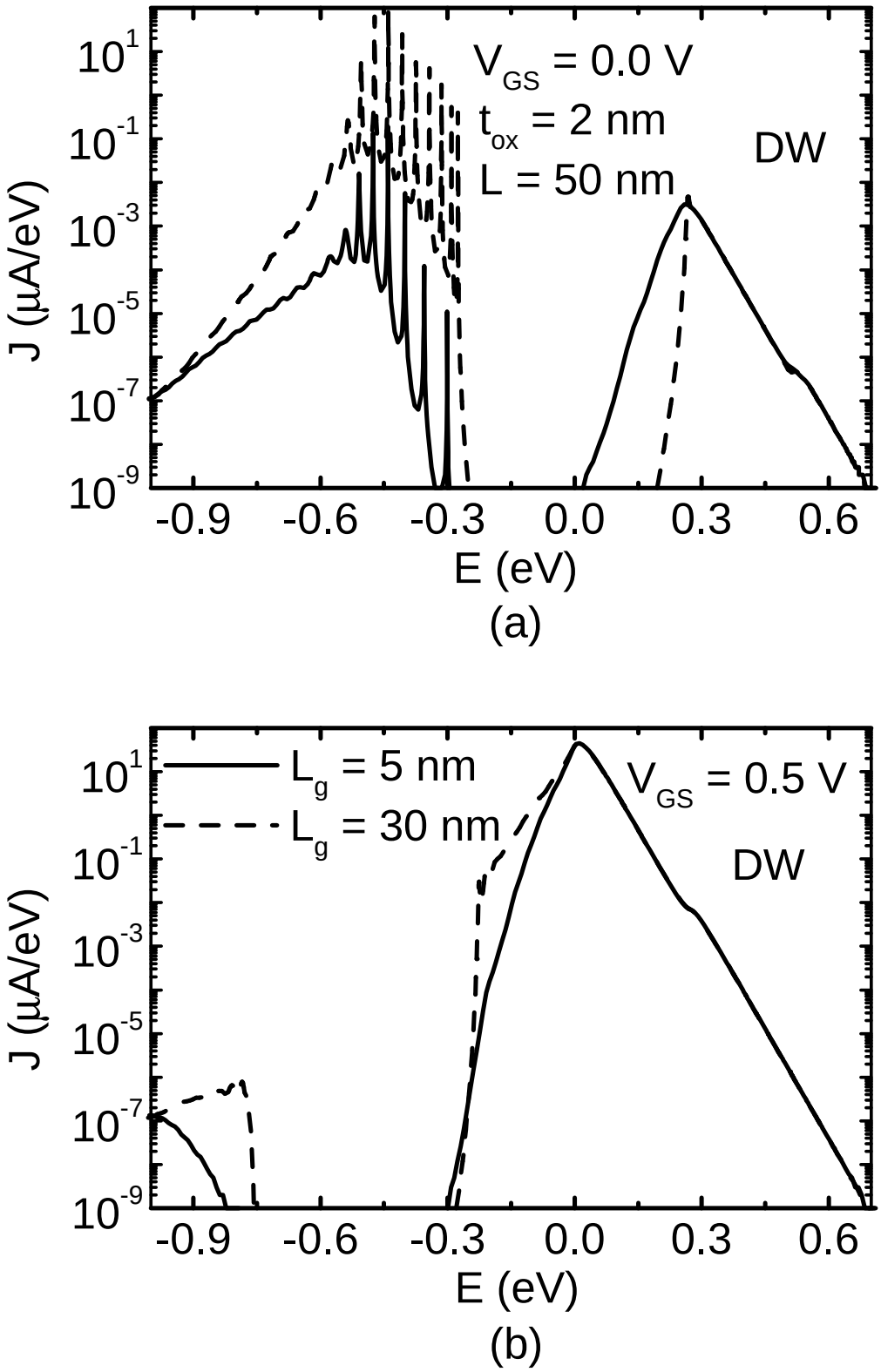

Figures 6.9: J vs E plot at two different values of gate length (a) off-state and (b) on-state. Here, $V_{DS} = 0.5$V.

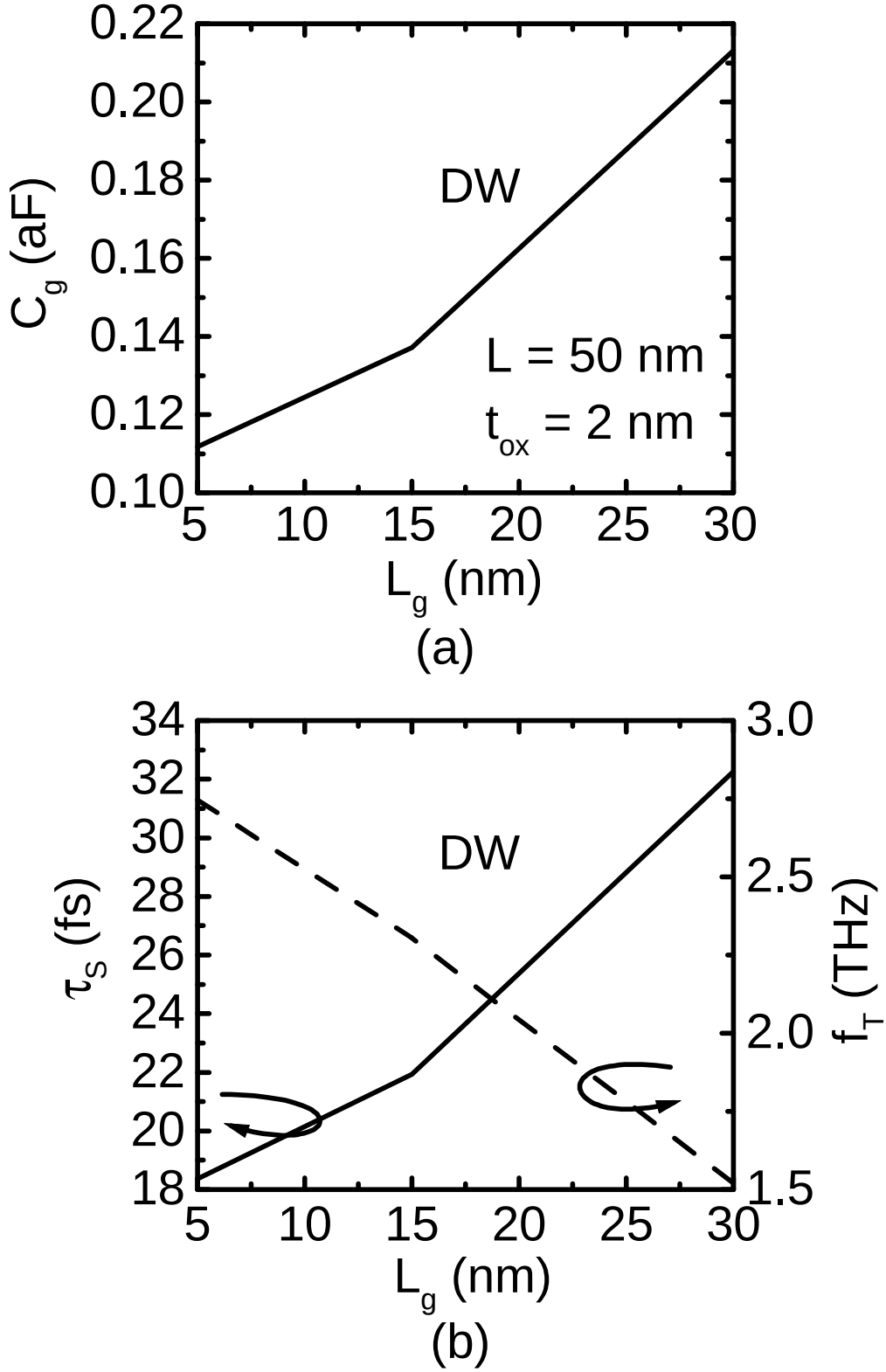

Figures 6.10: (a) On-state gate capacitance versus gate length. (b) On-state intrinsic switching delay and on-state intrinsic cut-off frequency versus gate length. Here, $V_{DS} = 0.5V$.

Table 6.2: Performance metrics of zero-Schottky-barrier DW CNTFETs with L = 50 nm and t_{ox} = 2 nm.

L_g (nm)	C_g (aF)	τ_S (fs)	f_T (THz)
5	0.11	18.37	2.75
100	0.21	32.26	1.52

SW CNTFET [63–66]. With the increase of gate length both the conduction band and valence band become much wider in off-state. Conduction band height is insensitive of gate length. For similar conduction band height and since the transport is ballistic thermal current should be insensitive of gate length. It is clearly observable in Figure 6.9 (a) for $0.26 < E < \infty$ eV. Wider conduction band is accountable for lower electron tunneling current (Figure 6.9 (a) for $0 < E < 0.26$ eV) for DW CNTFET with $L_g = 30$ nm. Wider valence band corresponds to narrower tunneling barrier for hole. That is why we get larger hole tunneling current for DW CNTFET with $L_g = 30$ nm. The difference of hole tunneling current is larger than difference of electron tunneling current. The DW CNTFET with $L_g = 30$ nm exhibits larger off current. In on-state both the electron tunneling current (Figure 6.9 (b) for $-0.3 < E < 0$ eV) and hole tunneling current (Figure 6.9 (b) for $-0.9 < E < -0.75$ eV) are larger for larger gate length DW CNTFET. The hole current is negligible in on-state.

Unlike channel length with the increase of gate length the on-state gate capacitance increases. The on-state gate capacitance versus gate length curve is shown in Figure 6.10 (a) for DW CNTFET. The intrinsic switching delay curve in Figure 6.10 (b) follows the gate-capacitance curve. The intrinsic unity current gain frequency curve show downward slope with the increase of gate length. So switching performance degrades. Figures of merit of DW CNTFET with different gate lengths are included in Table 6.2.

6.3.3 Effects of Gate Oxide Thickness

To complete the full analysis of the whole device structure we even vary the oxide thickness of the device and measure the characteristics and performance. One important finding of DW CNTFET is with the increase of oxide thickness off current increases but on current decreases (Figures 6.11) Consequently on/off current ratio decreases. So, performance degrades.

Unlike channel length and gate length with the increase of oxide thickness the top of the conduction band lowers. This is reported before for SW CNTFET [65]. The slight change of thermal current (Figure 6.13 (a) for $0.26 < E < \infty$ eV) is visible

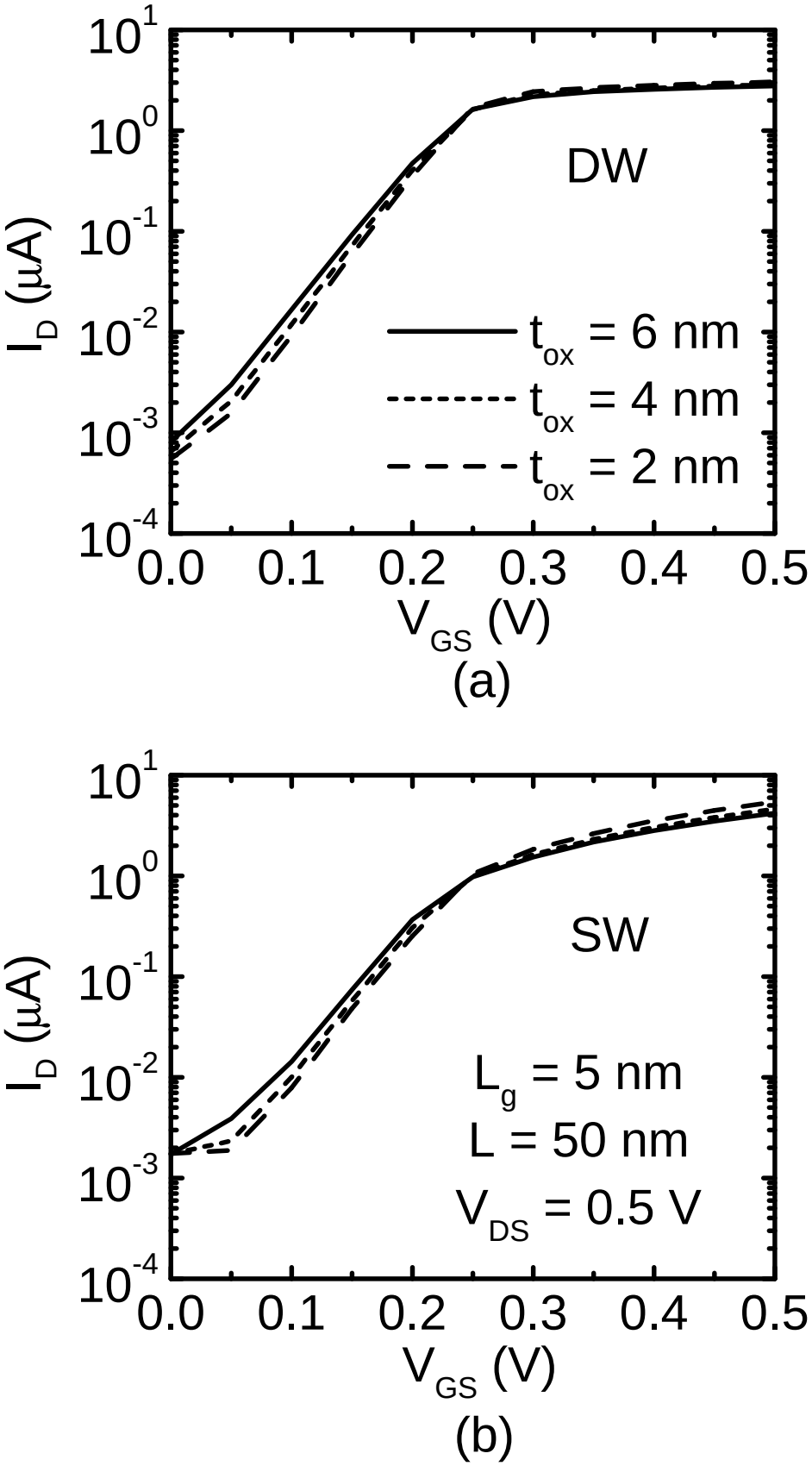

Figures 6.11: Simulated log I_D versus V_{GS} characteristics of (a) SW and (b) DW CNTFETs. Here, $V_{DS} = 0.5$V.

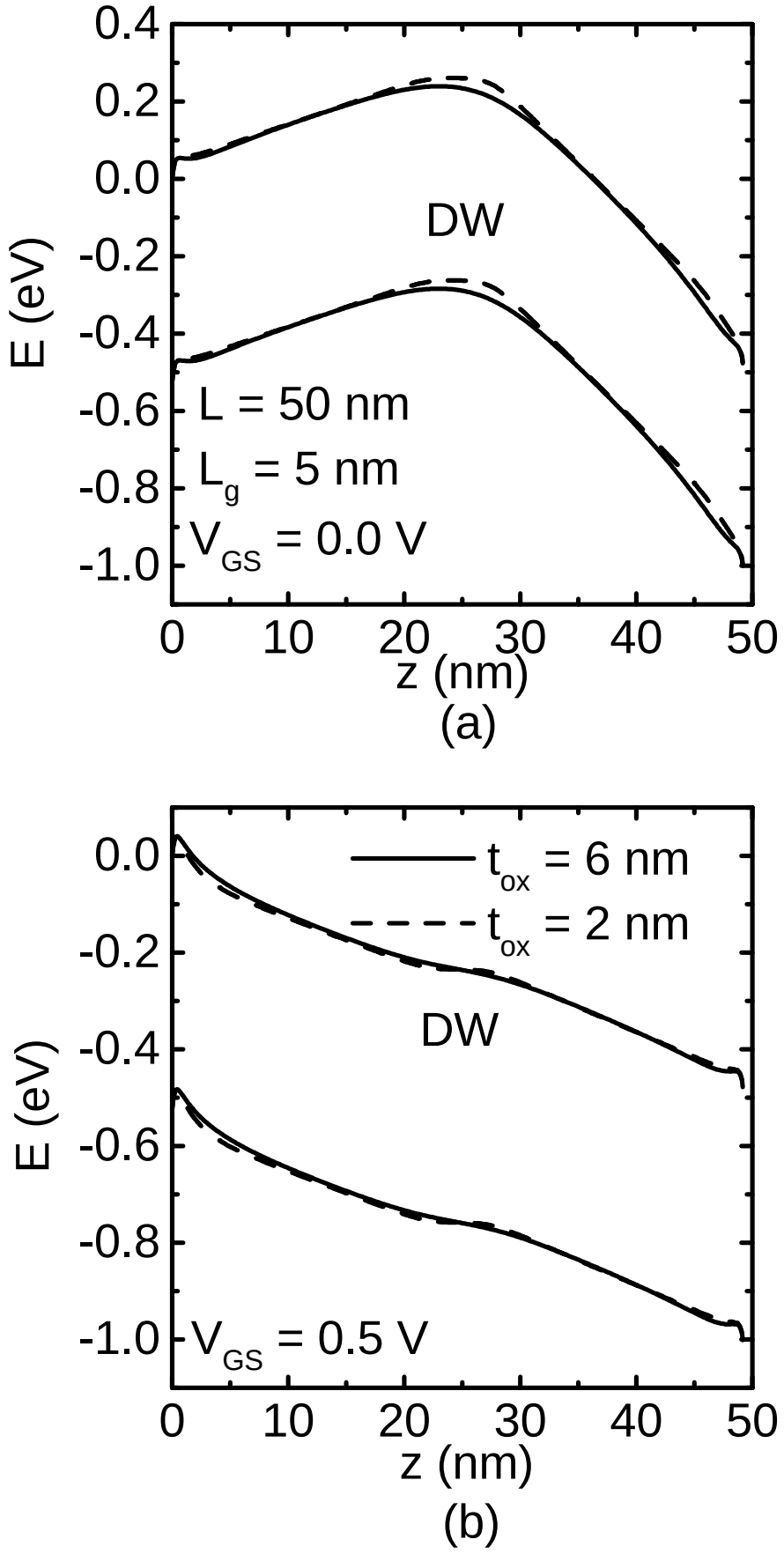

Figures 6.12: Conduction and valence band profiles at two different values of gate-oxide thickness (a) off-state and (b) on-state. Here, $V_{DS} = 0.5V$.

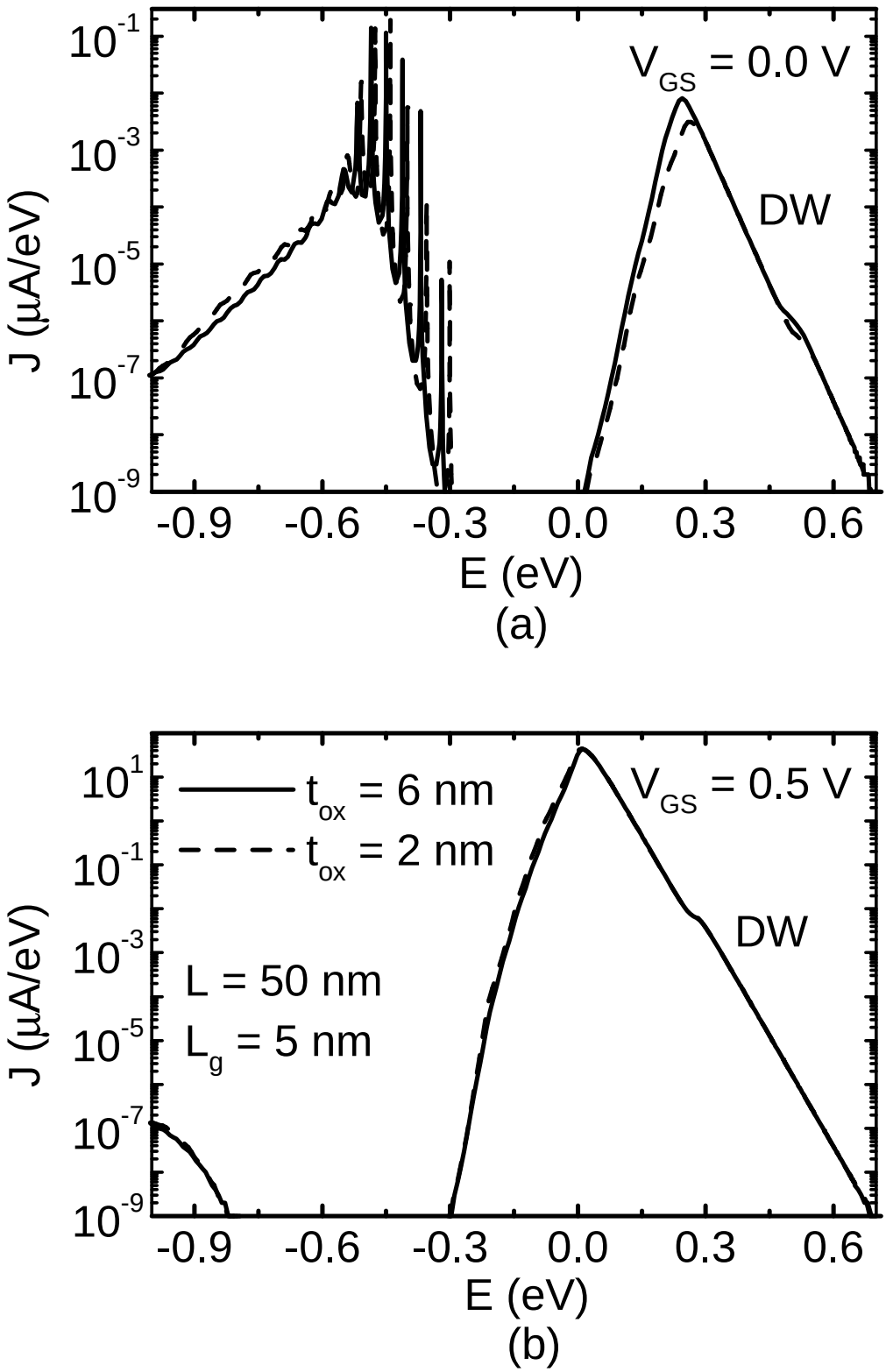

Figures 6.13: J vs E plot at two different values of gate-oxide thickness (a) off-state and (b) on-state. Here, $V_{DS} = 0.5$V.

in off-state. The conduction band becomes slightly narrower with the increase of gate oxide thickness. So, electron tunneling current (Figure 6.13 (a) for $0 < E < 0.26$ eV) increases. For narrower valence band the hole faces larger tunnel barrier. Consequently hole tunneling current decreases. But the change is not significant. The difference of electron tunneling current dominates. In on-state thermal current almost same (Figure 6.13 (b) for $0 < E < \infty$ eV), and electron and hole tunneling current slightly lower at $t_{ox} = 6$ nm.

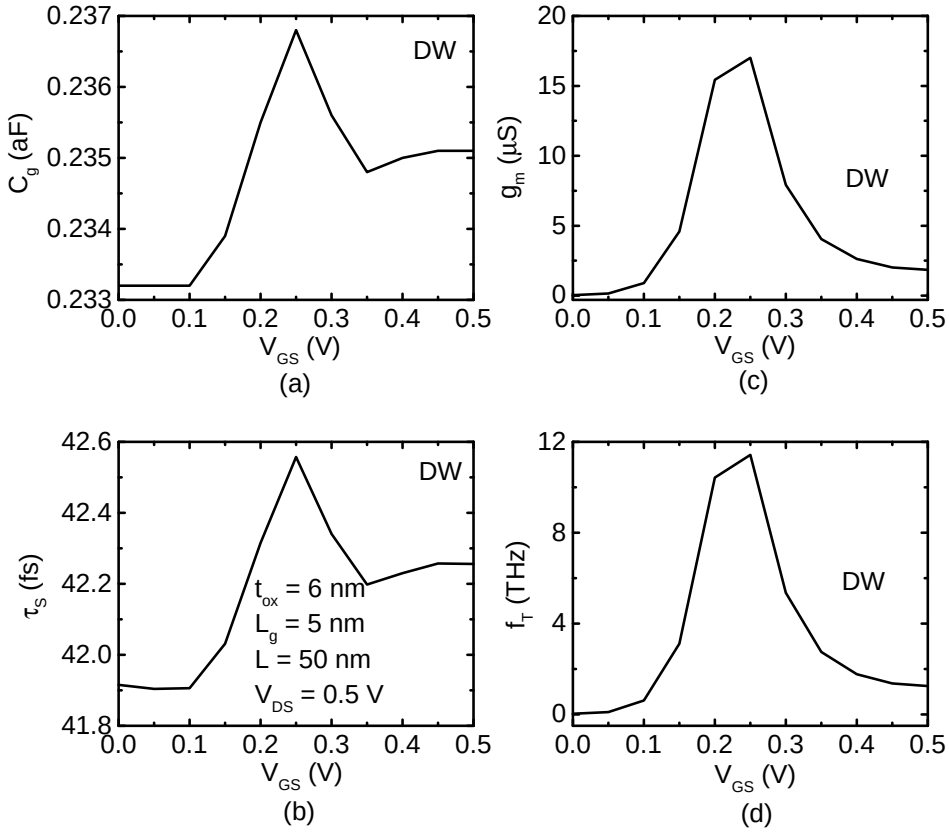

Figures 6.14: (a) Gate capacitance, (b) intrinsic switching delay, (c) transconductance and (d) intrinsic cut off frequency versus gate voltage for Schottky-barrier DW CNTFET at gate-oxide thickness $t_{ox} = 6$ nm.

The gate capacitance, the transconductance, the intrinsic switching delay, and the intrinsic cut-off frequency versus gate bias plots of DW CNTFET only at $t_{ox} = 6$ nm is shown in Figures 6.14. Gate capacitance, transconductance, intrinsic switching delay and intrinsic cut-off frequency peak at a gate bias $\approx E_g/(2q)$ as usual where, there is approximately a flat band situation between the potential under the gate region and the source Fermi level. This is reported before for SW CNTFET [65, 81, 82].

The on-state gate capacitance and the performance metrics are shown in Figures 6.15. The inverse subthreshold slope increases with the increase of gate oxide thickness. The more the inverse subthreshold slope the less the on/off current ratio. On/off current ratio decreases with increase of oxide thickness. With the increase of

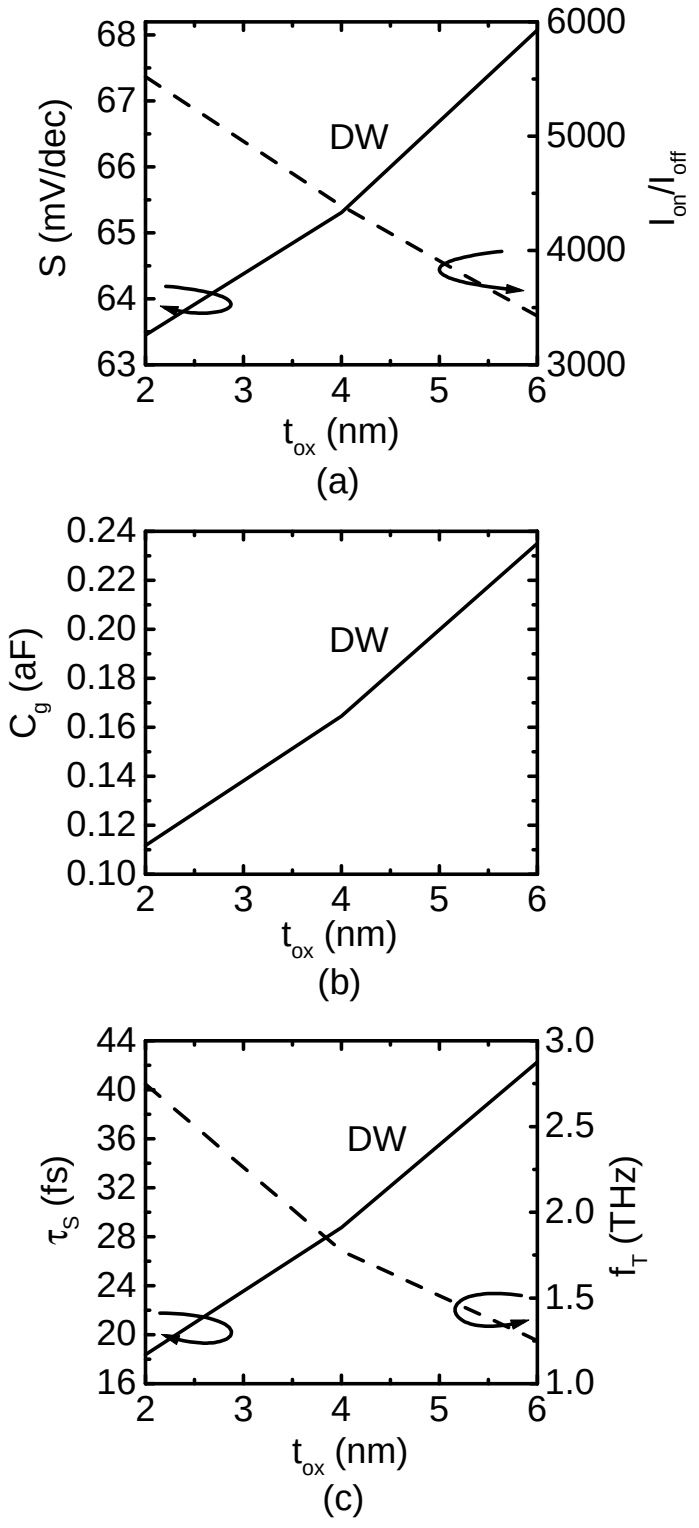

Figures 6.15: (a) Inverse subthreshold slope and on/off current ratio versus gate-oxide thickness. (b) On-state gate capacitance versus gate-oxide thickness. (c) On-state intrinsic switching delay and on-state intrinsic cut-off frequency versus gate-oxide thickness. Here, $V_{DS} = 0.5$V.

Table 6.3: Performance metrics of zero-Schottky-barrier DW CNTFETs with L_g = 5 nm and L = 50 nm.

t_{ox} (nm)	I_{off} (μA)	I_{on} (μA)	I_{on}/I_{off}	S (mV/dec)	C_g (aF)	τ_S (fs)	f_T (THz)
2	5.5×10^{-4}	3.04	5.52×10^3	63.45	0.11	18.37	2.75
6	8.12×10^{-4}	2.78	3.43×10^3	68.1	0.24	42.3	1.25

gate oxide thickness the on-state gate capacitance increases resulting bad switching performance (Figure 6.15 (c)). This is reported before for SW CNTFET [65]. Table 6.3 carries the information of performance metrics of the DW CNTFET devices with variation of oxide thickness.

6.3.4 Effects of Schottky-Barrier Height

Next we vary the Schottky-barrier height of the source-channel and drain-channel contacts. From the I-V characteristics of Figures 6.16 we can say that for SW CNTFET with the increase of the barrier height the bottom of the I-V characteristics shifts right side. For Schottky-barrier height $\phi_B = E_g/2$, we get the bottom at $V_{DS}/2$. This is reported for SW CNTFET before [49, 65]. The characteristics exhibits 'V' shape. For DW CNTFET at Schottky-barrier height other than zero, the drain current reduces with the increase of gate voltage. The characteristics exibits no trough. There is no defined on- or off- state. The on/off current ratio is very small. So, these devices lose their functionality as a FET. We can not use this structure to build electronic logic devices.

From the band diagram of Figures 6.17 at off-state it is clear that unlike zero-Schottky-barrier CNTFET the conduction band of barrier height $\phi_B = E_g/2$ peaks near the source region. Higher peak of conduction band correspond to lower thermal current. The thermal current (Figure 6.18 (a) for $0.26 < E < \infty$ eV) at off-state with $\phi_B = E_g/2$ is almost negligible. There is no electron tunneling current for range $0 < E < 0.26$ eV of Figure 6.18 (a). We get electron tunneling current in the energy range $-0.26 < E < 0$ eV. Both the electron tunneling current and hole tunneling current with $\phi_B = E_g/2$, are much higher resulting higher current at $V_{GS} = 0$ V. The thermal current is insensitive of gate voltage at $\phi_B = E_g/2$. But now we get electron tunneling current in the energy range $0 < E < 0.26$ eV (see Figure 6.18 (b)). As usual the hole tunneling current is significantly high. For $\phi_B = 0$ eV DW CNTFET both the thermal current and electron tunneling current increases with the increase of gate voltage. Only the hole tunneling current decreases.

In conclusion, a detail study of length effects on zero-Schottky-barrier DW CNTFETs with source and drain underlap is presented in this chapter. To complete the analysis of the whole device structure we have also varied the Schottky-barrier height. The I-V characteristics are almost insensitive to channel length variation and

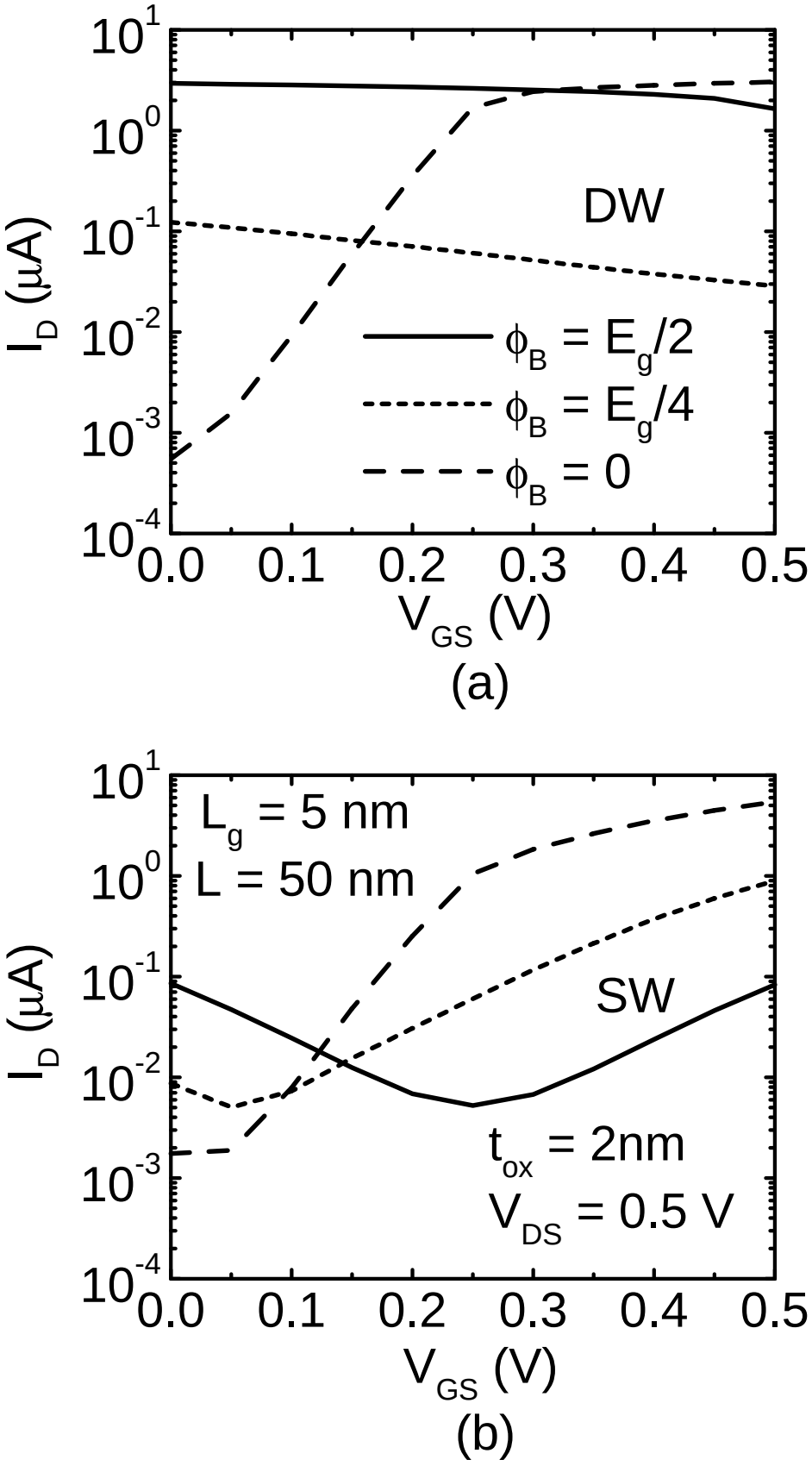

Figures 6.16: Simulated log I_D versus V_{GS} characteristics of (a) SW and (b) DW CNTFETs. Here, $V_{DS} = 0.5$V.

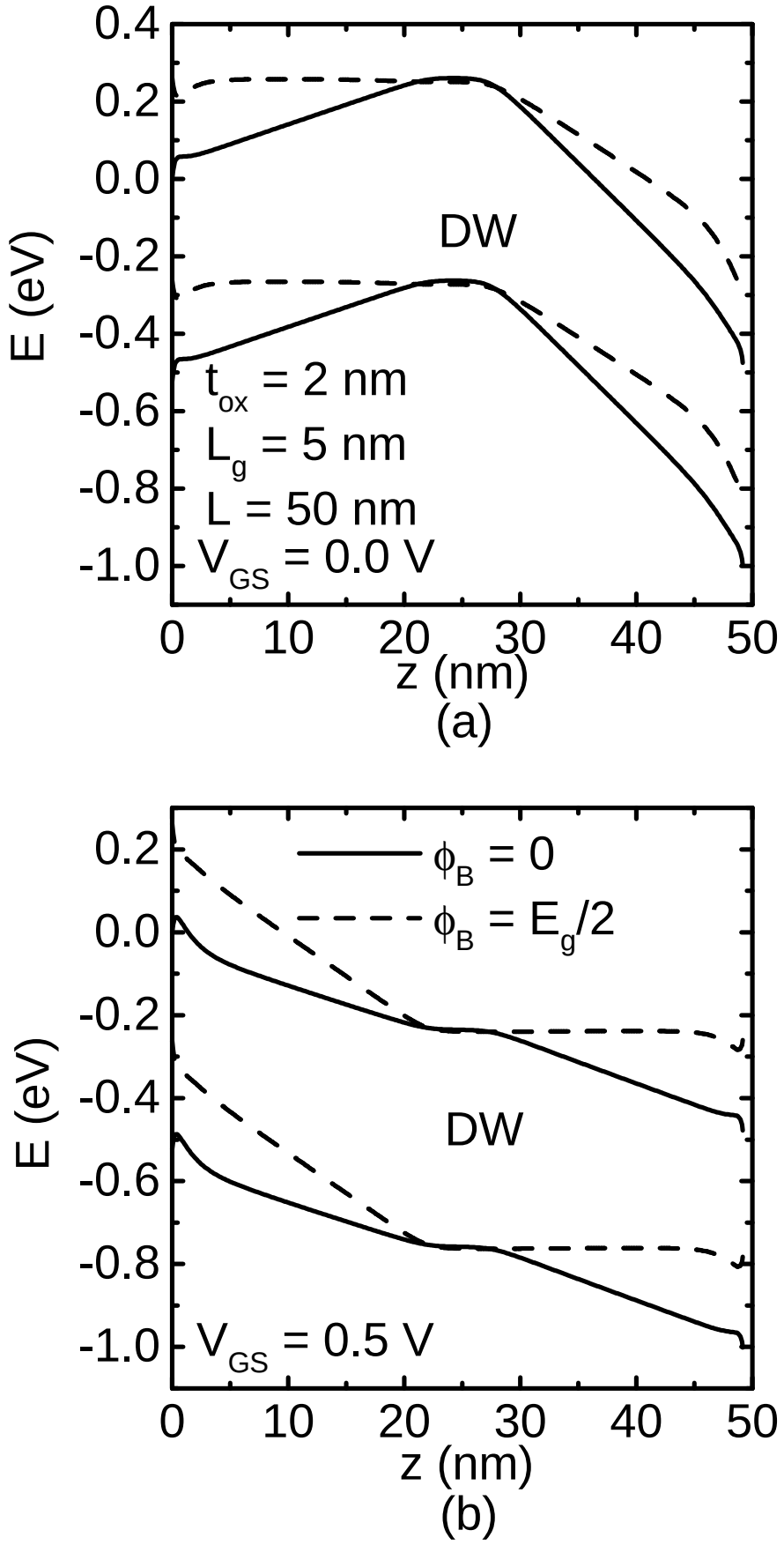

Figures 6.17: Conduction and valence band profiles at two different values of Schottky-barrier height (a) off-state and (b) on-state. Here, $V_{DS} = 0.5$V.

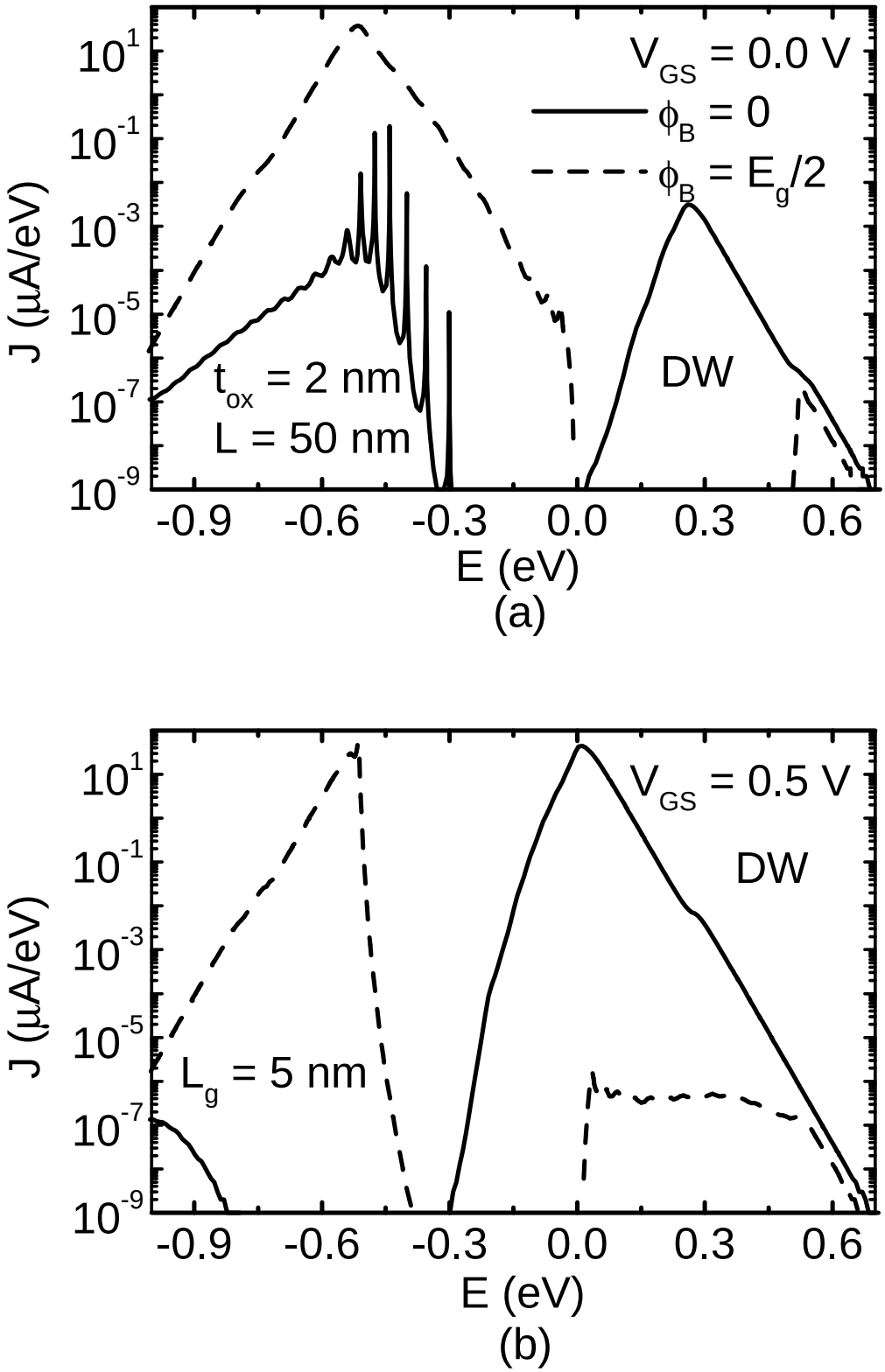

Figures 6.18: J vs E plot at two different values of Schottky-barrier height (a) off-state and (b) on-state. Here, $V_{DS} = 0.5$V.

oxide thickness variation. The off current changes considerably with gate length. With the increase of gate length this performance degrades. Only with the increase of channel length the gate capacitance reduces drastically indicating higher switching speed. For others length variation the switching speed reduces. For Schottky-barrier other than zero the DW CNT devices become useless as a logic devices losing field-effect characteristics.

Chapter 7

Conclusion and Future Research Work

7.1 Summary

In this work the following has been accomplished:

First, the whole simulation model for this research is prepared. The Poisson's solver is developed using finite difference method. This solver is used to calculate electric potential at different position of the device. Dirichlet boundary conditions are applied at the source, drain, and gate metals. Von Neumann boundary conditions are used along the exposed surface of the dielectric. There, the radial component of the electric field is set to zero. To calculate charge density recursive Green function algorithm is exploited. Simulation starts with the initial guess of zero charge density. This is input to Poisson's solver. The solution of the Poisson's solver is applied to recursive Green function algorithm to calculate charge density. This is a self-consistent process. This process continues until full convergence. Newton-Raphson method and Anderson mixing scheme are used to accelerate convergence.

Next, The simulation is started with the conductivity analysis of both SW and DW CNTs with strain. First, the numerical model of the tubes without strain is constructed by determining all lattice coordinates. To incorporate strain in this numerical tube structures each carbon-carbon bond length is varied depending on the value of strain. With the variation of bond length the bonding energy definitely changes. The bonding energy is modified through Harrison's formula. Hamiltonian matrix is formed by incorporating the energy among different orbitals of the tube. Then the band gap is determined. This process is continued for every value of strain. The band gap of DW CNT is the minimum of the two band gaps of the SW tubes from which it is constituted.

Later, research is performed in device level with SW and DW carbon nanotubes including strain. Here, self-consistent model is applied between Poisson's solver and recursive Green's function algorithm. The I-V characteristics and the C-V characteristics are observed with both uniaxial and torsional strain. With the application of tensile or torsional strain conductivity decreases. This is reflected clearly in I-V characteristics. Unlike SW CNTFET the drain current saturates in DW CNTFET at $V_{GS} \geq E_g/(2q)$. With the tensile and torsional strain off-state current and on/off current ratio improve greatly and with compressive strain on-state current improves for both devices. But improvement is better for SW CNTFET. DW CNTFET

exhibits better inverse subthreshold slope than SW CNTFET and with the application of tensile or torsional strain this improves in both devices. SW CNTFET shows more improvement of inverse subthreshold slope than DW CNTFET with strain. Unlike SW CNTFET the on-state tranconductance increases with tensile and torsional strain and decreases with compressive strain for DW CNTFET. The on-state cut-off frequency of DW CNTFET also shows opposite behavior to SW CNTFET following on-state transconductance. The DW CNTFET with 50 nm channel exhibits poor switching speed. With the application of compressive strain the switching delay improves in both devices. But again the SW CNTFET exhibits better improvement.

To complete the analysis of the whole device structure next simulation is made by varying channel length, gate length, gate oxide thickness. The I-V characteristic is almost insensitive to length variation. But small gate length or small oxide thickness results small gate capacitance which corresponds to high switching speed. Long channel consequences low gate capacitance. Better inverse subthreshold slope as well as on/off current ratio is observed with thinner oxide layer. The DW CNTs lose their functionality as a field-effect transistors with high source-channel and drain-channel Schottky-barriers.

7.2 Future Research Work

This thesis is performed by considering ballistic transport. Incorporating scattering the performance of CNT devices may be different. The whole analysis of this thesis can be repeated by slightly changing the device structure. The doped source-channel and drain-channel contacts can be incorporated instead of Schottky contacts. The doped contact DW CNTFET may be analyzed including scattering. The compact model of the DW CNTFET with or without strain has not been developed yet. In this side also there is scope to work. The Poisson's equation in this thesis is solved using finite difference method. This equation can be solved using finite element method for our CNT devices and results can be compared. The Schrodinger's equation is solved using atomistic Hamiltonian (also known as full band Hamiltonian) with recursive Green's function algorithm. This equation can be solved using effective mass Hamiltonian with non-equilibrium Green's function algorithm and results can be compared with the report of this paper. Gate oxide tunneling current has not been considered here.

References

[1] D. Frank, R. Dennard, E. Nowak, P. Solomon, Y. Taur, and H.-S. P. Wong, "Device scaling limits of si mosfets and their application dependencies," *Proceedings of the IEEE*, vol. 89, no. 3, pp. 259–288, 2001.

[2] Y. Taur, "Cmos design near the limit of scaling," *IBM Journal of Research and Development*, vol. 46, no. 2, pp. 213–222, 2002.

[3] R. H. Baughman, A. A. Zakhidov, and W. A. de Heer, "Carbon nanotubes - the route toward applications," *Science*, vol. 297, pp. 787–792, 2002.

[4] P. Avouris, J. Appenzeller, V. Derycke, R. Martel, and S. Wind, "Carbon nanotube electronics," *International Electron Devices Meeting*, pp. 281–284, 2002.

[5] R. M. P. Avouris, J. Appenzeller and S. Wind, "Carbon nanotube electronics," *Proceedings of the IEEE*, vol. 91, no. 11, pp. 1772–1784, 2003.

[6] H. Dai, "Pushing to the performance limit of carbon nanotube electronics," *61st Device Research Conference. Conference Digest (Cat. No.03TH8663)*, p. 165, 2003.

[7] S. Heinze, J. Tersoff, and P. Avouris, "Carbon nanotube electronics and optoelectronics," *Lect. Notes Phys.*, vol. 680, pp. 381–409, 2005.

[8] A. Javey and H. Dai, "Carbon nanotube electronics," *19th International Conference on VLSI Design held jointly with 5th International Conference on Embedded Systems and Design*, pp. 453–458, 2006.

[9] T. Durkop, S. Getty, E. Cobas, and M. Fuhrer, "Extraordinary mobility in semiconducting carbon nanotubes," *Nano Lett.*, vol. 4, no. 1, pp. 35–39, 2004.

[10] S. Iijima, "Helical microtubules of graphitic carbon," *Nature*, vol. 354, pp. 56–58, 1991.

[11] R. Martel, T. Schmidt, H. R. Shea, T. Hertel, and P. Avouris, "Single- and multiwall carbon nanotube field-effect transistors," *Appl. Phys. Lett.*, vol. 73, no. 17, pp. 2447–2449, 1998.

[12] S. J. Tans, A. R. M. Verschueren, and C. Dekker, "Room-temperature transistor based on a single carbon nanotube," *Nature*, vol. 393, pp. 49–52, 1998.

[13] J. Guo, S. Datta, M. Lundstrom, M. Brink, P. McEuen, A. Javey, H. Dai, H. Kim, and P. McIntyre, "Assessment of silicon mos and carbon nanotube fet performance limits using a general theory of ballistic transistors," *International Electron Devices Meeting*, pp. 711–714, 2002.

[14] S. Heinze, M. Radosavljevic, J. Tersoff, and P. Avouris, "Unexpected scaling of the performance of carbon nanotube schottky-barrier transistors," *Phys. Rev. B*, vol. 68, no. 2, pp. 235418(1–5), 2003.

[15] M. Radosavljevic, S. Heinze, J. Tersoff, and P. Avouris, "Drain voltage scaling in carbon nanotube transistors," *Appl. Phys. Lett.*, vol. 83, no. 12, pp. 2435–2437, 2003.

[16] J. Guo, J. Wang, E. Polizzi, S. Datta, and M. Lundstrom, "Electrostatics of nanowire transistors," *IEEE Trans. Nanotechnol.*, vol. 2, no. 4, pp. 329–334, 2003.

[17] S. Heinze, J. Tersoff, R. Martel, V. Derycke, J. Appenzeller, and P. Avouris, "Carbon nanotubes as schottky barrier transistors," *Phys. Rev. Lett.*, vol. 89, no. 10, pp. 106801(1–4), 2002.

[18] S. Heinze, J. Tersoff, and P. Avouris, "Electrostatic engineering of nanotube transistors for improved performance," *Appl. Phys. Lett.*, vol. 83, no. 24, pp. 5038–5040, 2003.

[19] Y. M. Lin, J. Appenzeller, and P. Avouris, "Ambipolar-to-unipolar conversion of carbon nanotube transistors by gate structure engineering," *Nano Lett.*, vol. 4, no. 5, pp. 947–950, 2004.

[20] R. Martel, V. Derycke, C. Lavoie, J. Appenzeller, K. K. Chan, J. Tersoff, and P. Avouris, "Ambipolar electrical transport in semiconducting single wall carbon nanotubes," *Phys. Rev. Lett.*, vol. 87, no. 25, pp. 256805(1–4), 2001.

[21] V. Derycke, R. Martel, J. Appenzeller, and P. Avouris, "Controlling doping and carrier injection in carbon nanotube transistors," *Appl. Phys. Lett.*, vol. 80, no. 15, pp. 2773–2775, 2002.

[22] X. Cui, M. Freitag, R. Martel, L. Brus, and P. Avouris, "Controlling energy-level alignments at carbon nanotube/au contacts," *Nano Lett.*, vol. 3, no. 6, pp. 783–787, 2003.

[23] S. Auvray, J. Borghetti, M. F. Goffman, A. Filoramo, V. Derycke, J. P. Bourgoin, and O. Jost, "Carbon nanotube transistor optimization by chemical control of the nanotube-metal interface," *Appl. Phys. Lett.*, vol. 84, no. 25, pp. 5106–5108, 2004.

[24] A. Javey, J. Guo, Q. Wang, M. Lundstrom, and H. Dai, "Ballistic carbon nanotube field-effect transistors," *Nature*, vol. 424, pp. 654–657, 2003.

[25] W. Kim, A. Javey, R. Tu, J. Cao, Q. Wang, and H. Dai, "Electrical contacts to carbon nanotubes down to 1 nm in diameter," *Appl. Phys. Lett.*, vol. 87, no. 17, pp. 173101(1–3), 2005.

[26] Z. Zhang, X. Liang, S. Wang, K. Yao, Y. Hu, Y. Zhu, Q. Chen, W. Z., Y. Li, Y. Yao, J. Zhang, and L.-M. Peng, "Doping-free fabrication of carbon nanotube based ballistic cmos devices and circuits," *Nano Lett.*, vol. 7, no. 12, pp. 3603–3607, 2007.

[27] P. J. Burke, "Ac performance of nanoelectronics: towards a ballistic thz nanotube transistor," *Solid-State Electron.*, vol. 48, pp. 1981–1986, 2004.

[28] D. V. Singh, K. A. Jenkins, J. Appenzeller, D. Neumayer, A. Grill, and H. S. P. Wong, "Frequency response of top-gated carbon nanotube field-effect transistors," *IEEE Trans. Nanotechnol.*, vol. 3, no. 3, pp. 383–387, 2004.

[29] J. Appenzeller and D. J. Frank, "Frequency depedent characterization of transport properties in carbon nanotube transistors," *Appl. Phys. Lett.*, vol. 84, no. 10, pp. 1771–1773, 2004.

[30] S. Ito, H. Namba, K. Yamaguchi, T. Hirata, K. Ando, S. Koyama, S. Kuroki, N. Ikezawa, T. Suzuki, T. Saitoh, and T. Horiuchi, "Mechanical stress effect of etch-stop nitride and its impact on deep submicron transistor design," *International Electron Devices Meeting*, pp. 247–250, 2000.

[31] A. Shimizu, K. Hachimine, N. Ohki, H. Ohta, M. Koguchi, Y. Nonaka, H. Sato, and F. Ootsuka, "Local mechanical-stress control (lmc): A new technique for cmos-performance enhancement," *International Electron Devices Meeting*, pp. 19.4.1–19.4.4, 2001.

[32] C. L. Kane and E. J. Mele, "Size, shape, and low energy electronic structure of carbon nanotubes," *Phys. Rev. Lett.*, vol. 78, no. 10, pp. 1932–1935, 1997.

[33] R. Heyd, A. Charlier, and E. McRae, "Uniaxial-stress effects on the electronic properties of carbon nanotubes," *Phys. Rev. B*, vol. 55, no. 11, pp. 6820–6824, 1997.

[34] A. Rochefort, D. R. Salahub, and P. Avouris, "The effect of structural distortions on the electronic structure of carbon nanotubes," *Chem. Phys. Lett.*, vol. 297, pp. 45–50, 1998.

[35] L. Yang, M. P. Anantram, J. han, and J. P. Lu, "Band-gap change of carbon nanotubes: Effect of small uniaxial and torsional strain," *Phys. Rev. B*, vol. 60, no. 19, pp. 13874–13878, 1999.

[36] M. Nardelli and J. Bernholc, "Mechanical deformations and coherent transport in carbon nanotubes," *Phys. Rev. B*, vol. 60, no. 24, pp. 16338–16341, 1999.

[37] A. Rochefort, P. Avouris, F. Lesage, and D. R. Salahub, "Electrical and mechanical properties of distorted carbon nanotubes," *Phys. Rev. B*, vol. 60, no. 19, pp. 13824–13830, 1999.

[38] A. Kleiner and S. Eggert, "Band gaps of primary metallic carbon nanotubes," *Phys. Rev. B*, vol. 63, no. 7, pp. 073408(1–4), 2001.

[39] L. Yang and J. Han, "Electronic structure of deformed carbon nanotubes," *Phys. Rev. Lett.*, vol. 85, no. 1, pp. 154–157, 2000.

[40] L. Liu, C. S. Jayanthi, M. Tang, S. Wu, T. W. Tombler, C. Zhou, L. Alexseyev, J. Kong, and H. Dai, "Controllable reversibility of an sp2 to sp3 transition of a single wall nanotube under the manipulation of an afm tip: A nanoscale electromechanical switch?," *Phys. Rev. Lett.*, vol. 84, no. 21, pp. 4950–4953, 2000.

[41] A. Maiti, A. Svizhenko, and M. P. Anantram, "Electronic transport through carbon nanotubes: effects of structural deformation and tube chirality," *Phys. Rev. Lett.*, vol. 88, no. 12, pp. 126805(1–4), 2002.

[42] M.-F. Yu, O. Lourie, M. J. Dyer, K. Moloni, T. F. Kelly, and R. S. Ruoff, "Strength and breaking mechanism of multiwalled carbon nanotubes under tensile load," *Science*, vol. 287, no. 5453, pp. 637–640, 2000.

[43] J. P. Salvetat, J. M. Bonard, N. H. Thomson, A. J. Kulik, L. Forro, W. Benoit, and L. Zuppiroli, "Mechanical properties of carbon nanotubes," *Appl. Phys. A*, vol. 69, pp. 255–260, 1999.

[44] T. W. Tombler, C. Zhou, L. Alexseyev, J. Kong, H. Dai, L. Liu, C. S. Jayanthi, M. tang, and S. Wu, "Reversible electromechanical characteristics of carbon nanotubes under local-probe manipulation," *Nature*, vol. 405, pp. 769–772, 2000.

[45] E. D. Minot, Y. Yaish, V. Sazonova, J.-Y. Park, M. Brink, and P. L. McEuen, "Tuning carbon nanotube band gaps with strain," *Phys. Rev. Lett.*, vol. 90, no. 15, pp. 156401(1–4), 2003.

[46] J. Cao, Q. Wang, and H. Dai, "Electromechanical properties of metallic, quasimetallic, and semiconducting carbon nanotubes under stretching," *Phys. Rev. Lett.*, vol. 90, no. 15, pp. 157601(1–4), 2003.

[47] H. Maune and M. Bockrath, "Elastomeric carbon nanotube circuits for local strain sensing," *Appl. Phys. Lett.*, vol. 89, no. 17, pp. 173131(1–3), 2006.

[48] T. Cohen-karni, L. Segev, O. Srur-Lavi, S. R. Cohen, and E. Joselevich, "Torsional electromechanical quantum oscillations in carbon nanotubes," *Nature Nanotechnology*, vol. 1, no. 1, pp. 36–41, 2006.

[49] Y. Yoon and J. Guo, "Analysis of strain effects in ballistic carbon nanotube fets," *IEEE Trans. Electron Dev.*, vol. 54, no. 6, pp. 1280–1287, 2007.

[50] Y. A. Kim, H. Muramatsu, T. Hayashi, M. Endo, M. Terrones, and M. S. Dresselhaus, "Thermal stability and structural changes of double-walled carbon nanotubes by heat treatment," *Chem. Phys. Lett.*, vol. 398, pp. 87–92, 2004.

[51] M. Endo, H. Muramatsu, T. Hayashi, Y. A. Kim, M. Terrones, and M. S. Dresselhaus, "'buckypaper' from coaxial nanotubes," *Nature*, vol. 433, p. 476, 2005.

[52] T. Shimada, T. sugai, Y. Ohno, S. Kishimoto, T. Mizutani, H. Yoshida, T. Okazaki, , and H. Shinohara, "Double-wall carbon nanotube field-effect transistors: Ambipolar transport characteristics," *Appl. Phys. Lett.*, vol. 84, no. 13, pp. 2412–2414, 2004.

[53] D. Kang, N. Park, J. Hyun, E. Bae, J. Ko, J. Kim, and W. Park, "Adsorption-induced conversion of the carbon nanotube field effect transistor from ambipolar to unipolar behavior," *Appl. Phys. Lett.*, vol. 86, no. 9, pp. 093105(1–3), 2005.

[54] S. Wang, X. Liang, Q. Chen, Z. Zhang, and L. peng, "Field-effect characteristics and screening in double-walled carbon nanotube field-effect transistors," *J. Phys. Chem. B*, vol. 109, pp. 17361–17365, 2005.

[55] Y. Li, R. Hatakeyama, T. Kaneko, T. Izumida, T. Okada, and T. Kato, "Electronic transport properties of Cs-encapsulated double-walled carbon nanotubes," *Appl. Phys. Lett.*, vol. 89, no. 9, pp. 093110(1–3), 2006.

[56] S. Wang and M. Grifoni, "Schottky-barrier double-walled carbon-nanotube field-effect transistors," *Phys. Rev. B*, vol. 76, no. 3, pp. 033413(1–4), 2007.

[57] M. Kociak, K. Suenaga, K. Hirahara, Y. Saito, T. Nakahira, and S. Iijima, "Linking chiral indices and transport properties of double-walled carbon nanotubes," *Phys. Rev. Lett.*, vol. 89, no. 15, pp. 155501(1–4), 2002.

[58] R. Lake, G. Klimeck, R. C. Bowen, and D. Jovanovic, "Single and multiband modeling of quantum electron transport through layered semiconductor devices," *J. Appl. Phys.*, vol. 81, no. 12, pp. 7845–7869, 1997.

[59] J. C. Slonczewski and P. R. Weiss, "Band structure of graphite," *Phys. Rev.*, vol. 109, no. 2, pp. 272–279, 1958.

[60] S. Bandow, M. Takizawa, K. Hirahara, and M. Y. S. Iijima, "Raman scattering study of double-wall carbon nanotubes derived from the chains of fullerenes in single-wall carbon nanotubes," *Chem. Phys. Lett.*, vol. 337, pp. 48–54, 2001.

[61] J. W. McClure, "Band structure of graphite and de haas-van effect," *Phys. Rev.*, vol. 108, no. 3, pp. 612–618, 1957.

[62] T. Natsuki, K. Tantrakarn, and M. Endo, "Effects of carbon nanotube structures on mechanical properties," *Appl. Phys. A*, vol. 79, no. 1, pp. 117–124, 2004.

[63] K. Alam and R. Lake, "Leakage and performance of zero-schottky-barrier carbon nanotube transistors," *J. Appl. Phys.*, vol. 98, no. 3, pp. 064307(1–10), 2005.

[64] K. Alam and R. Lake, "Performance of 2 nm gate length carbon nanotube field-effect transistors with source/drain underlaps," *Appl. Phys. Lett.*, vol. 87, no. 7, pp. 073104(1–3), 2005.

[65] K. Alam and R. Lake, "Dielectric scaling of a zero-schottky-barrier, 5 nm gate, carbon nanotube transistor with source/drain underlaps," *J. Appl. Phys.*, vol. 100, no. 2, pp. 024317(1–7), 2006.

[66] K. Alam and R. Lake, "Role of doping in carbon nanotube transistors with source/drain underlaps," *IEEE Transections on Nanotechnology*, vol. 6, no. 6, pp. 652–658, 2007.

[67] G. D. Wilk, R. M. Wallace, and J. M. Anthony, "High-k gate dielectrics: current status and materials properties considerations," *J. Appl. Phys.*, vol. 89, no. 10, pp. 5243–5275, 2001.

[68] S. J. Tans, A. R. M. Verschueren, and C. Dekker, "Room-temperature transistor based on a single carbon nanotube," *Nature*, vol. 393, pp. 49–52, 1998.

[69] S. Datta, *Quantum Transport Atom to Transistor*. Cambridge: Cambridge University Press, 2005.

[70] V. Eyert, "A comparative study on methods for convergence acceleration of iterative vector sequences," *J. Comput. Phys.*, vol. 124, no. 0059, pp. 271–285, 1996.

[71] M. F. Yu, O. Lourie, M. J. Dyer, K. Moloni, T. F. Kelly, and R. S. Ruoff, "Strength and breaking mechanism of multiwalled carbon nanotubes under tensile load," *Science*, vol. 287, no. 5453, pp. 637–640, 2000.

[72] D. Qian, G. J. Wagner, W. K. Liu, M. F. Yu, and R. S. Ruoff, "Mechanics of carbon nanotubes," *Appl Mech Rev*, vol. 55, no. 6, pp. 495–533, 2002.

[73] S. Uryu and T. Ando, "Electronic intertube transfer in double-wall carbon nanotubes with impurities: Tight-binding calculations," *Phys. Rev. B*, vol. 76, no. 15, pp. 155434(1–8), 2007.

[74] T. Nakanishi and T. Ando, "Conductance of crossed carbon nanotubes," *J. Phys. Soc. Jpn*, vol. 70, no. 6, pp. 1647–1658, 2001.

[75] S. Uryu, "Electronic states and quantum transport in double-wall carbon nanotubes," *Phys. Rev. B*, vol. 69, no. 7, pp. 075402(1–10), 2004.

[76] J. C. Slater and G. F. Koster, "Simplified lcao method for the periodic potential problem," *Phys. Rev.*, vol. 94, no. 6, pp. 1498–1524, 1954.

[77] W. A. Harrison, "Electronic structure and the properties of solids: The physics of the chemical bond," *San Francisco, CA:Freeman*, 1990.

[78] P. Lambin, V. Meunier, and A. Rubio, "Electronic structure of polychiral carbon nanotubes," *Phys. Rev. B*, vol. 62, no. 8, pp. 5129–5135, 2000.

[79] M. Z. Kauser and P. P. Ruden, "Effects of chirality and diameter on the transport properties of semiconducting carbon nanotubes," *J. Appl. Phys.*, vol. 102, no. 3, pp. 033712(1–10), 2007.

[80] M. Z. Kauser and P. P. Ruden, "Electron transport in semiconducting chiral carbon nanotubes," *Appl. Phys. Lett.*, vol. 89, no. 16, pp. 162104(1–3), 2006.

[81] K. Alam and R. Lake, "Performance metrics of a 5 nm, planar, top gate, carbon nanotube on insulator (COI) transistor," *IEEE Trans. Nanotechnol.*, vol. 6, no. 2, pp. 186–190, 2007.

[82] K. Alam, "Transport and performance of a zero-schottky barrier and doped contacts graphene nanoribbon transistors," *Semicond. Sci. Technol.*, vol. 24, no. 1, pp. 015007(1–8), 2009.

[83] D. A. Muller, T. Sorsch, S. Moccio, F. H. Baumann, K. Evans-Lutterodt, and G. Timp, "The electronic structure at the atomic scale of ultrathin gate oxides," *Nature*, vol. 399, pp. 758–761, 1999.

[84] A. Javey, J. Guo, M. Paulsson, Q. Wang, D. Mann, M. Lundstrom, and H. Dai, "High-field quasiballistic transport in short carbon nanotubes," *Phys. Rev. Lett.*, vol. 92, no. 10, pp. 106804(1–4), 2004.